DE-FE0008868

Novel Functionally Graded Thermal Barrier Coatings in Coal-Fired Power Plant Turbines

Final Technical Report

Period Covered: September 2012 – August 2016

Federal Project Manager: Richard Dunst

Technology Manager: Robert Romanosky

November 2016

Principal Investigator:

Jing Zhang

Email: jz29@iupui.edu; Tel: 317-278-7186

Indiana University – Purdue University Indianapolis

Indianapolis, Indiana

DISCLAIMER

TABLE OF CONTENTS

DISCLAIMER II

ABSTRACT v

Task 1: Design and fabrication of novel thermal coatings 1

Task 1.1: Preparation of the coating powders 1

Task 1.2: Characterization of the powders 1

Task 1.3: APS fabrication of thermal spray coatings 7

Task 2: Characterization and microstructure analysis of the TBCs 10

Task 2.1: Microstructure analysis of the TBCs 10

Task 2.2: Compositional analysis 15

Task 2.3: Porosity measurement 16

Task 3: Evaluation and characterization of mechanical and thermal properties of TBCs 17

Task 3.1: Hardness and Young's modulus 17

Task 3.2: Bond strength between the LZ top coat and bond coat 21

Task 3.3: Erosion resistance 24

Task 3.4: Thermal conductivity of LZ coatings 30

Task 3.5: Coefficient of thermal expansion of LZ coatings 32

Task 4: Modeling of residual stresses, mechanical and thermal properties in TBCs 34

Task 4.1: Analytical modeling of residual stresses in TBCs 34

Task 4.2: DFT and MD modeling of mechanical properties of LZ 37

4.2.1 Introduction 37

4.2.2 DFT LZ models 38

4.2.3 DFT LZ crystal lattice parameter optimization 41

4.2.4 DFT calculations of tensile and shear stress-strain curves and anisotropic elastic moduli 43

4.2.5 DFT Bader charge analysis and charge density distribution 49

4.2.6 MD LZ models 51

4.2.7 MD simulations of LZ tensile and shear deformations 52

4.2.8 Summary of DFT and MD modeling of mechanical properties 55

Task 4.3: DFT, MD, and FE modeling of thermal properties of LZ 56

4.3.1 Introduction 56

4.3.2 Thermodynamics and specific heat of LZ 57

4.3.3 Thermal conductivity of LZ crystal and coating 60

4.3.4 Summary of DFT, MD, and FE modeling of LZ thermal conductivities 67

Task 4.4 Modeling of mechanical properties of ZrO2/Ni interface 68

4.4.1 Introduction 68

4.4.2 DFT model description of ZrO_2/Ni interface 70

4.4.3 Results and discussion of DFT interface models 73

4.4.4 MD model of ZrO_2/Ni interface in tensile and shear deformations 86

4.4.5 Summary of modeling of mechanical properties of ZrO2/Ni interface 91

Task 5: Durability of LZ based TBCs at elevated temperatures 93

Task 5.1: Heat treatment test 93

Task 5.2: Furnace cycling test (FCT) 96

Task 5.3: Jet engine thermal shock (JETS) test 96

Task 5.4: Thermal gradient mechanical fatigue (TGMF) test 102

Task 5.5: Durability of composite LZ/8YSZ coatings 106

REFERENCES 113

APPENDIX: PUBLICATIONS AND PRESENTATIONS AS A RESULT OF THIS RESEARCH 120

ABSTRACT

Principal investigator: Jing Zhang, Indiana University – Purdue University Indianapolis

Contributing authors: James Knapp, Praxair Surface Technologies; Li Li, Praxair Surface Technologies; Yeon-Gil Jung, Changwon National University, South Korea; and Xingye Guo, Indiana University – Purdue University Indianapolis

This project presents a detailed investigation of a novel functionally graded coating material, pyrochlore oxide, for thermal barrier coating (TBC) in gas turbines used in coal-fired power plants. Thermal barrier coatings are refractory materials deposited on gas turbine components, which provide thermal protection for metallic components at operating conditions. The ultimate goal of this research is to develop a manufacturing process to produce the novel low thermal conductivity and high thermal stability pyrochlore oxide based coatings with improved high-temperature durability. The current standard TBC, yttria stabilized zirconia (YSZ), has service temperatures limited to <1200 ^{o}C, due to sintering and phase transition at higher temperatures. In contrast, pyrochlore oxide, e.g., lanthanum zirconate ($La_2Zr_2O_7$, LZ), has demonstrated lower thermal conductivity and better thermal stability, which are crucial to high temperature applications, such as gas turbines used in coal-fired power plants.

Indiana University – Purdue University Indianapolis (IUPUI) has collaborated with Praxair Surface Technologies (PST), and Changwon National University in South Korea to perform the proposed research. The research findings are critical to the extension of current TBCs to a broader range of high-temperature materials and applications. Several tasks were originally proposed and accomplished, with additional new opportunities identified during the course of the project. In this report, a description of the project tasks, the main findings and conclusions are given. A list of publications and presentations resulted from this research is listed in the Appendix at the end of the report.

Task 1: Design and fabrication of novel thermal coating

Research activities

The primary goal of this task is to design novel robust LZ based TBC systems suitable for applications >1200 ^{o}C. Due to LZ's low coefficient of thermal expansion and fracture toughness, which cause poor thermal cycling performance, two TBC architectures are proposed: (1) multiple layered coating, and (2) LZ/8YSZ composite coating. In this task, LZ powders were fabricated using the solid-state reaction method, and all of the coatings were deposited using air plasma spray (APS) technique.

Main findings and conclusions

Single ceramic layer (SCL), double ceramic layer (DCL) and composite LZ based TBC samples were successfully deposited using the APS technique at Praxair Surface Technologies. The APS processing parameters were carefully optimized to achieve desirable coating microstructures.

Task 2: Characterization and microstructure analysis of the TBCs systems

Research activities

The microstructures of the TBCs were studied using SEM, TEM, and optical microscopy. Phase analysis was carried out using x-ray diffraction in the lab, and *in situ* high-temperature synchrotron x-ray at Argonne National Laboratory (ANL).

Main findings and conclusions

For the LZ powder, SEM images show that powder is in spherical shape with an average powder size ~ 65 μm, which meets the powder requirements of the APS process. TEM image shows the crystallinity of the powder. Both x-ray diffraction and synchrotron x-ray confirm the purity and high-temperature stability of the LZ powder from room temperature up to the testing temperature of 1400 ^{o}C, which is critical to TBC applications.

Task 3: Evaluation and characterization of thermal and mechanical properties of TBCs

Research activities

The physical, thermal, and mechanical properties of the sprayed LZ coatings have been systematically investigated, including temperature-dependent thermal conductivity, coefficient of thermal expansion, density, hardness, Young's modulus, bond strength, and erosion resistance.

Main findings and conclusions

The measured average thermal conductivity of the LZ is about 0.59-0.68 W/m/ ^{o}C in the temperature range of 24 - 899 ^{o}C, which is about 25% lower than that of the porous 8YSZ (0.84-0.87 W/m/ ^{o}C) in the same temperature range. The coefficient of thermal expansion (CTE) values of the LZ are approximately 9-10×10^{-6}/ ^{o}C in the temperature range of 127 - 327 ^{o}C, which are similar to the reported literature data.

The hardness values of LZ coatings are similar to porous 8YSZ. The hardness values of dense 8YSZ coats are much higher than other coats, due to their low porosity. The porosity and corresponding hardness of the coatings can be tuned by controlling APS processing parameters.

Task 4: Modeling of residual stresses in TBCs

Research activities

In parallel to experimental investigations, a multi-scale modeling approach has been employed to study the fundamental thermal and mechanical properties of LZ crystal and coatings. Physics-based models were developed, including using the density functional theory (DFT), molecular dynamics (MD), and finite element (FE) methods. The nanoscale tensile and shear deformations of LZ single crystal were simulated using the DFT calculations with the generalized gradient approximation (GGA) functional. The anisotropic Young's moduli were studied using two approaches: (1) stress-strain curve of large deformation, and (2) analytical method in small deformation. Additionally, the tensile and shear large deformations of LZ single crystal were simulated using the MD method with Buckingham and Coulomb potentials at room temperature.

Main findings and conclusions

Both DFT and MD results show that LZ has strong anisotropic Young's moduli with the ranking of crystallographic orientations [111] > [110] > [100]. The shear modulus in {111}<110> direction is slightly higher than that in {111}<11$\bar{2}$> direction. Both Bader charge transfer and electron charge density analyses indicate that the electron interactions between O and Zr ions in LZ are stronger in [111] direction for tensile, and in {111}<110> direction for shear deformation.

For thermal properties, the temperature-dependent thermal conductivities of LZ coating were calculated using a multiscale approach. First, the thermal conductivity of LZ single crystal was calculated using a reverse non-equilibrium molecular dynamics (reverse NEMD) approach. The single crystal data was then passed to a FE model which takes into account realistic TBC microstructures. The predicted thermal conductivities from the FE model are in good agreement with experimental validations using both flash laser technique and pulsed thermal imaging-multilayer analysis conducted at Argonne National Laboratory.

Furthermore, the mechanical properties at the ceramic-metal (C-M) interface in TBCs were investigated. The nanoscale tensile and shear deformations of the ZrO_2/Ni interface, an approximation of the interface between the top and bond coats, were performed using both DFT and MD calculations. The DFT results show that the elastic modulus, ultimate strength, and toughness of the C-M interface increase with the decrease of the Ni layer thickness. The MD simulations using the COMB3 potential show that the Young's modulus of ZrO_2/Ni interface in [111] direction is larger than that in [100] direction, and the shear modulus in {111}<110> direction is higher than that in {111}<$11\bar{2}$> direction.

Task 5: Durability of LZ based TBCs at elevated temperatures

Research activities

The durability of the coatings in various thermal and mechanical conditions was investigated, including heat treatment, furnace cycling test (FCT), thermal gradient mechanical fatigue test (TGMF), and jet engine thermal shock (JETS) test.

Main findings and conclusions

For the layered TBCs, both furnace heat treatment and JETS tests show that the double-layer LZ+ porous YSZ coating has better thermal shock and thermal cycling performances than those of the single-layer LZ coating and the double-layer LZ+ dense

YSZ coating. The results suggest that the porous 8YSZ can be used as a buffer layer for LZ based TBC systems to improve the durability during service. However, all layered LZ coatings were delaminated in the FCT test. The delamination of LZ coatings in FCT and JETS test is related to the thermal residual stress induced by the CTE difference and the low fracture toughness of the LZ coatings.

Since the layered LZ based TBCs have limited thermal durability performance, LZ/YSZ composite coatings are proposed. The results show that LZ/8YSZ (vol.% is 50:50) with a thin buffer layer LZ/8YSZ(vol.% is 25:75) has the greatest thermal cycling performance in both FCT and JETS tests. This is because the composite LZ/YSZ coatings reduce the CTE difference at the interface. In addition, the fracture toughness of the composite coatings is increased by adding 8YSZ into LZ coatings.

Task 1: Design and fabrication of novel thermal coatings

Task 1.1: Preparation of the coating powders

The criteria of fabrication LZ feedstock powders include: (1) spherical shape powder, (2) uniform and fine particle size distribution, (3) homogeneous composition, (4) high purity, and (5) low fabrication cost. The requirement of the shape and size distribution in powder is because the powder flow capability is important for a feeding stock in thermal spray process. The spherical shaped powder and its uniform particle size are critical to smooth flow of powder through the feedstock-feeding pipe of the thermal spray equipment. Homogeneous composition and higher purity can enhance the phase stability and corrosion resistance, which improve the coating lifetime.

In general, three preparation methods have been used in laboratory: (1) solid state reaction [1, 2], (2) nitric acid dissolution method [3], and (3) sol-gel technique [4-6]. Comparing these methods, solid state reaction method is ideal for large scale fabrication in industry.

This project requires to fabricate the TBC materials that is scalable. All of LZ powders used in this project were fabricated using the solid state method. The raw materials for the LZ fabrication include La_2O_3 and ZrO_2. The raw materials were milled into small particles in the first step. Then La_2O_3 and ZrO_2 powders were mixed together using a V-shaped powder blender. After that, water and binder material were pumped into the mixed raw materials, and all the materials were made into a “slurry cake”. After that, the “slurry cake” was dried in 150 ^{o}C for several hours. Finally, the mix raw materials were filled into an alumina case and calcined in a furnace at 1650 ^{o}C. The LZ material was synthesized during the high-temperature calcination process. To satisfy the size requirement of the thermal spray process, the powder needs to be screened with specific mesh sizes for several times.

Task 1.2: Characterization of the powders

The LZ powder size was measured by Microtrac standard range particle analyzer (Microtrac, s3500, Pennsylvania, USA). The particle analyzer statistically analyzes the particle size using three precisely placed red laser diodes to accurately characterize particles. The column in Fig. 1 shows the size distribution of the LZ powder. The size distribution shows that the average powder size is ~65 µm, which meets the powder size requirement of the APS process.

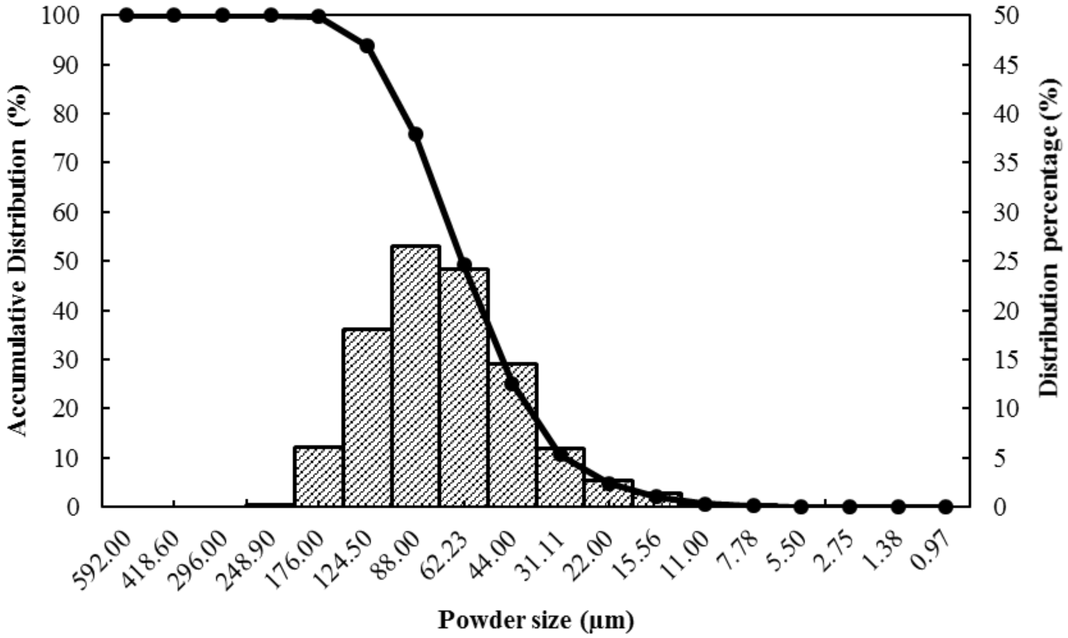

Figure 1: LZ powder size distribution.

The chemical composition of the LZ powders was analyzed using inductively coupled plasma techniques (ICP) and inductively coupled plasma mass spectrometry (ICP-MS) methods at the NSL analytical test laboratory. Table 1 shows the chemical composition of LZ. The measured chemical compositions of LZ powders are very close to the theoretical weight ratio of ZrO_2 and La_2O_3 in LZ (43%: 57%), suggesting that the solid state reaction approach produces the LZ powder with required compositions.

Table 1: Chemical composition of LZ powder

Chemistry	Test method	Weight percentage
Lanthanum Oxide	ICP	57.0
Zirconium Oxide	ICP	41.6
Aluminum Oxide	ICP	<0.1
Ferric Oxide	ICP-MS	0.1
Hafnium Oxide	ICP	0.1
Silicon Dioxide	ICP	0.7
Other Oxides Total	ICP-MS	~0.4

X-ray diffraction (XRD) test of the LZ powder was performed using a laboratory XRD equipment with a wavelength of 1.54 Å. The XRD scan speed is 4 degrees per minutes and the scan increment is 0.02 degree per step. As shown in Fig. 2, the XRD pattern of the LZ powder synthesized by the solid state reaction (red curve) matches very well with the standard XRD pattern card of LZ (pdf card #73-0444, green lines). In addition, the XRD pattern shows that LZ is a cubic phase with the space group $Fd\overline{3}m$ (227). The powder shows narrow peak widths, suggesting high crystalline in the LZ powder.

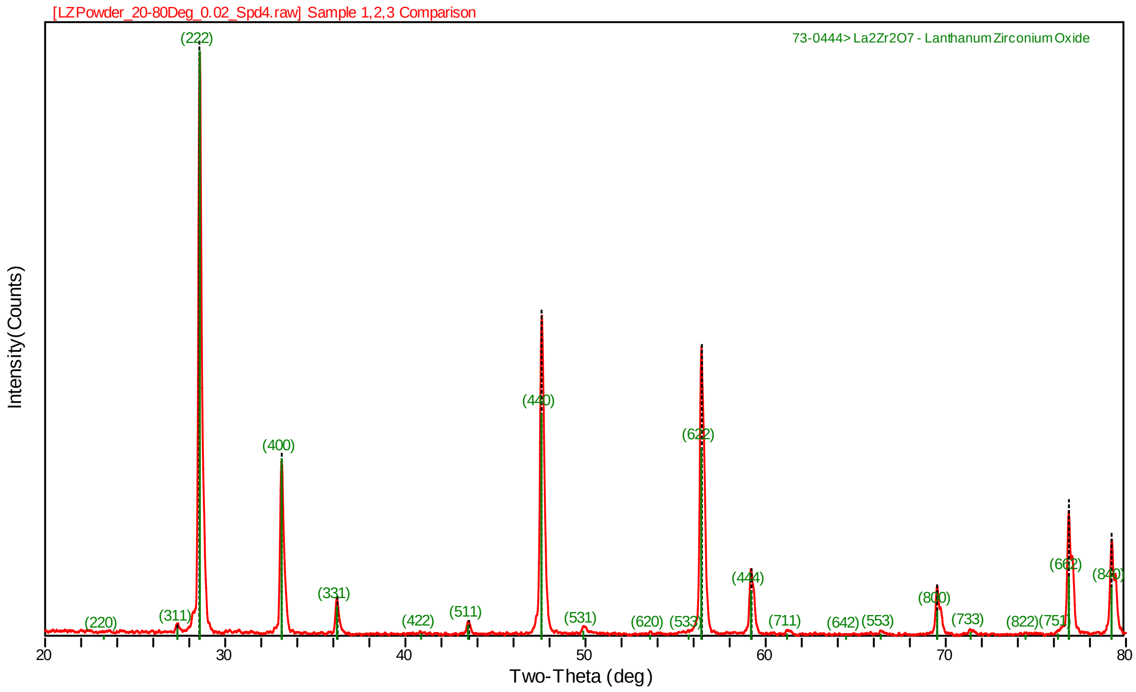

Figure 2: X-ray diffraction data of LZ powder.

In addition, phase stability of the LZ from room temperature to 1673K (1400 ^{o}C) has been studied using *in situ* synchrotron X-ray diffraction (XRD) at Argonne National Laboratory, as shown in Fig. 3 [7, 8]. The synchrotron XRD curves of LZ powder do not show any peak pattern changes from 30 ^{o}C to 1400^{o}C, indicating that there is no phase change during this continuous heating and cooling process.

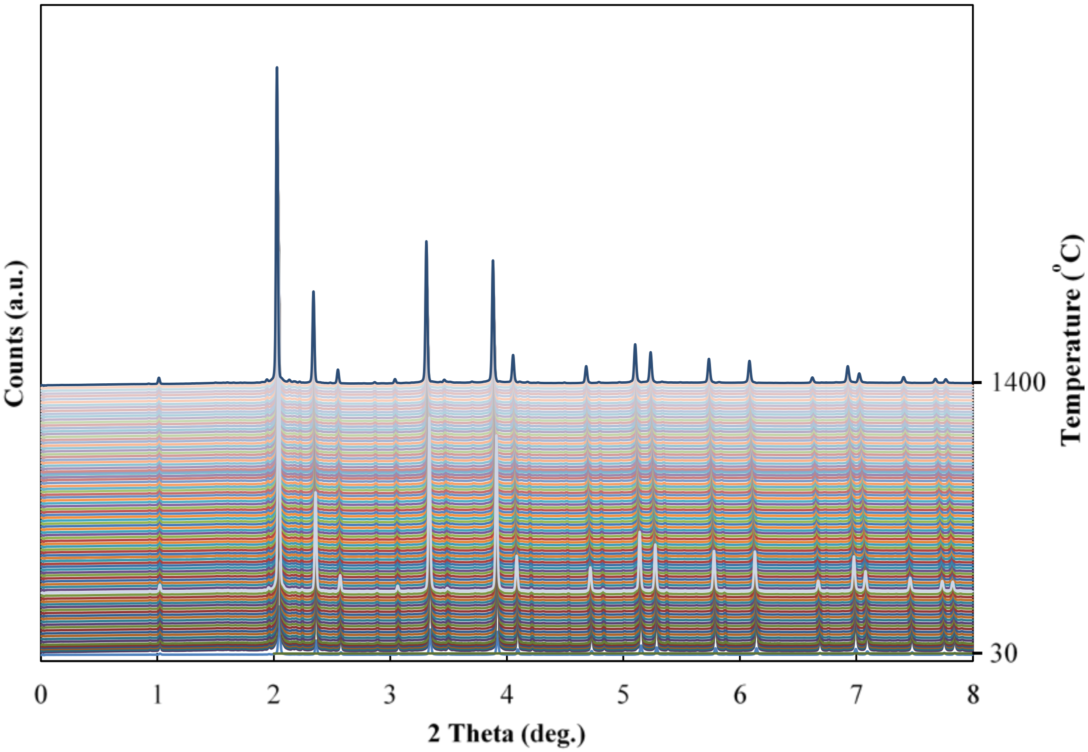

Figure 3: *in situ* synchrotron XRD of the LZ powder as a function of temperature.

The scanning electron microscope (SEM) images of LZ powders, which can be directly used as the feedstock powders in the thermal spray process, are shown in Fig. 4. The powder shows spherical or ellipse shape with a uniform particle size of ~ 65 μm. In a single LZ particle, porous surface is evident.

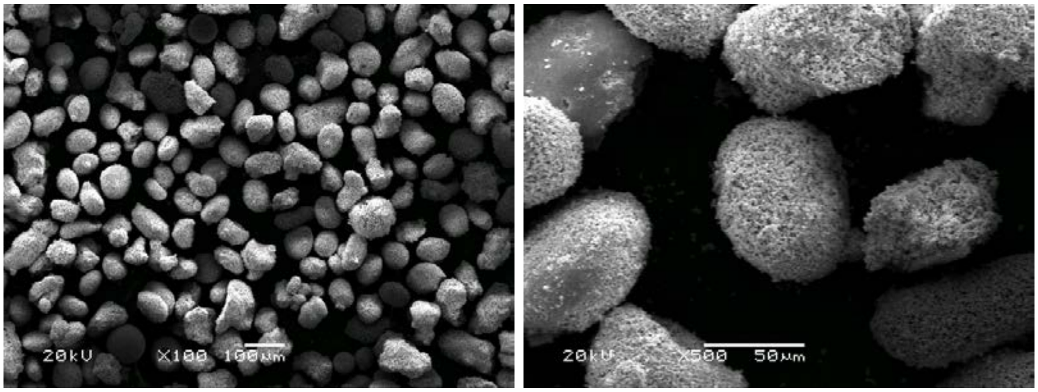

(a) (b)

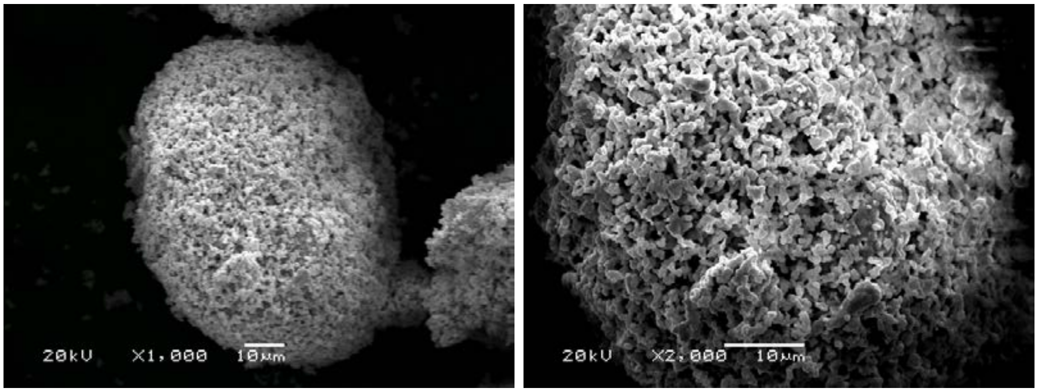

(c) (d)

Figure 4: SEM images of LZ powders under different magnifications (a) X100, (b) X500, (c) X1000, (d) X2000.

To further understand the LZ crystalline morphology, transmission electron microscopy (TEM) image of milled LZ coating powders is shown in Fig. 5, which exhibits polycrystalline characteristics.

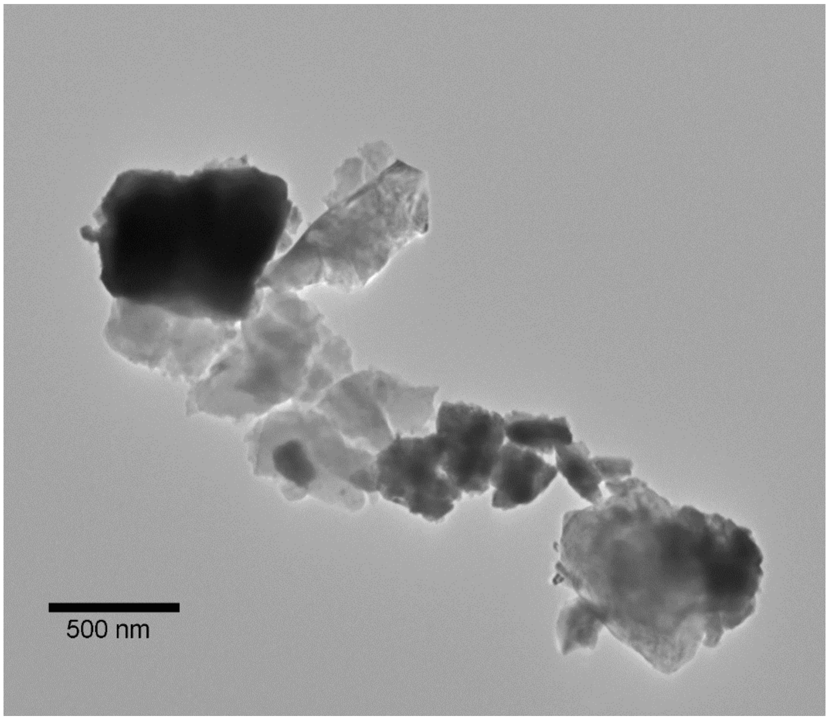

Figure 5: TEM image of the LZ powder

Task 1.3: APS fabrication of thermal spray coatings

The primary goal of this task is to design novel robust LZ based TBC systems suitable for applications beyond 1200 ^{o}C. Due to LZ's low coefficient of thermal expansion and fracture toughness, which cause poor thermal cycling performance, two TBC architectures are proposed: (1) multiple layered coating, and (2) LZ/8YSZ composite coating.

All LZ coatings were deposited using APS technique using a Praxair patented plasma spray torch. Haynes 188 superalloy (Haynes International, Kokomo, IN, USA) was used as the standard substrate material. NiCrAlY powder, Ni-211 (Praxair Surface Technologies, Indianapolis, IN, with chemistry of Ni 61.5 wt%, Cr 21.12 wt%, Al 9.94wt%, Y 1.02wt% [9]) was selected as a standard bond coat feedstock in this work. The bond coat thickness was in the range of 180-230 μm. LZ or 8YSZ top coats were deposited above the bond coat using the APS technique. The thicknesses of the top coats used in this project range from 300 to 600 μm. In order to deposit the top coats with designated porosity, all of the APS parameters were properly tailored. Dense and porous 8YSZ TBCs system were also deposited as a reference sample on the same bond coat and substrate using the same deposition technique and similar deposition parameters. AMPERIT 825.001 and AMPERIT 827.006 (HC Starck, Munich, Germany) were selected powders to produce the dense and porous 8YSZ.

Four types of shapes were applied as substrate. 10 mm cubic bulk substrates were used to produce the free-standing samples, which were deposited directly on smooth substrates without any bond coats. The top coats can be easily peeled off from the cubic substrates. Round button HS 188 substrates with a diameter of 1 inch (25.4 mm) were used in the bond strength tensile tests. Tensile bar samples (200×20 mm) were used in thermal gradient mechanical fatigue (TGMF) tests. Rectangular panel (50.8×25.4 mm) samples were used in erosion tests.

The layered LZ coatings are presented first. Single ceramic layer (SCL) LZ coating samples deposited in the first batch are aimed to investigate the physical, mechanical and thermal properties of pure LZ coating. The SCL samples were coated using the same powder feed ratio, deposition speed, and plasma current for single layer coating. The only difference between sample 1 to sample 5 is the standoff distances, which is the distance from the spray torch to the sample surface. The deposition standoff and physical parameters of SCL LZ coatings in the first batch are listed in Table 2.

Table 2: Physical properties of LZ SCL coating deposited in first batch

Sample No.	Standoff distance (mm)	Density (g/cm^3)	Top coat thickness (µm)	Porosity (%)
1	165.1	5.2587	445	11.36
2	177.8	5.2584	422	12.36
3	190.5	5.2917	389	11.81
4	203.2	5.2614	373	12.31
5	215.9	5.0089	365	16.52

Double layer TBCs deposited in the second batch include both 8YSZ and LZ layers. Both coating layers were sprayed using APS method in the second batch. Two different types of double-layer TBC samples were deposited: LZ coating on a porous 8YSZ layer and LZ coating on a dense 8YSZ layer. Additionally, two types of single-layer TBC samples, single-layer LZ and single-layer porous 8YSZ, were produced for comparison purposes. All prepared TBC samples are listed in Table 3.

Table 3: Architecture and porosity of SCL and DCL layered LZ coatings in second batch

Sample No.	Bond coat	Top coats	Thickness (µm)	Porosity (%)
6	NiCrAlY	SCL LZ	424	11.54
7	NiCrAlY	DCL Porous 8YSZ + LZ	138 + 305	15.95 / 11.54
8	NiCrAlY	DCL Dense 8YSZ + LZ	140 + 292	7.24 / 11.54
9	NiCrAlY	SCL porous 8YSZ	452	15.95

For LZ/8YSZ composite coatings, the biggest challenge of LZ for application is the relative shorter thermal cycling lifetime than the traditional 8YSZ coating due to LZ’s lower CTE and fracture toughness than 8YSZ. In this research, a new LZ/8YSZ composite coating material was designed, which was aimed to improve the toughness and CTE of the top coatings. Buffer layer also introduced into this architecture to further reduce the residual thermal stress at the interface between top and bond coat. The architecture, composition, and thickness of the LZ/8YSZ composite coating sample are listed in Table 4. Sample 10 and 12 are single layer coatings that do not have any buffer layer. Sample 11 is a double layer TBC that contains an 8YSZ buffer layer and a 50% LZ/50% 8YSZ composite coat. Sample 13 has an 8YSZ buffer layer and two composite top coats, which are a 25% LZ/75% 8YSZ composite coating on the bottom and a 50% LZ/50% 8YSZ composite coat on the top. All of these composite coating samples were deposited using APS technique on the Ni-based superalloy substrates (Nimonic 263, ThyssenKrupp VDM, Germany, composition: Ni-20Cr-20Co-5.9Mo-0.5Al-2.1Ti-0.4Mn-0.3Si-0.06C, in wt.%) with an AMDRY 962 bond coat (Sulzer Metco Holding AG, Switzerland, composition: Ni-22Cr-10Al-1.0Y in wt.%). The same LZ and 8YSZ powders were deposited as the aforementioned sections [43].

Table 4: List of the LZ/8YSZ composite coating samples

Sample No.	Buffer layer composition	Buffer layer thickness (μm)	Top coat composition		Top coat thickness (μm)	
10	No buffer layer	-	50% LZ + 50% 8YSZ		430	
11	Porous 8YSZ	60	50% LZ + 50% 8YSZ		370	
12	No buffer layer	-	25% LZ + 75% 8YSZ		430	
13	Porous 8YSZ	60	25% LZ+75% 8YSZ	50% LZ + 50% 8YSZ	60	310

Task 2: Characterization and microstructure analysis of the TBCs

Task 2.1: Microstructure analysis of the TBCs

Both SCL and DCL TBCs systems and the free-standing samples were used to observe the cross-sectional microstructure. All of the samples were sectioned and mounted by cold-mounting method with epoxy and hardener. A significant benefit gained by using cold-mount materials is that the epoxy can impregnate and fill surface-connected pores, which can provide a strong support to the porous sample [10]. The microstructures of the complete TBCs system samples were observed using an optical microscope, and the free standing samples were examined by a scanning electron microscope (SEM; JEOL, JSM−5610, Japan). The optical images of cross-sectional microstructures of the as-prepared TBC specimens are shown in Fig. 6. The LZ coatings deposited above the bond coat (white layer). LZ with different thicknesses and porosities can be well deposited on the bond coat without delamination or cracking at the interface. Fig. 6 shows that all of the LZ top coats have lots of pores, but without large cracks. The coating thickness is decreased from sample 1 to sample 5, while porosity increases from sample 1 to sample 5. Relatively large defects such as pores and unmelted particles were increased by from sample 1 to sample 5.

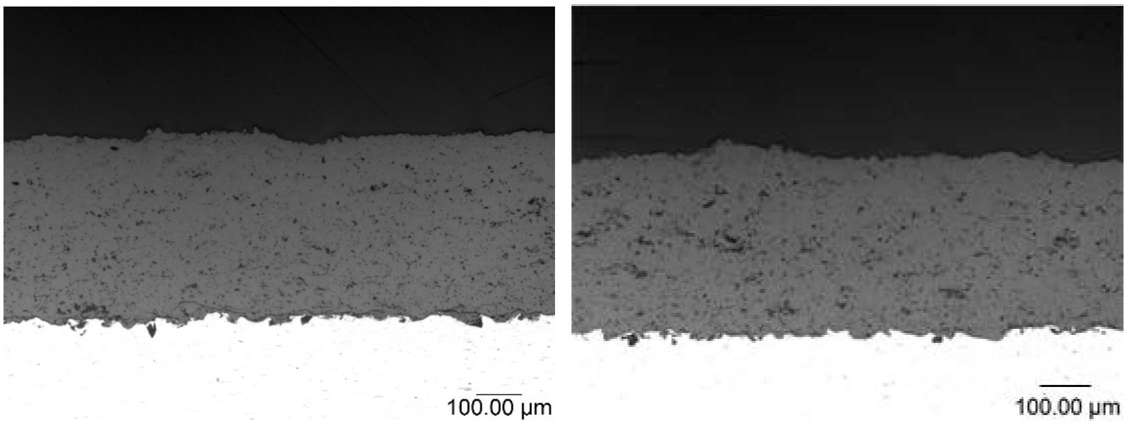

(a) (b)

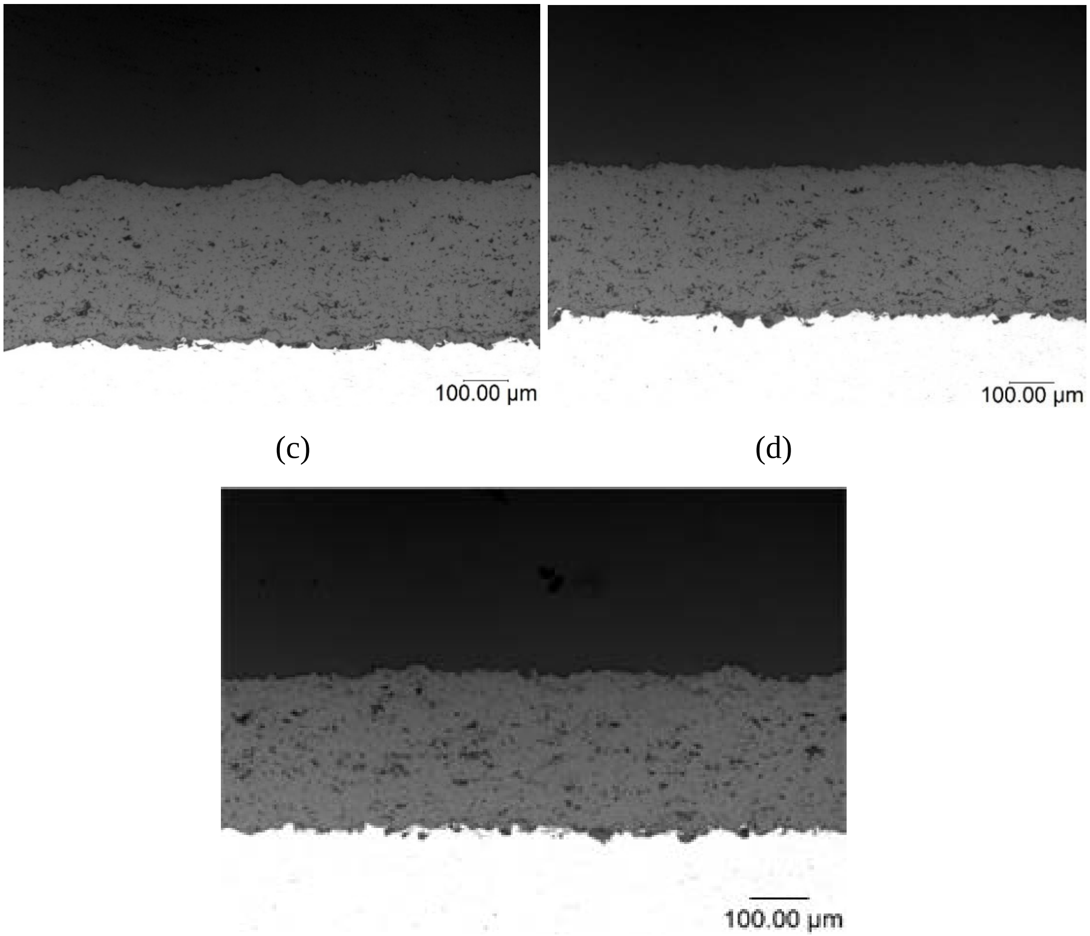

(c) (d)

(e)

Figure 6: Optical microscopic images of SCL LZ samples. (a) Sample 1, (b) Sample 2, (c) sample 3, (d) sample 4, (e) sample 5.

Fig. 7 shows the SEM images of SCL LZ free-standing samples. It illustrates the detailed microstructure for samples of various porosities. The microstructures show a lot of intrinsic defects, such as pores, unmelted particles and splat boundaries in the coat preparation process. In Fig. 7e, sample 5 shows obviously higher porosity than sample 1~ sample 4. Different pores in various morphologies can be spotted, and some of the unmelted feedstock powders can also be found in the SEM images. In general, the microstructures in Fig. 6 and Fig. 7 show that the number and size of the defects are proportional to the porosity measurements as shown in Table 2. As the standoff distance increases, the defects in the microstructure increase. So, coatings with relatively accurate porosity can be achieved through tuning the standoff distance.

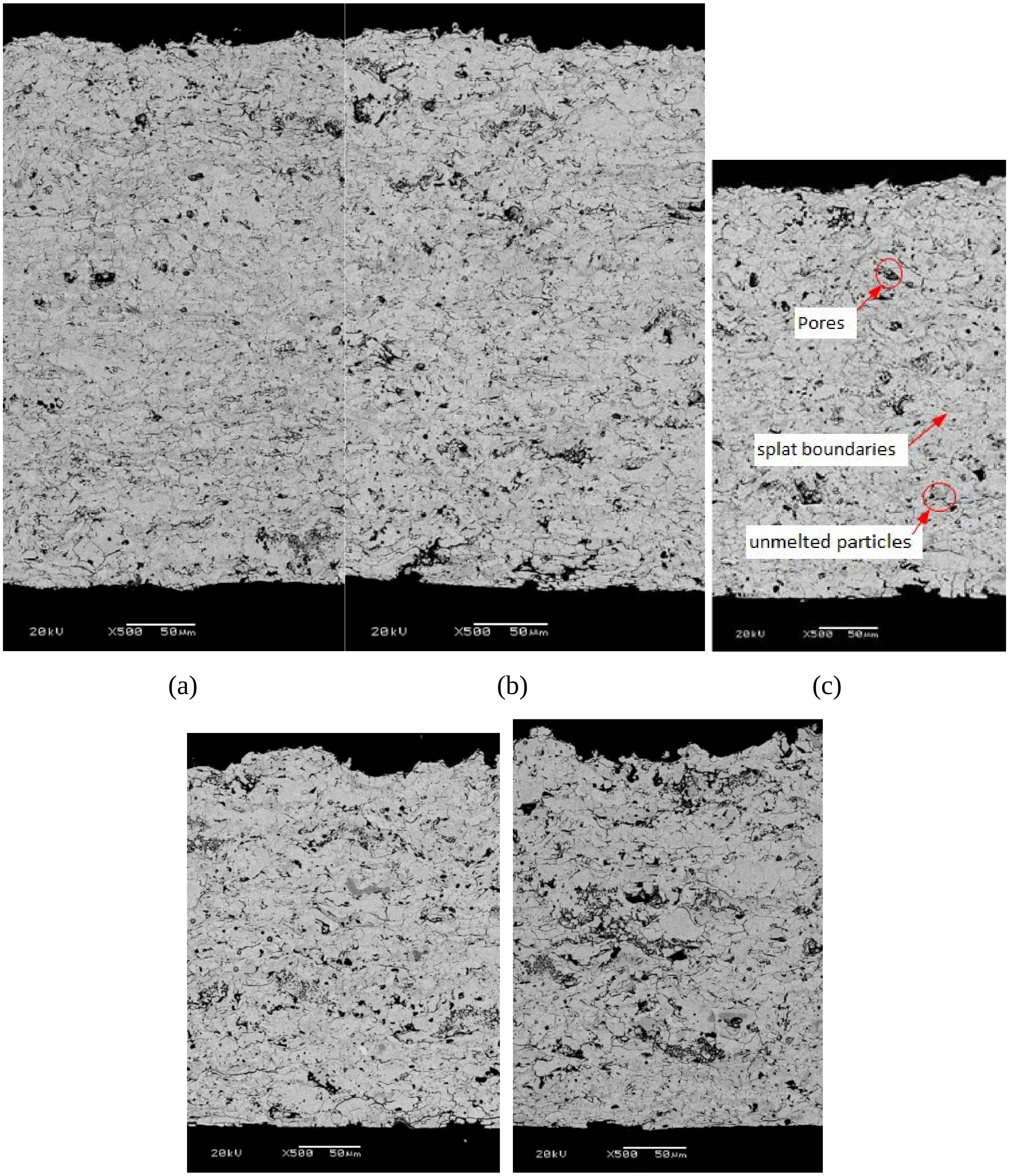

(a) (b) (c)

(d) (e)

Figure 7: SEM images of cross section microstructures of LZ coating. (a) sample 1, (b) sample 2, (c) sample 3, (d) sample 4, (e) sample 5.

The pores constitutes a large portion of total porosity which is illustrated from the microstructures shown in Fig. 7. The distribution and the size of pores are not uniformity in all samples. The porosity has a large influence on thermal and mechanical properties. With a large number of pores and cracks in TBCs, the mechanical properties will also have a severe change.

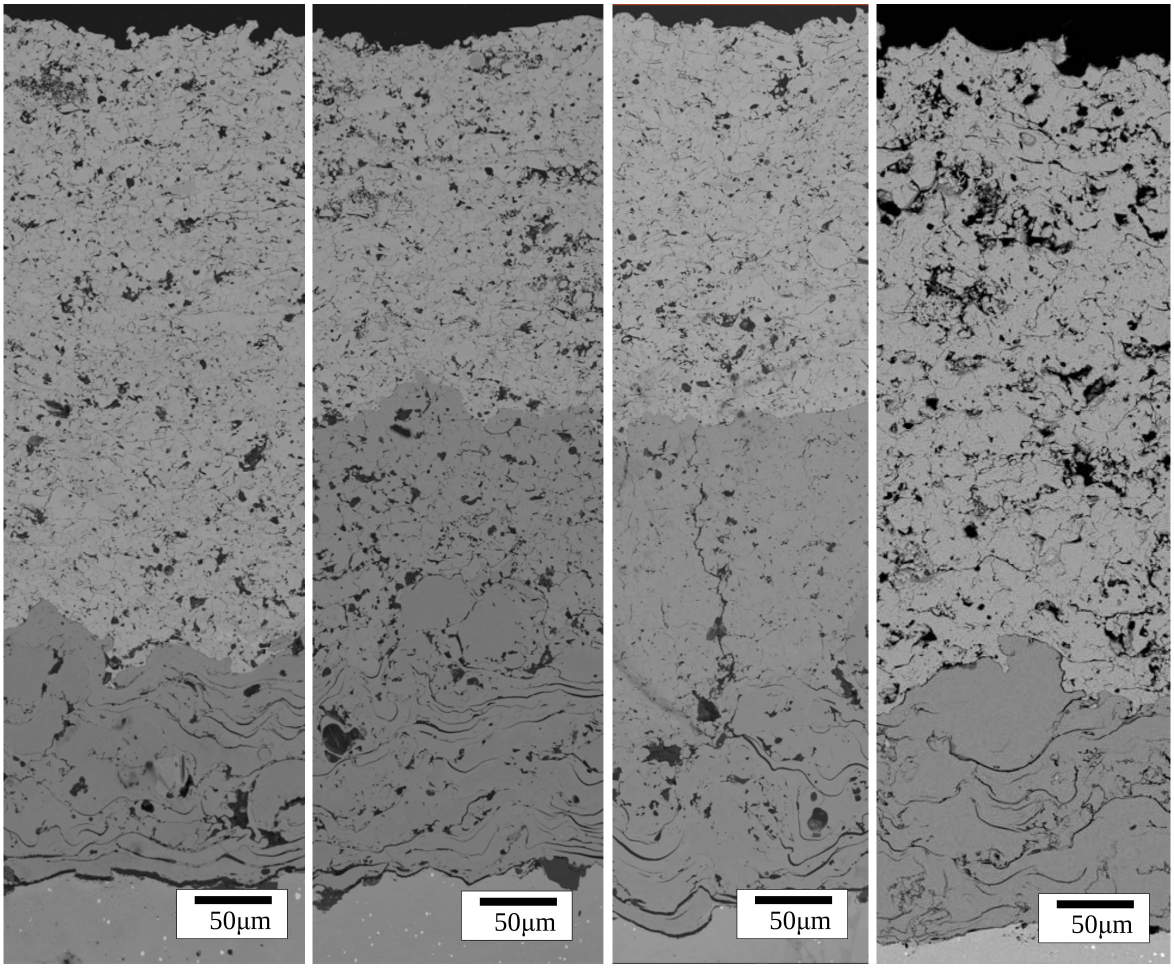

(a) (b) (c) (d)

Figure 8: SEM images showing the cross sectional microstructure of the as-sprayed SCL and DCL samples: (a) sample 6: SCL porous LZ , (b) sample 7: DCL porous 8YSZ+ LZ , (c) sample 8: DCL dense 8YSZ+ LZ, (d) sample 9: SCL porous 8YSZ.

The microstructure images of the as-sprayed DCL and SCL LZ/8YSZ layered coating are shown in Fig. 8. All of the coatings show a sound status without delamination. There is no TGO at the interface between the top coat and bond coat, suggesting the bond coat is not oxidized yet. Scattered pores and cracks are obvious in the porous LZ and 8YSZ layer, and vertical cracks generated in the dense 8YSZ layers, which is good for the coating durability performance [11].

For LZ/8YSZ composite coatings, the cross-sectional microstructure SEM images of as-sprayed composite TBC samples are shown in Fig.9. The bond coat and buffer layers demonstrate a typical microstructure of APS deposited coating. The two component materials LZ (white color) and 8YSZ (gray color) are glued together as a layered “splats” form in the top coat, which leaves some micro-cracks and pores in the coating. There is no delamination or spallation in the as-sprayed top coat and buffer layer, suggesting the initial deposition has a high quality. All the surface and interfaces show an irregular roughness, and No TGO layer can be observed at the interface between top coat (or buffer layer) and bond coat [43].

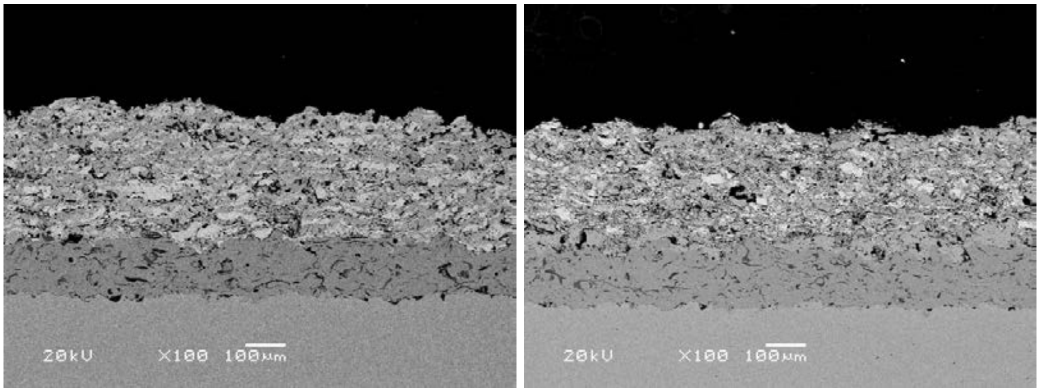

(a) (b)

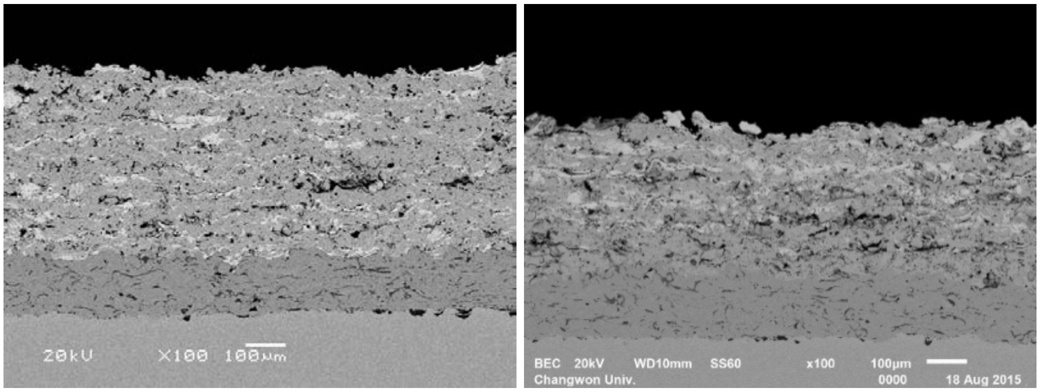

(c) (d)

Figure 9: SEM images of cross sectional view of the LZ/8YSZ composite coatings. (a) sample 10, (b) sample 11, (c) sample 12, (4) sample 13.

Task 2.2: Compositional analysis

Energy-dispersive X-ray spectroscopy (EDS) was used to on sample 8 to examine the compositional distribution between LZ and 8YSZ layer in the bilayer TBC system, as shown in Fig. 10. Before the EDS analysis, sample 8 was heat treated at 1080 °C for about 4 hours. Both Zr and La elements were analyzed using line scan as shown in Fig. 10. There is no obvious diffusion of Zr and La element between the two layers.

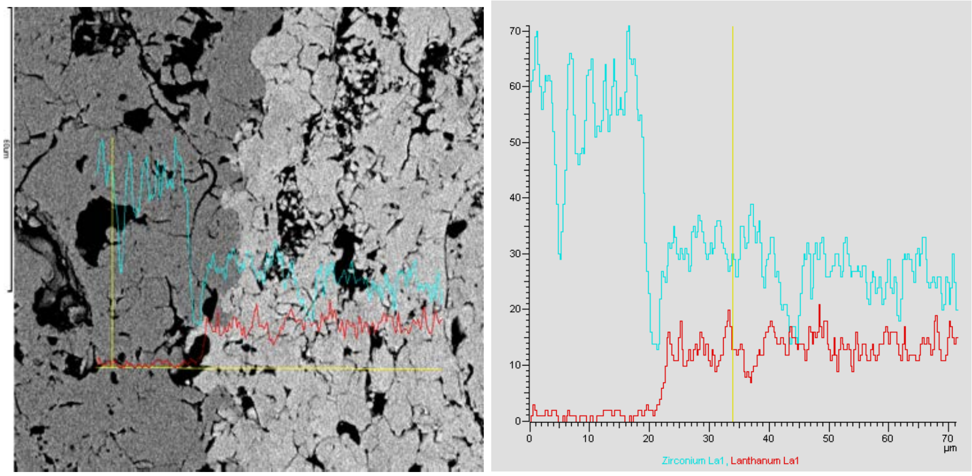

(a) (b)

Figure 10: EDS analysis at the interface between LZ and 8YSZ layers on sample 8

Task 2.3: Porosity measurement

The density measurement for LZ top coat was conducted using the free standing coatings with a thickness of 432 µm. The samples were peeled off from the 10 mm cubic substrate. The density was measured following the ASTM standard B328-94, which is based on the Archimedes' principle. The measurement apparatus includes an analytical balance (Mettler AE240, Switzerland) and a density determination kit (Denver Instrument, density kit, Arvada, Colorado).

The porosities and densities of the as-sprayed SCL samples deposited in the first batch are summarized in Table 2. The porosities range from 11.81 % ~ 16.52 %. The porosity values obtained here are calculated using the theoretical density of LZ, 6.05 g/cm^3 [12]. Typically, the commercial APS 8YSZ coatings have a porosity of 10-20% [13]. Since the mechanical properties of LZ decrease with increasing porosity, it is important to control the porosity in the range of 10% to 15% through tuning the APS process parameters. From Table 2, it shows that when the standoff distance is increased, the porosity increases as well.

The porosities of second batch SCL and DCL LZ/8YSZ layered coatings are listed in Table 3. The free-standing LZ top coat of sample 6 was used to measure the porosity and density of all the LZ coat layers, because the density of LZ coat layer among sample 6, 7 and 8 are almost same. The measured average densities and porosities of LZ layer in samples 6, 7 and 8 are 5.35g/cm^3 and 11.54 %, respectively. Porosities in the dense and porous 8YSZ layers are 7.24 % and 15.95 %, respectively.

Task 3: Evaluation and characterization of mechanical and thermal properties of TBCs

Task 3.1: Hardness and Young's modulus

The whole TBCs system samples (include top coat, bond coat, and substrate) were used to evaluate the mechanical properties. Vickers indentation experiments were applied on the cross-sectional mounted samples of the TBC system so that the hardness of each layer can be measured individually. The hardness values of the top coats were determined using a Vickers hardness tester (Mitutoyo Corp., HM−114, Japan) with a Vickers tip for a load of 10 N and a nanoindenter (MTS, nanoindenter XP, Minnesota).

The Vickers hardness results of SCL LZ samples that sprayed in the first batch are summarized in Fig. 11. The hardness values in porous TBCs are not as easily and clearly defined as those in dense material since the "splat" boundaries and pores would influence the indentation measurement results. Therefore, the results in Fig. 11 show some variations. The hardness of sample 5 is the lowest, which is in consistent with its low density and high porosity. Fig. 11 shows that the harnesses decrease as the porosities increase.

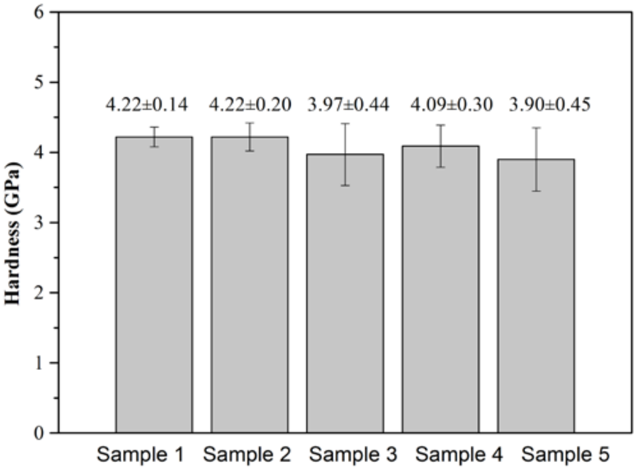

Figure 11: Vickers hardness of SCL LZ coatings sprayed in first batch.

Fig. 12 shows the hardness results of the SCL and DCL LZ/8YSZ layered coatings, which were sprayed in the second batch. The hardness values of porous 8YSZ coats are similar to the LZ coats, as shown in Fig. 11. The small difference might be due to the difference of the porosity between these two coating layers. The hardness values of dense 8YSZ coats are much higher than other coats, due to its low porosity. As a result, the hardness of the TBC coating is related to the porosity and composition.

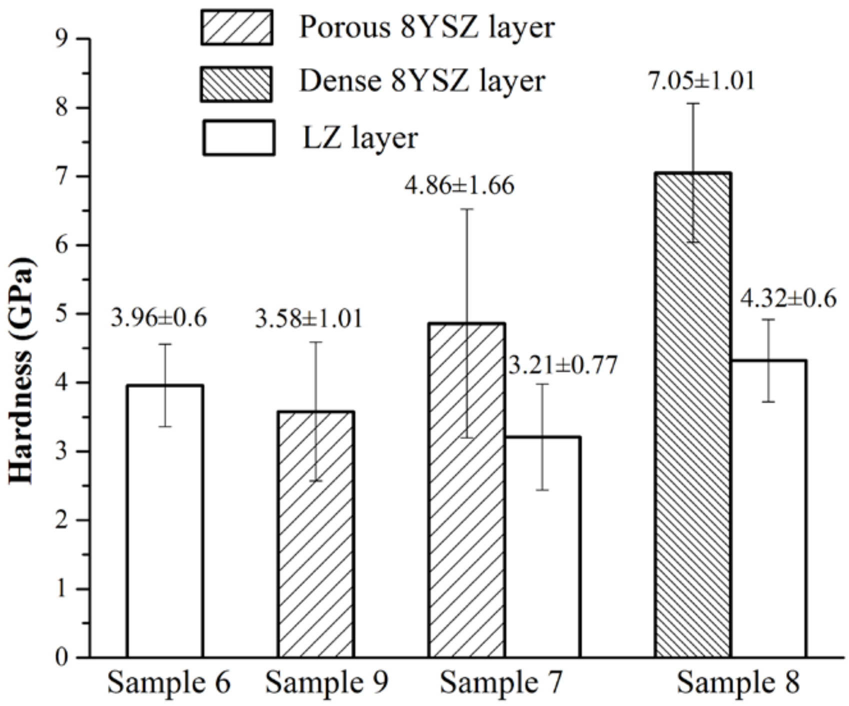

Figure 12: Vickers hardness in different layers of the DCL TBC samples.

Nanoindenter measures the hardness and Young’s modulus by continuously monitoring the displacement of the indenter by a capacitance gauge as the load is applied. The nanoindentation hardness was performed using the calibrated shape of the diamond tip [14]. Nanoindentation employs the Berkovitch diamond indenter. There are two testing modes that can be applied in the nanoindentation tests: the depth control mode, and the load control mode. In this study, the load control mode was employed. In order to reach the predesignated 500 mN, five consecutive indentations movement were conducted at the same position. The hardness values can be obtained from each indentation. However, when the indenter displacement is small, there are quite a lot of errors due to artificial effects in the experiments, such as surface roughness and contact angle. The accuracy can be improved with increasing displacement.

The nanoindentation hardness results of LZ coating sprayed in the first batch are summarized in Fig. 13. The nanoindentation hardness normally has a higher value than the Vickers hardness, because localized indentations are used, where pores can be avoided in nanoindentations. However, the variations of nanoindentation hardness are larger than Vickers hardness because of the complex microstructure on various indentation sites. These results indicate that nanoindentation hardness decreases as the porosities increases, due to the existence of the pores, splat boundaries, and cracks.

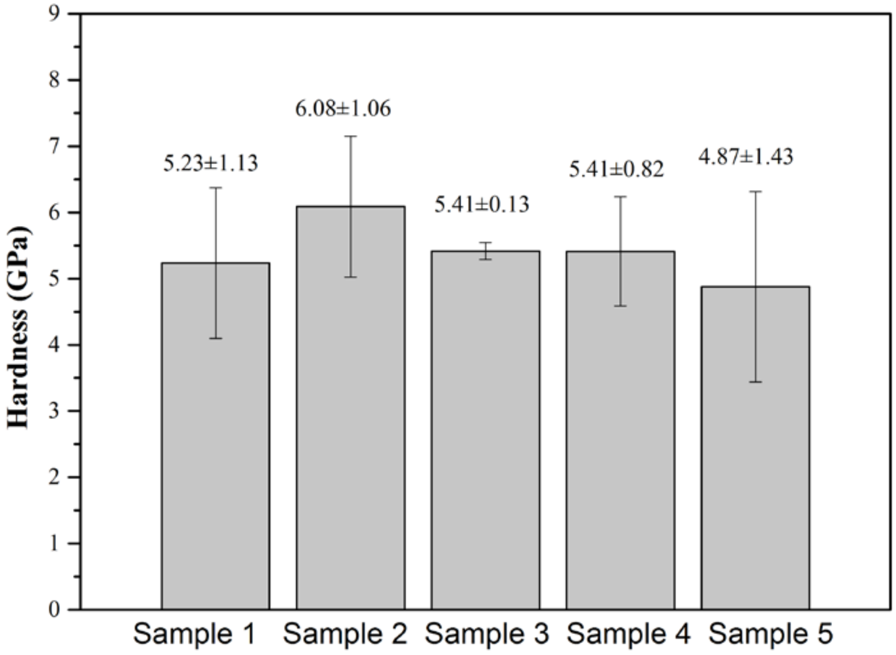

Figure 13: Nanoindentation hardness

The Young’s modulus results are calculated from the slope of the unloading part in the load and displacement curve in nanoindentation measurements, as shown in Fig. 14. During unloading, it is assumed that only the elastic displacements are recovered. Because of the elastic nature of the unloading curve, the elastic modulus can be analyzed. Fig.14 shows the calculated Young’s modulus values. Sample 5 has a smaller Young’s modulus than that of samples 2, 3 and 4. Comparing microstructures with the porosity data, the Young’s modulus in LZ coatings decreases as the porosity increases.

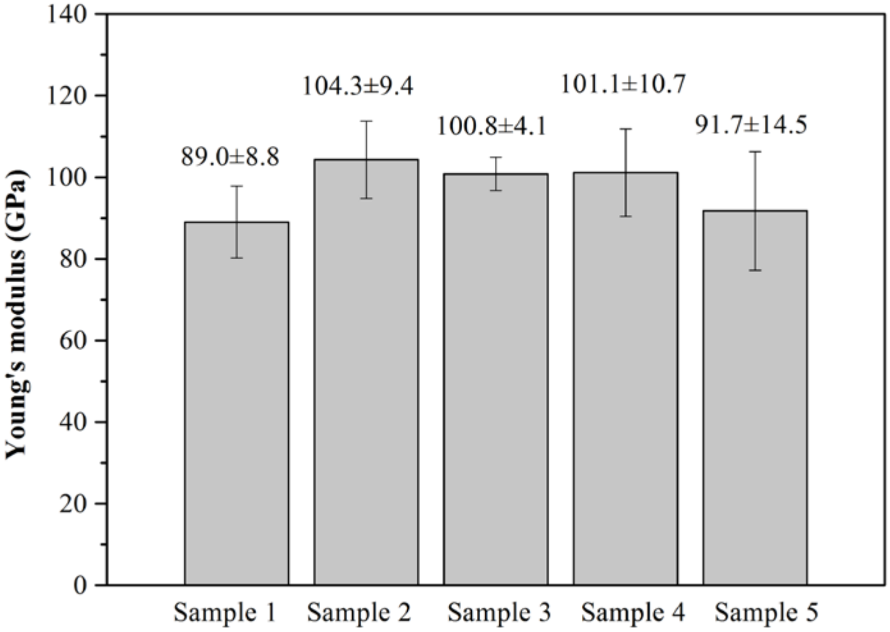

Figure 14: Young’s modulus of SCL LZ TBC measured by nanoindentation.

The correlation between the Young’s modulus and nanoindentation hardness is investigated. In order to calculate the Young’s modulus, three important quantities must be measured in the load curve: the maximum load, P_{max}, the maximum displacement, h_{max}, and the elastic unloading stiffness, $S=dP_{max}/dh_{max}$, which is defined as the slope of the upper portion of the unloading curve during the initial stages of unloading as shown in Fig. 12. The relationship between hardness (H) and Young’s modulus (E) can be expressed by the following equation [15]:

$$\frac{P}{S^2} = \frac{\pi}{(2\beta)^2}\frac{H}{E^2} \tag{1}$$

where β is the correction factor and β =1.0226 for the Berkovich diamond indenter [15]; P is load force and S is stiffness. Fig. 15 shows the correlation relation of P/S^2 and H/E^2. The experiments results are shown using solid dots. The theoretic P/S^2 value is calculated from Equation 1. The experimental data are distributed around the theoretical line. So P/S^2 and H/E^2 can be expressed with a linear relation.

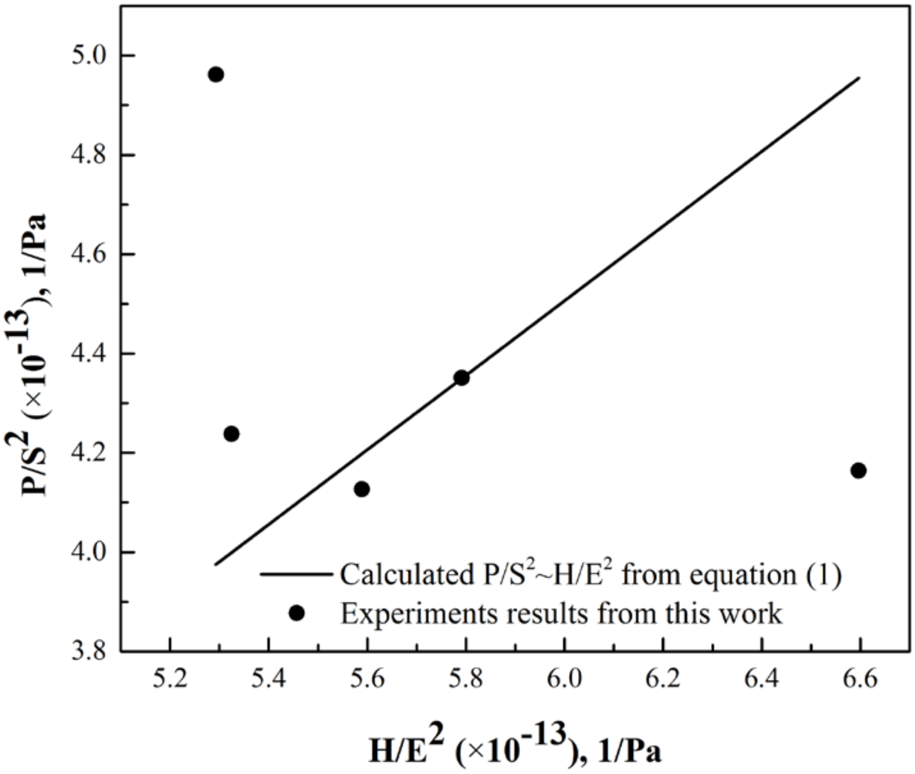

Figure 15: Nanoindentation P/S^2 vs. H/E^2

Task 3.2: Bond strength between the LZ top coat and bond coat

Sufficient adhesion bond strength between top coat layers and bond coat is an important property for the TBCs systems because durability and integrity of coating depend on the adhesion bond strength. Bond strength experiments were performed in this study to investigate the adhesion bond strength following ASTM C633. Epoxy (FM 1000 adhesive film) was used to glue the TBCs top coats to two cylinders. This bonding agent is capable of bonding the coating to the loading fixture with a tensile strength which is at least larger than the minimum required adhesion strength of the coating. Besides, this FM 1000 has sufficient viscosity not to penetrate through the coating. The adhesion or cohesion bond strength can be calculated by dividing the maximum load with the coating area.

Only the SCL LZ and 8YSZ coating samples (sample 6 and sample 9) were investigated for the bond strength test. Because the adhesion bond strength is affected by various interfaces and layers in multiple layer coats, it is difficult to determine the adhesion bond strength at a specific interface for DCL.

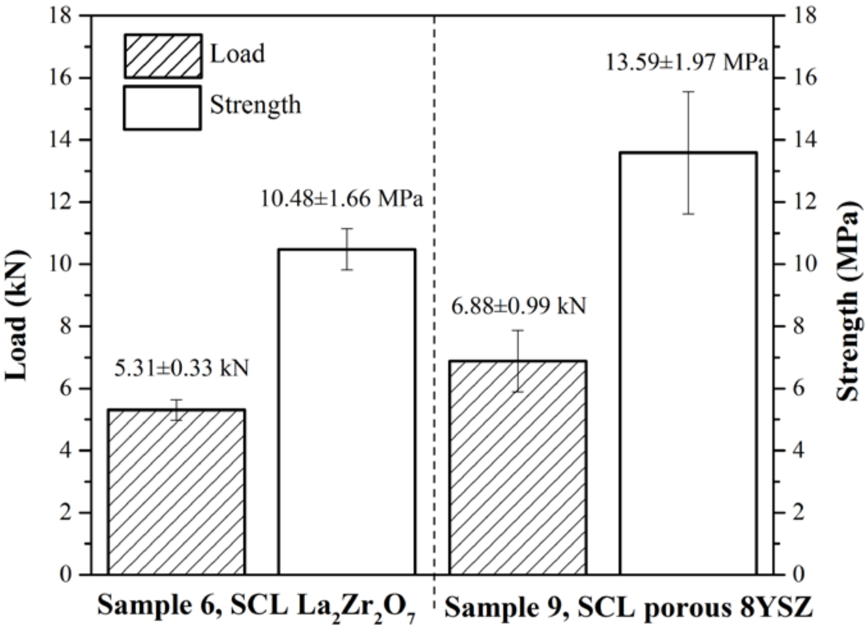

Figure 16: Load and bond strength results of bond strength test.

As shown in Fig. 16, the SCL 8YSZ sample can resist higher load, so it has higher adhesion bond strength than SCL LZ coating. When the tensile stress is lower than the adhesion bond strength, the TBCs are intact. Local fracture occurs when the tensile and shear stresses in the coating layer equal to the adhesion bond strength. There are typically two failure mechanisms: (1) the residual stress enhances the defects inside the ceramic layer, which leads to delamination, (2) increasing tensile and shear stresses enhances the tendency of cracking [16].

The LZ coats have lower fracture toughness than 8YSZ coats (2.2~3.3 MPa·m^{½} for YSZ and 1.1 ± 0.2 MPa·m^{½} for LZ), which means LZ coats are easy to break [17-19]. As a result, the SCL LZ coating sample has a lower adhesion bond strength than SCL porous 8YSZ.

Fig. 17 shows the cross-sectional SEM images of the TBCs systems after the bond strength tests. There is almost no TGO layer at the interface between the top and bond coat, so TGO layer is not the cause of spallation. The spallation occurs predominantly near the interface between the top coat and the bond coat, and the spallation did not occur exactly at the interface. Although the porosities of LZ and 8YSZ are similar, the LZ coats samples have scattered 'splats' grains. The SEM image shows the net-shape cracks inside the LZ layer. The cracks are easy to propagate in grain boundaries. However, in the remnant 8YSZ layer, it shows fewer grain boundaries but much larger pores than LZ. So there are fewer initial crack resources in the 8YSZ and its grains are connected better than LZ.

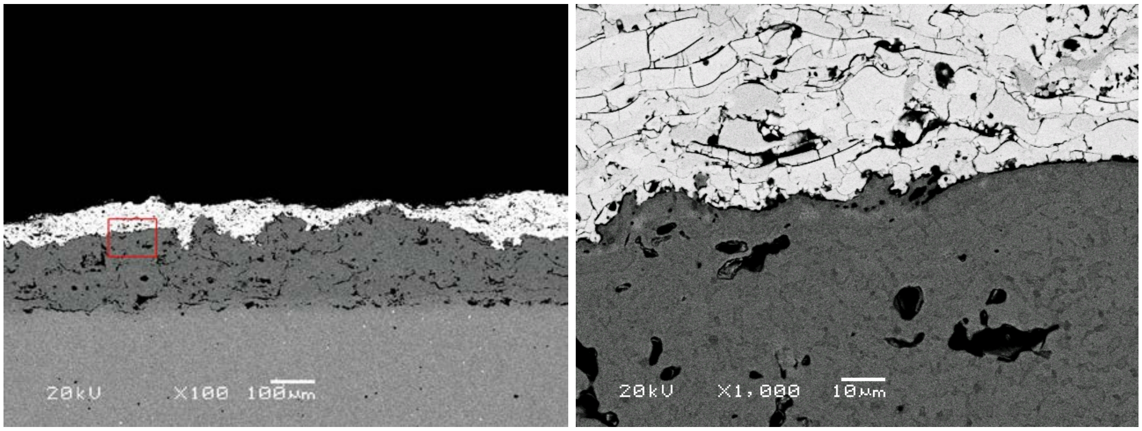

(a) (b)

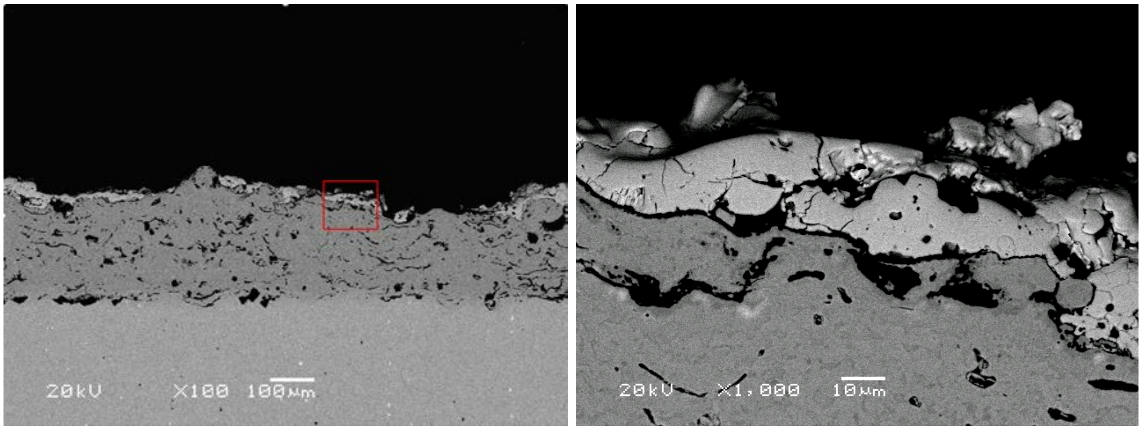

(c) (d)

Figure 17: SEM images at the interface of SCL LZ and 8YSZ coating at different magnifications. (a) Sample 6, magnification x100, (b) Sample 6, magnification x1000 (c) Sample 9, magnification x100, (d) Sample 9, magnification x1000.

Task 3.3: Erosion resistance

Erosion resistance tests were performed following ASTM G76-13. Alumina sand with a particle size of 50 µm was used as the erosive material, and 600 g sand was used for each sample. The speed of sand flow stream is 6 g/s with an impingement angle of 20^{o}. The erosion rate (mg/g) is used to evaluate the erosion resistance property in this experiment, which is calculated by dividing TBCs erosion weight (mg) by the abrasive flow weight (g).

Fig. 18 summarizes the erosion rate results for the four TBCs systems. SCL porous 8YSZ coating sample has the lowest erosion rates, which is about only half of the other samples erosion rate. The erosion rates of all LZ coating layers are much higher than 8YSZ. However, the DCL dense 8YSZ + LZ has relatively lower erosion rates than other SCL and DCL LZ based coatings.

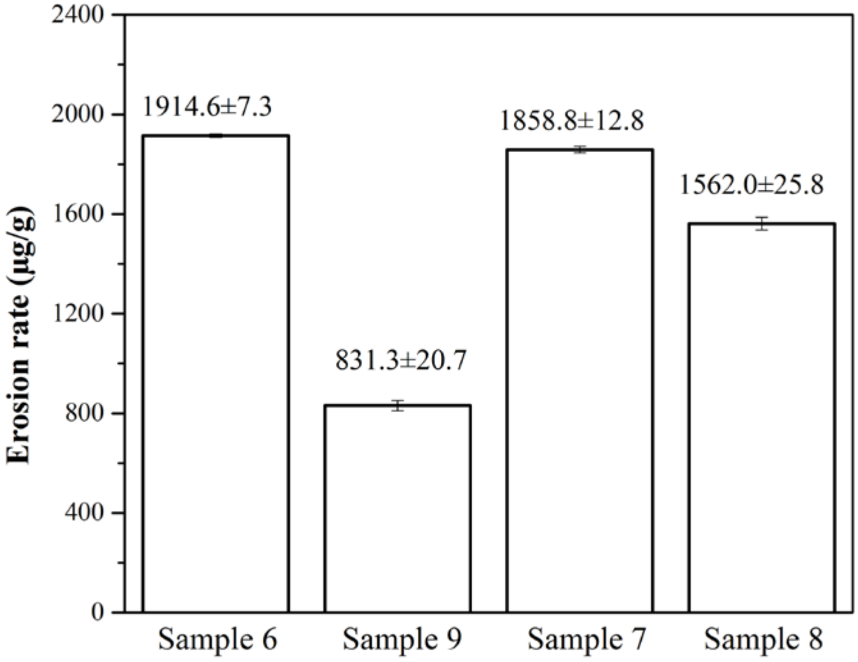

Figure 18: Erosion rates from erosion tests .of TBC samples.

Fig. 19 shows the optical micrographs of TBCs samples after the erosion experiments. Although the single layer 8YSZ TBCs have lower erosion rate, the center of this coating system was penetrated, as shown in Fig. 19d. The substrate of sample 9 was exposed, so this small hole can lead to lethal failure of the whole coating system. Similarly, the bond coats of both sample 6 and 7 were penetrated, as shown in Figs. 19a and 19b. Fig. 19b shows three concentric ellipses, which separate LZ, porous 8YSZ, the bond coat and substrate respectively from outside to inside. The dark solid ellipse area in Fig.19c is the dense 8YSZ layer, which was not penetrated. However, all the LZ top coat layer and some of 8YSZ layer was removed in this ellipse region.

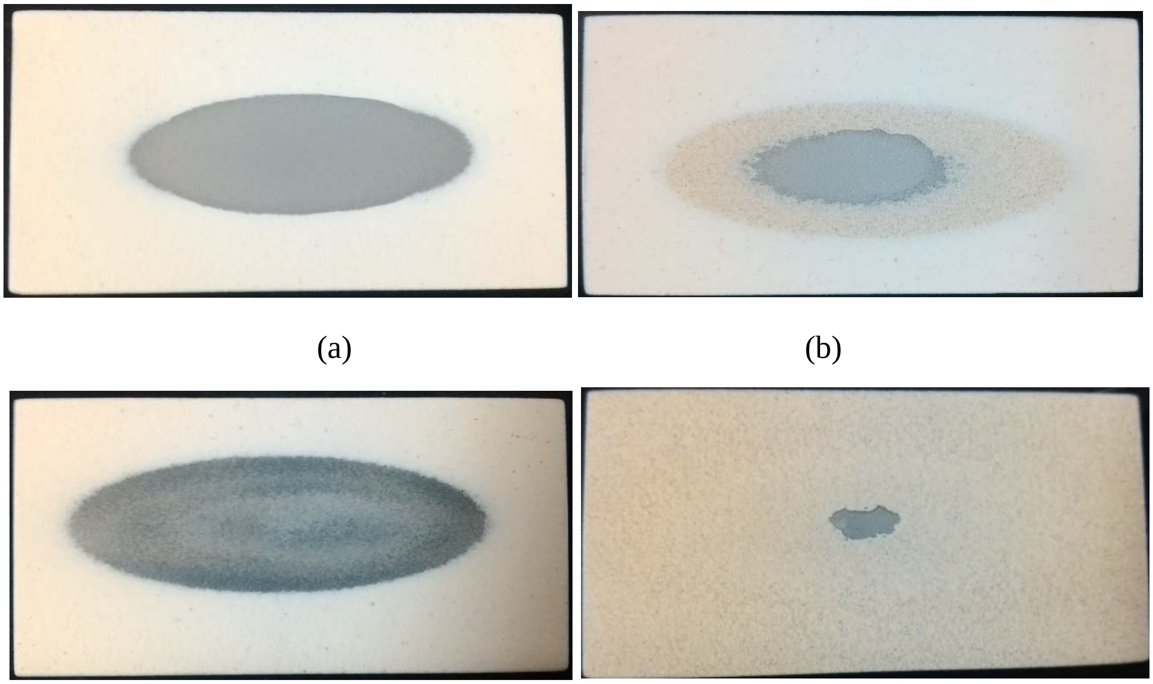

(a) (b)

(c) (d)

Figure 19: Optical images of erosion test: (a) sample 6, SCL porous LZ coating (b) Sample 7, DCL Porous 8YSZ + LZ coating, (c) Sample 8, DCL dense 8YSZ + LZ coating, (d) sample 9, SCL porous 8YSZ coating.

The cross-sectional SEM images of the erosion samples, which were passed through the erosion area, are shown in Fig. 20. As shown in Fig. 20a, the removed part is very large in LZ coating layer, but both two sides are still connected with the substrate. For the DCL porous 8YSZ plus LZ coatings shown in Fig. 20b, both two layers of top coats are removed in the center. More porous 8YSZ material is left than LZ. The interfaces between each layer are connected well. As shown in Fig. 20c although there is a big loss of LZ, the dense 8YSZ layer is almost intact. The interface between dense 8YSZ and substrate is also well connected. As shown in Fig. 20d, although the erosion hole is relatively small, the porous 8YSZ top coat in this cross-sectional image is almost delaminated from the substrate.

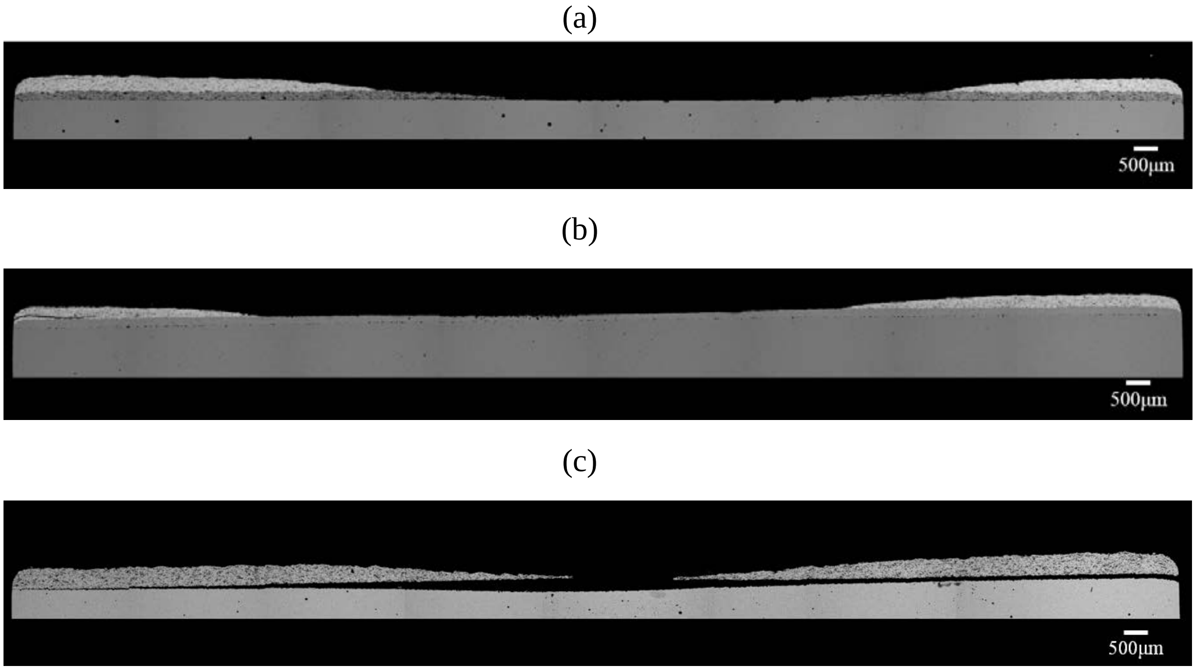

(a)

(b)

(c)

(d)

Figure 20: Cross sectional SEM images of the erosion panels: (a) sample 6, SCL porous LZ coating (b) Sample 7, DCL Porous 8YSZ + LZ coating, (c) Sample 8, DCL dense 8YSZ + LZ coating, (d) sample 9, SCL porous 8YSZ coating.

The SEM images at the edge of the erosion areas are shown in Fig. 21. As shown in Fig. 21a and Fig. 21b, both the SCL porous 8YSZ and SCL LZ layers were delaminated from the substrate at the interface. However, the double-layer coatings have better interfaces, as shown in Fig. 21c and Fig. 21d.

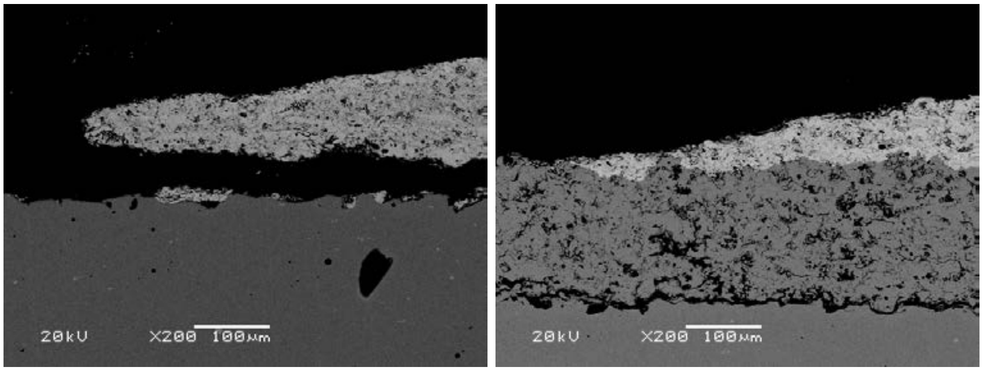

(a) (b)

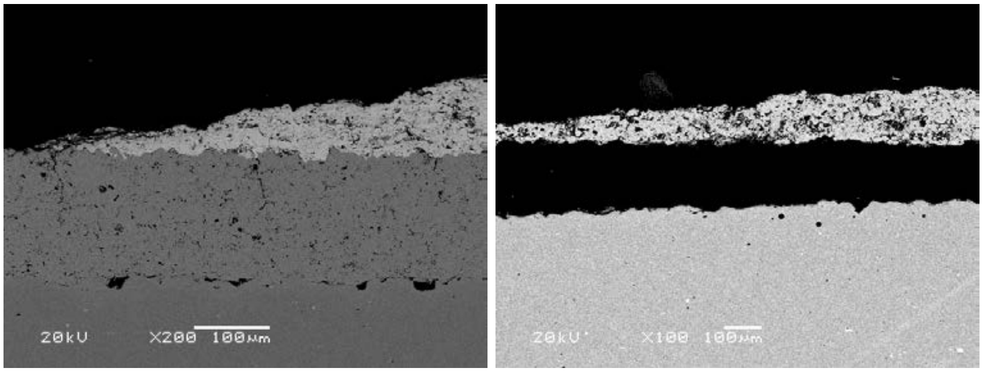

(c) (d)

Figure 21: SEM images of the cross sectional view of the erosion edge area: (a) Sample 6, SCL porous LZ coating (b) Sample 7, DCL Porous 8YSZ + LZ coating, (c) Sample 8, DCL dense 8YSZ + LZ coating, (d) sample 9, SCL porous 8YSZ coating.

8YSZ coats show better erosion resistance performance than LZ coats, mainly because the fracture toughness of 8YSZ is higher than LZ. Besides, the hardness values of dense 8YSZ layers are higher than other TBCs coat layers, as discussed above, so the erosion rate of this coat is the lowest.

Erosion models of brittle materials such as TBCs can be described using the indentation theory of erodent particles, which focuses on the relationship between TBC material properties, such as the Young's modulus and fracture toughness, and the erosion process conditions, such as impact velocity and abrasive particle size [24-27]. It is necessary to determine whether an impinging particle will initiate cracks in the target material. The velocity threshold is used to express the critical condition to initiate the crack. Wellman proposed that the critical velocity for the erosion can be given by [28]:

$$V_{crit} = 105 \frac{E^{3/4} K_{IC}^{3}}{H^{13/4} \rho^{1/2} R^{3/2}} \tag{2}$$

where E is Young's modulus, H is hardness, K_{IC} is fracture toughness, ρ is the density of the erodent particle and R is the particle radius. Since LZ has a lower K_{IC} than 8YSZ, low erosion resistance of LZ in the erosion test is expected [29].

The calculated critical erodent velocities of each sample are shown in Fig.22. The critical velocities of LZ coating layer are much lower than 8YSZ. So the erosion rate of SCL LZ TBCs is larger than SCL 8YSZ TBCs. Comparing sample 7 DCL porous 8YSZ+ LZ with sample 8 DCL dense 8YSZ+ LZ, the critical velocity of top layer LZ in samples 8 is larger than sample 7, so sample 8 has a larger erosion rate than sample 7.

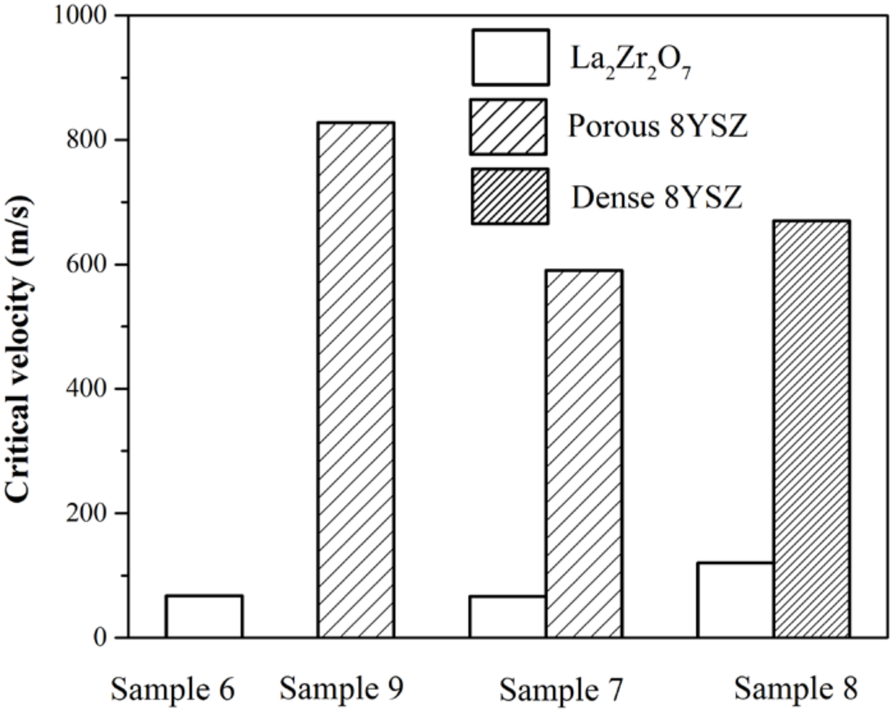

Figure 22: Critical erodent velocities of TBC samples.

Fig. 23 shows the reciprocal values of the critical velocity as a function of erosion rate. The measured data points can be fitted into a linear function, y=9.56e^{-6}x-0.00739.

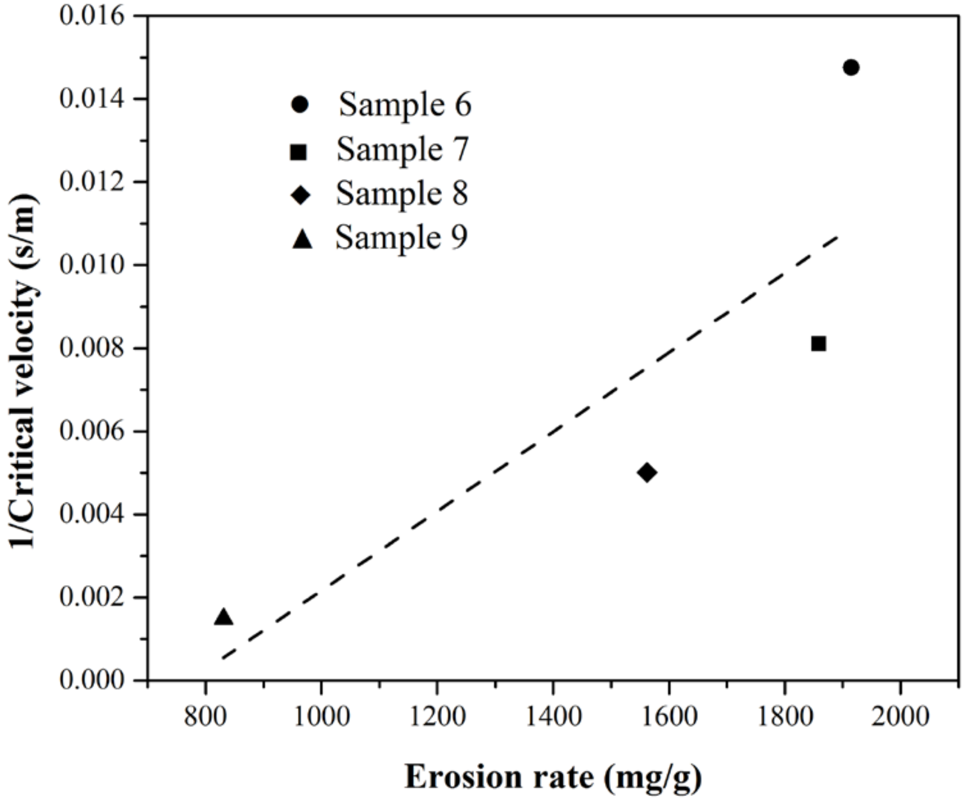

Figure 23: Relationship between critical erodent velociyies and erosion rate.

Task 3.4: Thermal conductivity of LZ coatings

For thermal barrier coating materials, one of the most important material properties is the thermal conductivity. There are several experimental methods to measure thermal conductivity. The most common one is the flash method, which was first proposed by Parker *et al.* [30]. Three thermal properties - thermal diffusivity, specific heat capacity, and thermal conductivity can be deduced simultaneously using one sample [30]. The flash method is designated as the standard thermal diffusivity method specified in ASTM E1461-11. The measurement error of the standard flash method is less than 5 % [31].

In this work, the thermal conductivities were calculated from thermal diffusivity $D_{th}(t)$, specific heat capacity $C_p(t)$ (from literature[18]) and measured density $\rho(t)$ [12]. The thermal diffusivities $D_{th}(t)$ were measured by flash diffusivity systems (TA instrument DLF1200, Delaware, USA).

The thermal conductivities of the as-sprayed single-layer porous LZ and porous 8YSZ coatings (sample 6 and sample 9) are plotted in Fig.24. Three thermal conductivity measurements were conducted for the LZ coatings at each temperature setting (297 K, 377K, 477K, 579K, 676K, 776 K, 874 K, 974 K, 1072K and 1172 K). The measured average thermal conductivity of the LZ was about 0.59-0.68 W/m/K in the temperature range of 297 to 1172 K (24 -899 ^{o}C), which was about 25% lower than that of the porous 8YSZ (0.84-0.87 W/m/K) in the same temperature range. The thickness of the porous LZ top coat varies from 450 to 550 μm. The density of sprayed LZ coating is 5.35 g/cm^3, and the corresponding porosity is 11.54 %. The porosity is essential for reducing thermal conductivity while maintaining resisting fracture, erosion and foreign object damage [32].

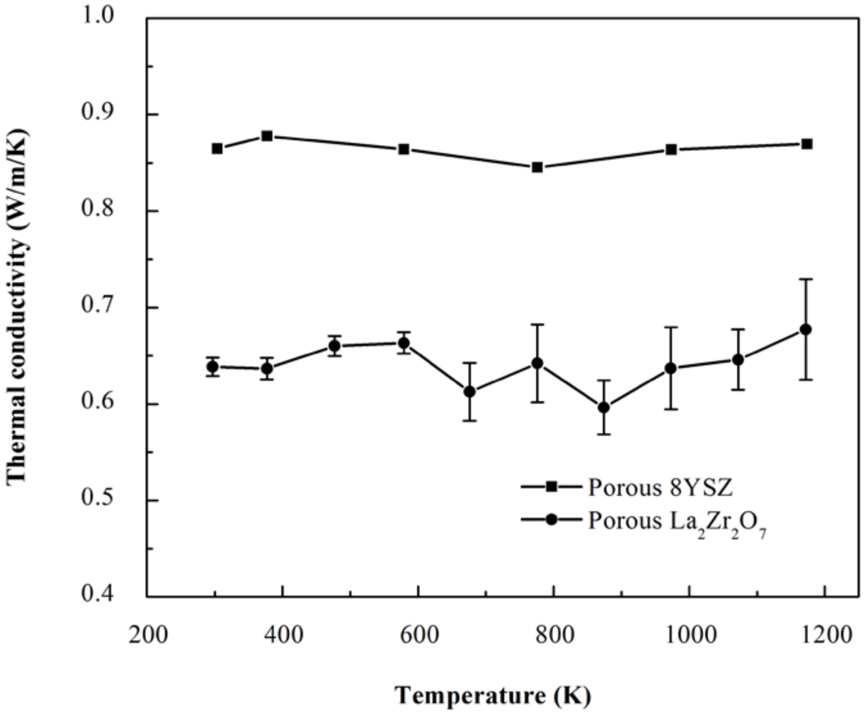

Figure 24: Temperture-depdendent thermal conductivity of sample 6 and sample 9.

The curves are a guide to the eye.

Task 3.5: Coefficient of thermal expansion of LZ coatings

The thermal expansion coefficients CTEs (sample size 5 mm in width, 25 mm in length and 0.43 mm in thickness) were measured by using a BAEHR dilatometer DIL 802 (now belonging to TA instrument, Delaware) at temperatures ranging from room temperature to 1673 K (1400 ^{o}C).

The CTE values measured on sample 6 SCL porous LZ coating and sample 9 SCL porous 8YSZ coating are shown in Fig. 25. CTE values of LZ change very little when the temperature is above 400 K. The CTE values of the LZ were about 9 -10×10^{-6} K^{-1} from 400 K (127 ^{o}C) to 1600 K (1327 ^{o}C), which were very close to the reported literature data [12, 33, 34]. Although the porosity of 8YSZ coating was higher than that of the LZ coating, the CTE values of the LZ were about 10% lower than those of the porous 8YSZ, which were 10-11×10^{-6} K^{-1} in the same temperature range [35, 36]. This indicates that the LZ coating can have lower CTE than 8YSZ coating if they are in the same porosity level. Due to the difference of CTE between the 8YSZ and the LZ, a thermal mismatch can be generated at the interface between the 8YSZ sublayer and the LZ top layer during the thermal shock and thermal cycling tests. As the NiCrAlY bond coat has much higher CTEs (about 15×10^{-6} K^{-1} at 1273 K) than the 8YSZ [9], a larger thermal mismatch between the bond coat and the LZ top coat are expected during thermal shock and thermal cycling tests.

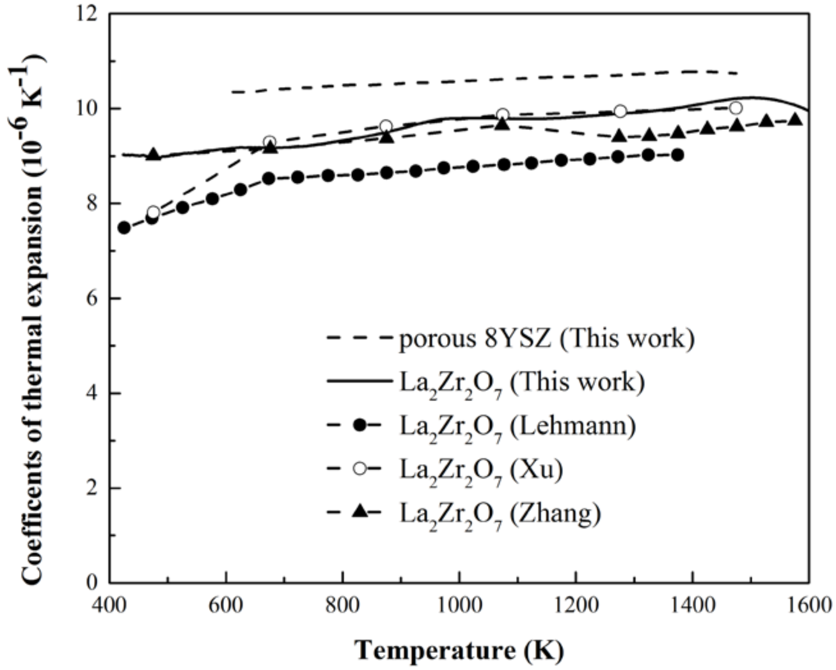

Figure 25: Temperature-dependent CTE values of LZ and 8YSZ.

Task 4: Modeling of residual stresses, mechanical and thermal properties in TBCs

Task 4.1: Analytical modeling of residual stresses in TBCs

Since the sprayed coating samples are cooled in ambient environment from the elevated deposition temperatures, thermal residual stress is generated in the TBCs layers, due to the different coefficients of thermal expansion in each TBCs layers. These residual stresses are mainly from the strain mismatch between the coating layers and the substrate when the TBCs systems are cooled from high temperatures to room temperature. When the coatings are cooled from high temperatures, the substrate volume shrinks more than the coatings due to its higher coefficient of thermal expansion. Considering displace compatibility, compression stress is applied in the ceramic coating layers and tension stress is applied on the substrate. In order to calculate the residual stress in multiple-layer coatings, the interface between the substrate and the bond coat is defined as the origin line, where z=0. The distance from layers i to substrate is defined as h_i [20-22]. The thermal residual stress in the substrate and ith coating layer, which related to the misfit strain ε_i and bending curvature K, can be expressed by[20, 23]:

$$\sigma_s = E_s\left[\varepsilon_s + K\left(z+\delta\right)\right] \quad (-t_s \le z \le 0) \tag{3}$$

$$\sigma_i = E_i\left[\varepsilon_i + K\left(z+\delta\right)\right] \quad (1 \le i \le n,\ h_{i-1} \le z < h_i) \tag{4}$$

where E_s and E_i are Young's modulus of substrate and ith coating layer. δ is the distance from the bending axis, where the bending strain is zero. ε_i, ε_s, K and δ can be individually expressed by [23]:

$$\varepsilon_s = -\sum_{i=1}^{n}\frac{E_i t_i}{E_s t_s}\Delta\alpha\Delta T \tag{5}$$

$$\varepsilon_i = \Delta\alpha\Delta T + \sum_{k=1}^{n}\frac{E_k t_k}{E_s t_s}(\alpha_k - \alpha_i)\Delta T \tag{6}$$

$$\delta = \frac{t_s}{2} - \sum_{i=1}^{n} \frac{E_i t_i}{E_s t_s}\left(2h_{i-1} + t_i\right) \tag{7}$$

$$K = -\sum_{i=1}^{n} \frac{6E_i t_i \Delta\alpha \Delta T}{E_s t_s^{\ 2}} \tag{8}$$

where α is the coefficient of thermal expansion (CTE), k is the ceramic coating layers range from 1 to n, t_i is the thickness of ith layer.

The calculated thermal residual stresses from Equations 3-8, along with thermal residual stress results from the Townsend model, are shown in Fig. 26 [21]. The compressive residual stress difference at the interface of SCL LZ coat is about 3 GPa larger than SCL porous 8YSZ at ΔT= 400 K.

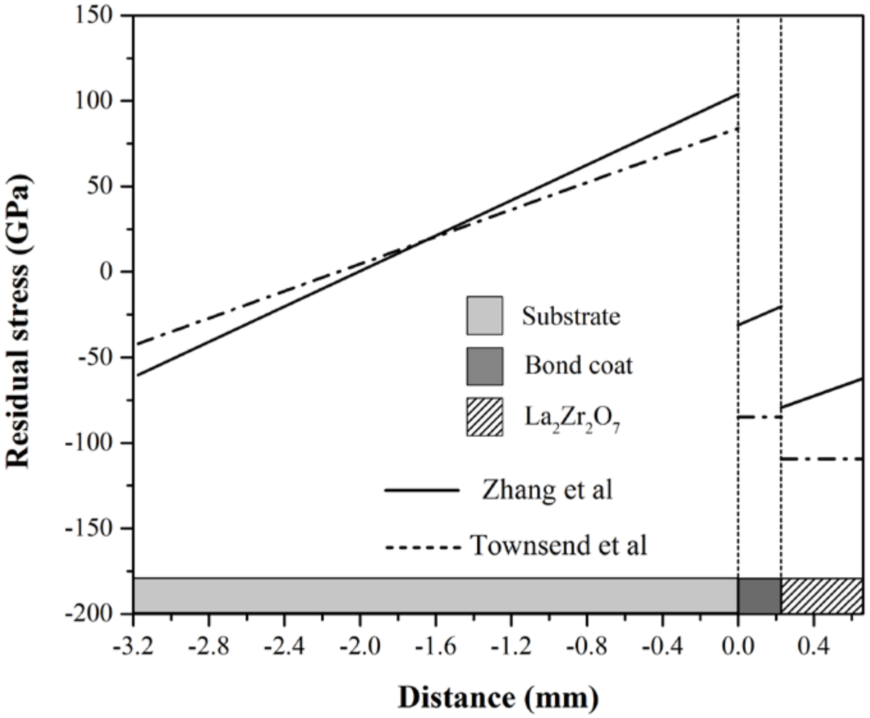

(a)

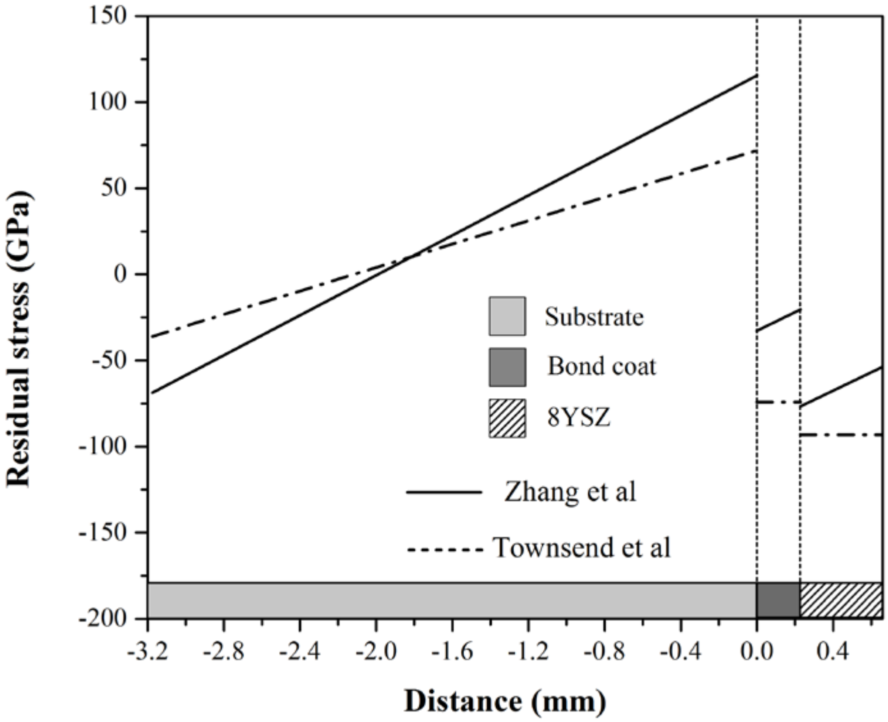

(b)

Figure 26: Residual stress distribution as a function of thickness with ΔT=400 K. (a) Residual stress distribution in Sample 6, SCL $La_2Zr_2O_7$ samples; (b) Residual stress distribution in Sample 9, SCL porous 8YSZ samples.

Due to the residual stress difference, there will be more defects, such as grain boundaries and pores, near the interface area of SCL LZ TBCs, which corresponds to Figs. 17b and 17d. Since there are more distributed grain boundaries in LZ than 8YSZ, so the LZ ceramic layers are easily to break. Besides, comparing to the interface, the LZ layers are much weaker due to its lower fracture toughness and scattered boundaries[17]. So the spallation occurs inside the LZ coating layer instead of the interface. The magnitude of residual stress in SCL LZ TBCs is larger than 8YSZ. The bond strength in LZ TBCs samples is lower than 8YSZ, which shows that the spallation occurs easier in LZ coating than 8YSZ. This can be attributed to the lower fracture toughness of LZ and higher residual stress in the LZ coating layer, as previously mentioned.

Task 4.2: DFT and MD modeling of mechanical properties of LZ

4.2.1 Introduction

Although the low thermal conductivity of LZ is an advantage for the application of TBCs, LZ has been also reported that it has lower Young's modulus, hardness, and lower fracture toughness than 8YSZ [18]. As discussed previously, the thermal cycling performance of the single layer LZ TBC is worse than that of 8YSZ, which might be due to the low coefficient of thermal expansion (CTE) and poor mechanical properties of LZ [40, 45]. As a result, the investigation of the mechanical property of LZ would be very important for systematically understanding the LZ materials. Tensile and shear stress-strain relations of single crystal LZ exhibit many anisotropic mechanical properties. However, single crystal LZ samples are difficult to obtain. Since it is hard to measure the intrinsic mechanical properties of perfect LZ in experiment due to its porous characteristics, theoretical modeling techniques can be used to study the mechanical properties.

The most widely used theoretical method to investigate the mechanical properties is the analytical method based on Voigt-Reuss-Hill's theories, which calculates the elastic moduli from the elastic constants [46-48]. The elastic constants can be computed using the first principles calculations based on the density functional theory (DFT) [49, 50]. In addition, the nanoscale tensile and shear simulation can be conducted using the DFT and MD calculations directly. The uniaxial nanoscale-tensile strain can be applied stepwise in the tensile direction. The shear strain can be applied stepwise by changing the crystal angle. After the full relaxation at each strain stage, the tensile and shear stresses can be computed using the DFT or MD calculations.

Although several methods have been developed to conduct the nanoscale tensile and shear simulations, to our best knowledge, no such investigation has been performed on LZ material. In this work, the single LZ crystal model was built and the lattice parameter of LZ conventional unit cell was calculated by minimizing the total system energy. The nanoscale tensile and shear stress-strain relations of single crystal LZ were investigated using the DFT and MD method. The corresponding elastic moduli were calculated using two approaches: stress-strain curve analysis in large deformation and Voigt-Reuss-Hill approximation in small deformation [46, 51]. Toughness was calculated based on the stress and strain curves as well. Average Bader charge difference and charge density distribution were used to explain the influence of election interaction on Young's modulus.

4.2.2 DFT LZ models

In this work, the DFT calculations were conducted using Vienna Ab initio Simulation Program (VASP) [52, 53]. The exchange-correlation potential was specified using projector augmented wave (PAW) method of generalized gradient approximation (GGA) functional. The Brillouin zone k-point of was conducted using 3×3×3 Monkhost-Pack scheme. A conjugate-gradient algorithm was used for the ironic relaxation. The plan-wave cutoff energy was 500eV. The energy relaxation criterion for the electron was 10^{-6}eV and the ionic relaxation convergence criterion was total forces smaller than 0.01 eV/A.

The LZ crystal is a cubic pyrochlore structure, which is belong to the space group of $Fd\overline{3}m$ [54]. There are four independent crystallographic atom sites, where La is at 16d at $(\frac{1}{2}, \frac{1}{2}, \frac{1}{2})$, Zr is at 16c at (0,0,0), O1 is at 48f at $(x, \frac{1}{8}, \frac{1}{8})$ and O2 is at 8b at $(\frac{3}{8}, \frac{3}{8}, \frac{3}{8})$. The x value of O1 varies from 0.3125 to 0.375. According to Tabira's experiments, 0.333 was chosen as the initial x value of LZ in this work [55]. The conventional LZ unit cell was used in the elastic constant calculation and the shear stress-strain calculations, as shown in Fig.27.

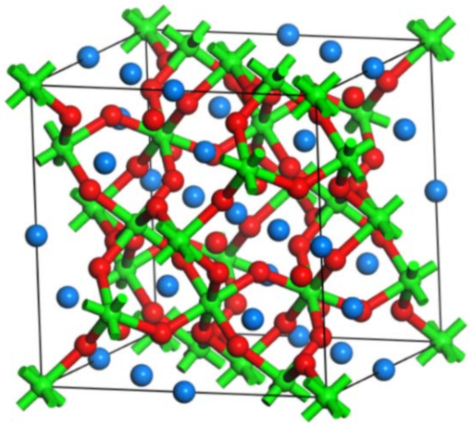

Figure 27: Crystal structure of LZ unit cell. Each ball shown as green, red, and blue indicates Zr atom, O atom and La atom, respectively (same coloring schemes are used in all figures afterwards).

To calculate the stress in a specific crystal direction, the LZ unit cell was rebuilt to align the (001), (011) and (111) surface perpendicular to the tensile axis for the tensile stress-strain calculations, as shown in Fig.28. The atom numbers of the (001), (011) and (111) model are 44, 44, 66 respectively. All of the LZ structures were relaxed before the elastic constant, tensile and shear calculations.

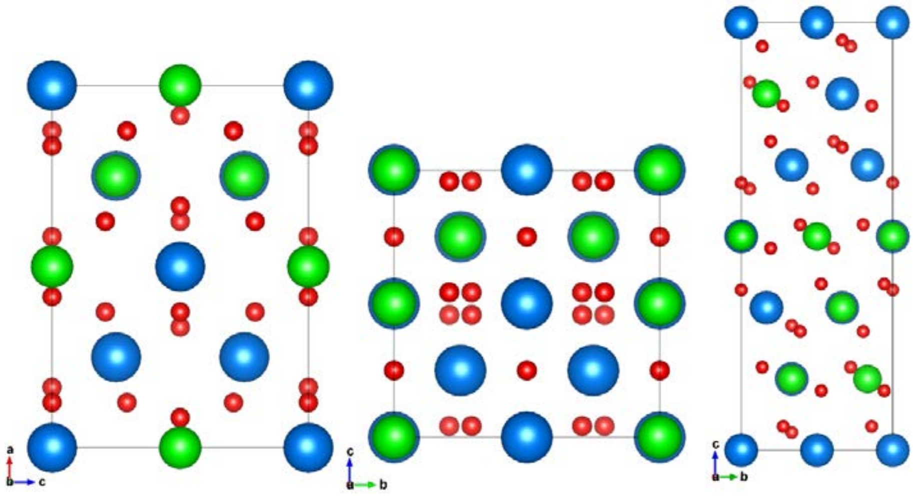

(a) (b) (c)

Figure 28: Tensile model at (a) [001] direction along a axis, (b) [011] direction along c axis, and (c) [111] direction along c axis directions. Each ball shown as green, red, and blue indicates Zr atom, O atom and La atom, respectively.

Large deformation stress-strain analysis and the small deformation elastic constant analysis were used to calculate the anisotropic elastic moduli. In the stress-strain analysis, the anisotropic Young's modulus and shear modulus in a particular tensile and shear direction were obtained from the slope of the linear fitted line in the elastic stage of the stress-strain curves. In the small deformation elastic constant analysis, Voigt-Reuss-Hill approximation was used to calculate the elastic moduli of LZ base on the elastic constants of single LZ unit cell. The elastic constants of LZ unit cell were calculated using DFT method by performing finite distortion of the LZ unit cell [56]. The Voigt proposed approach expresses the stress in a single crystal in terms of the given strain. On the other hand, the Reuss proposed approach expresses the strain in terms of the giving stress. The Voigt-Reuss-Hill approximation calculated the effective moduli of an aggregated polycrystalline combined the Voigt and Reuss's approximation [46, 57]. For cubic single crystal LZ, only 3 elastic constants are independent (C_{11}, C_{12}, C_{44}). The effective bulk modulus (K), shear modulus (G), Young's modulus (E) and Poisson's ratio (υ) of cubic LZ crystal can be calculated using following equations:

$$K = \frac{C_{11}+2C_{22}}{3} \tag{9}$$

$$G = \frac{G_R+G_V}{2} \tag{10}$$

$$E = \frac{9KG}{3K+G} \tag{11}$$

$$\upsilon = \frac{3K-2G}{2(3K+G)} \tag{12}$$

where G_V and G_R are the shear modulus expressed by the Voigt and Reuss approach, respectively [46, 57].

$$G_V = \frac{(C_{11}-C_{22})+3C_{44}}{5} \tag{13}$$

$$\frac{5}{G_R} = \frac{4}{C_{11}-C_{22}} + \frac{3}{C_{44}} \tag{14}$$

The slip system (easy slip plane and direction) in the shearing process often occurs on the plane of high atomic density in closely packed directions [58]. For example, the primary slip system for face center cubic (fcc) crystal is {111}<110> and the secondary slip direction is {111}<11$\bar{2}$>. Because the {111} is the closest packed plane in LZ crystal, the most possible slip direction is along {111}<110> and {111}<11$\bar{2}$> directions. The conventional unit cell of LZ was used in the shear stress calculation, as shown in Figure . The shear directions were controlled by rotating the LZ unit cell to align the slip plane perpendicular to one of the coordination axes. The shear strain was applied by changing the angle in the shear directions. The shear stress was calculated using first principles calculations corresponding to each strain step.

Bader charge transfer analysis in tensile and shear DFT model was conducted to describe the electron gain and loss between different atoms [59, 60]. The average charge differences between Zr, La and O were calculated from the Bader charge results, which gave the insights of atom bonding character in different orientations.

4.2.3 DFT LZ crystal lattice parameter optimization

The crystal constant or geometry optimization was calculated by minimization of the total system energy. The interatomic potential energy is the sum of the repulsive energy and attractive energy. The potential energy (E) as a function of interatomic distance (r) is shown in Fig.29 [64]. In a two atoms system, when r is smaller than the equilibrium distance r_0, the repulsive energy increases and attractive energy decreases which result to a repulsive force on the atoms. Therefore, the atom pair will be pushed away. On the other hand, when r becomes larger than r_0, the attractive energy take advantage to pull the atoms together. When the equilibrium distance r_0 between the two atoms is reached, the total energy reaches its lowest value. In a crystal system, the crystal constant that has the minimum total energy can be regarded as the equilibrium state of the system, which means the system has the highest possibility to balance the repulsive and attractive forces among atoms. As a result, the lattice constants can be obtained by analyzing the relations between the total energy and the lattice parameters.

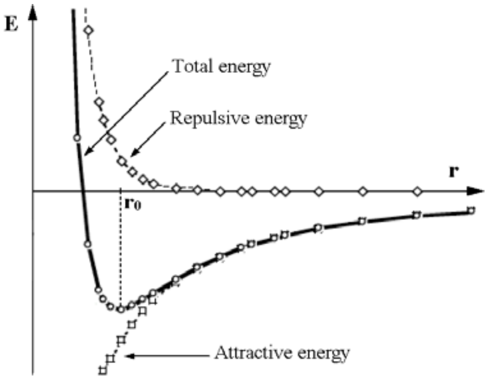

Figure 29: Potential energy vs. interatomic distance.

Since LZ is a cubic crystal, it has only one lattice constant. The actual LZ lattice constant was determined by finding the minimum point on the curve of the total energy as a function of lattice constant. Fig.30 shows the DFT calculated total energy of single LZ conventional cell as a function of lattice constant. This work tested the lattice constant of LZ model from 9 Å to 12 Å, which has a wide enough range to contain the actual LZ lattice constant. The calculation results indicated that the equilibrium state of the system occurred at the lattice constant of 10.875 Å, where the total energy reached its minimum point of -803.749 eV.

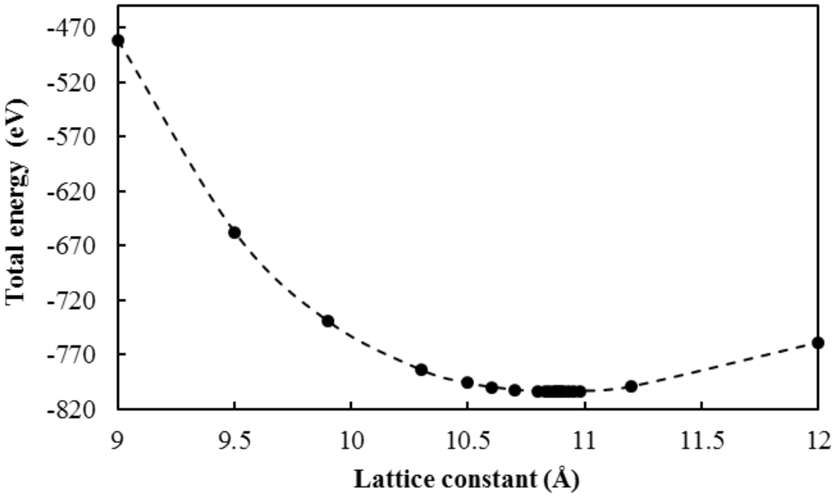

Figure 30: Total energy as a function of LZ lattice constant.

To validate the DFT calculated results, the lattice constant of LZ powders was analytically calculated from XRD experimental data, as shown in Fig. 2. Bragg's Law was used to analyze the XRD data:

$$n\lambda=2d\sin\theta \tag{15}$$

where λ=1.54 Å for the laboratory XRD used in this work, n=1. The lattice parameters can be derived from *d* and Miller indices <h k l> of each XRD peak. specifically, for cubic unit cell, lattice parameter (a_0) can be expressed by:

$$d_{hkl}=\frac{a_0}{s}, \text{ where } s=\sqrt{h^2+k^2+l^2} \tag{16}$$

The calculated lattice constant from several XRD peaks. The average lattice constant of LZ powders obtained from XRD experimental data is 10.801 Å. Shimamura and Tabira's experiment results of the LZ lattice constant are 10.8 Å and 10.802 Å, respectively, which are the same as the XRD experimental results in this work [55, 65]. The difference between the DFT calculated result and the XRD experiments result is 0.68%. The DFT calculated lattice constant of LZ is very accurate.

4.2.4 DFT calculations of tensile and shear stress-strain curves and anisotropic elastic moduli

4.2.4.1 Large tensile and shear deformation stress-strain curves

The single LZ cell nanoscale models used for DFT tensile and shear simulations were (001), (110), (111) and conventional LZ cell, respectively. The ions positions of all the DFT models were relaxed using conjugate-gradient algorithm before and in the deformation calculations. In the tensile simulation, the model is uniaxial elongated in the z-direction, so the tensile stress acquired directly from stress tensor in the z direction.

Fig.31 shows the tensile stress-strain curves calculated using the first principles calculations. The linear elastic stage on these curves only occurred in the first a few steps, then the stress drops slowly after it reached the ultimate tensile strength. The LZ tensile model in [001] direction has the largest ultimate tensile strength, and the LZ tensile models in [110] and [111] directions have similar ultimate strength. Young’s modulus can be calculated from the slope of the linear section in the curve using Hooke’s law. The Young’s modulus in [001], [110] and [111] directions were obtained from the slope of the linear fitted line, which corresponds to the strain from 0 to 0.1 for [001] direction, and from 0 to 0.08 for [111] and [110] directions. The toughness can be calculated from the integration of the area under the stress-strain curve.

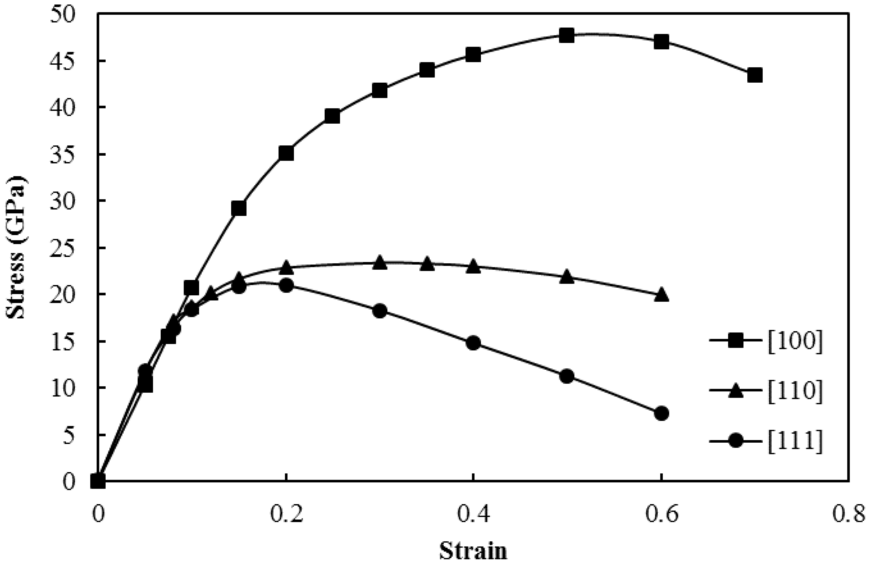

Figure 31: DFT calculated tensile stress-stain curve.

The calculated Young’s modulus, ultimate tensile strength, and toughness are summarized in Table 5. The single crystal LZ has the maximum tensile Young’s modulus in [111] direction, and minimum Young’s modulus in [001] plane, this trend is consistent with Liu ‘s results [66]. In the nanoscale DFT simulations results, the quasi-plastic deformation stage occurred on the stress-strain curves rather than the ideally elastic-brittle type [67]. The stress and strain were largely increased during the quasi-plasticity stage, which determined the magnitude of ultimate strength and toughness. Although Young’s modulus in [001] direction was lower than that in [110] and [111] directions, the tensile stress-strain curve in [001] direction possessed a higher “yield” point in quasi-plasticity stage than that in [110] and [111] directions. As a result, the LZ tensile model in [001] direction possessed the maximum ultimate strength and toughness. The ultimate strength and toughness are properties of large deformation; however, Young's modulus is a property of small elastic deformation. These properties describe stress-strain relations under different deformation circumstances, so they can exhibit the different trend.

Table 5: Calculated elastic modulus, ultimate strength, and toughness

Calculation model	Elastic modulus (GPa)	Ultimate strength (GPa)	Toughness (MJ/m^3)
DFT Tensile [001]	207.211	47.747	21.565
DFT Tensile [110]	213.225	23.453	12.219
DFT Tensile [111]	222.596	20.980	8.934
MD Tensile [001]	230.355	30.250	3.018
MD Tensile [110]	226.897	18.867	2.192
MD Tensile [111]	229.751	18.914	1.839
DFT Shear {111}<110>	76.037	22.507	8.862
DFT Shear {111}<11$\bar{2}$>	73.381	20.192	8.028
MD Shear {111}<110>	-	29.008	-
MD Shear {111}<11$\bar{2}$>	-	20.774	-

Fig.32 shows the DFT calculated shear stress-strain curves in two slip systems {111}<11$\bar{2}$> and {111}<110>. Basically, the two curves are very similar. As summarized in Table 5, the shear modulus of {111}<110> is slightly larger than that of {111}<11$\bar{2}$>, and so as the ultimate shear strength and the toughness, although the differences are very small. When the two slip systems of LZ crystal are under same stress level, the corresponding strain in {111}<11$\bar{2}$> direction will be larger than that in {111}<110> direction. Based on these DFT calculated results, in single crystal LZ material, the {111}<11$\bar{2}$> direction system is more likely to slip in the shear simulation.

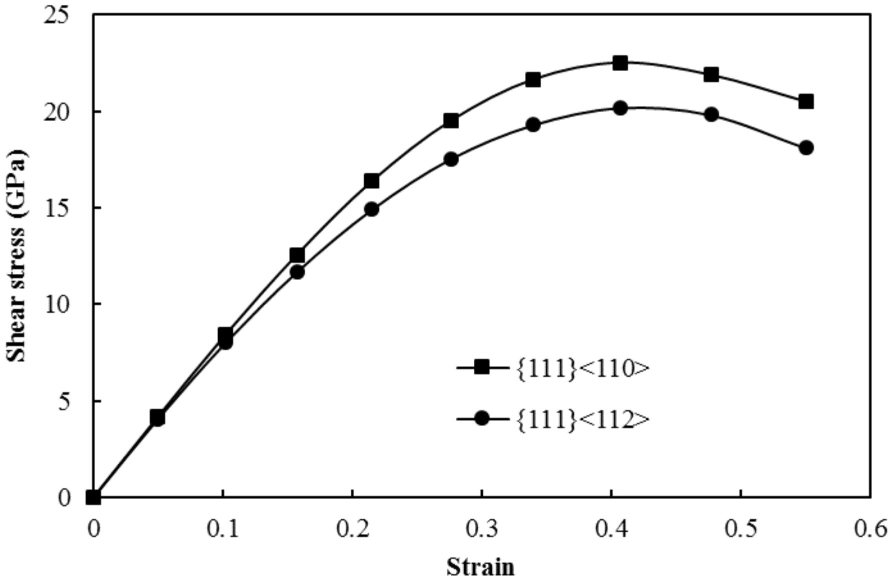

Figure 32: DFT calculated shear stress-stain curves.

4.2.4.2 Small deformation elastic moduli calculations

The elastic constants C_{11}, C_{12} and C_{44} of LZ single crystal were calculated using DFT method in small deformation condition, which were 256.001 GPa, 116.425 GPa and 86.708 GPa, respectively. The effective elastic moduli of LZ were calculated using Equations 9-14, as summarize in Table 6. Selected experimental results from the literature were also listed in Table 6 as a comparison. In these literature results, Zhang *et al.* measured Young's modulus of 7% porous LZ coating using nanoindentation [8], and Shimamura *et al.* studied the moduli of LZ materials using the ultrasound pulse-echo measurement [65]. Comparing with the experimental data from the literature, the effective moduli of the LZ are in a reasonable range.

Table 6: Calculated effective moduli of LZ, compared with expeirmental results

	Effective moduli	Experimental results
Young's modulus (GPa)	205.12	156±10 (Zhang [8]) 280 (Shimamura [65])
Bulk modulus (GPa)	162.95	216 (Shimamura [65])

Shear modulus (GPa)	79.49	109 (Shimamura [65])
Poisson’ s ratio	0.29	0.28 (Shimamura [65])

The anisotropic characteristics can be determined by Zener anisotropic ratio, which is defined as Z= $2C_{44}/(C_{11}-C_{22})$ [47]. If the Z = 1, the material is isotropic. The calculated Z value for LZ is 1.24, indicating that the elastic modulus of LZ is anisotropic, and the maximum Young’s modulus is in <111> direction. Anisotropic Young’s modulus of cubic LZ crystal can be expressed using the DFT calculated elastic constants, which is given by the following equations [47].

$$\frac{1}{E}=\frac{l^4+m^4+n^4}{E_0}+\frac{2(m^2n^2+n^2l^2+l^2m^2)}{F_0} \tag{17}$$

$$\frac{1}{E_0}=\frac{C_{11}+C_{22}}{(C_{11}-C_{22})(C_{11}+2C_{22})} \tag{18}$$

$$\frac{2}{F_0}=\frac{-2C_{12}}{(C_{11}-C_{22})(C_{11}+2C_{22})}+\frac{1}{C_{44}} \tag{19}$$

where l, m, n are directional cosines. The (110) plane was chosen in this work for the anisotropic calculation because it includes all three of the principal directions in a cubic crystal <111>, <110>, and <001>. The directional cosines for (110) plane can be calculated by:

$$l=cos\theta \quad m=\frac{\sin\theta}{\sqrt{2}} \qquad n=\frac{\sin\theta}{\sqrt{2}} \tag{20}$$

where θ is the angle in (110) plane, which measured from [100] direction to the [110] direction.

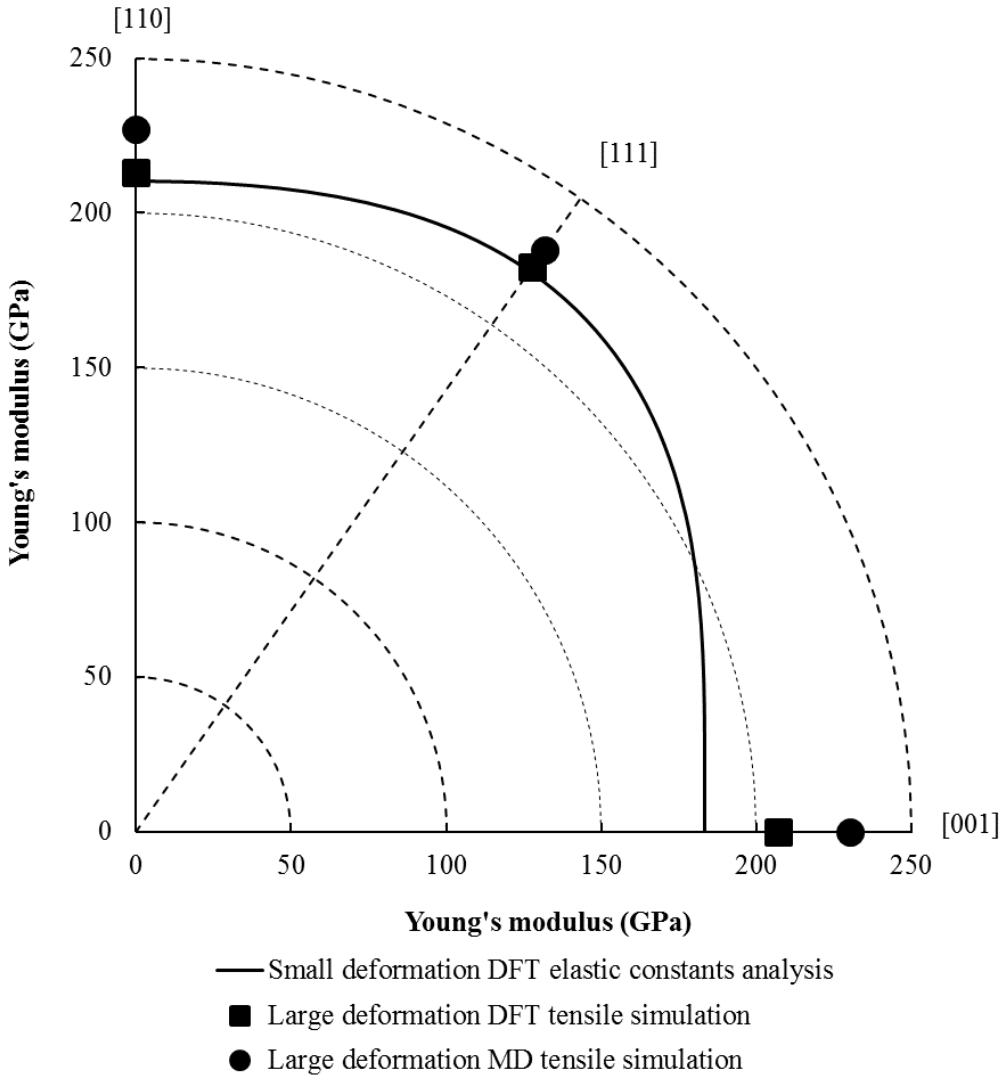

Figure 33: Anisotropic Young’s modului.

The anisotropic Young’s modulus results are plotted in Fig.33, including the solid curve calculated from the elastic constants of LZ single crystal in small deformation status, and the scattered points calculated from the DFT and the MD stress-strain curves in large deformation tensile simulation. As shown in Fig.33, most of anisotropic Young’s modulus results are very close to each other, suggesting that this modeling study has good consistency and accuracy.

4.2.5 DFT Bader charge analysis and charge density distribution

Bader charge transfer was calculated according to each atom in the tensile and shear systems. The unit of Bader charge is electron (e), which means that the number of the electrons one atom gains or losses. The average Bader charge difference of between cation and anion reveals the electron interaction between those two type of atoms, which related to the bonding character of those atoms. The high average Bader charge difference indicates the strong bond. Table 7 summarizes the Bader charge differences between cation and anion results in each tensile and shear calculations. The charge differences between Zr and O, and between La and O in tensile [111] calculation are the largest among the three tensile cases, suggesting the bonding strength in the tensile model in [111] direction are the strongest. The strong bond between the cation and anion in the [111] tensile model corresponding to the high Young's modulus result in DFT calculations. In the shear models, the average Bader charge difference in LZ shear model in {111}<110> direction are slightly larger than that in {111}<11$\bar{2}$> direction, suggesting the atom bond in {111}<110> shear model are stronger than that in {111}<11$\bar{2}$> direction. The stronger bond in the shear model in {111}<110> direction results to higher Young's modulus than that of the shear model in {111}<11$\bar{2}$> direction.

Table 7: Calculated average Bader charge difference between O, Zr and La ions.

	Young's modulus (DFT stress-strain analysis)	Average Bader Charge difference between O and Zr	Average Bader Charge difference between O and La
Tensile in [001]	188.139	4.592	3.469
Tensile in [110]	189.556	4.804	3.603
Tensile in [111]	208.462	5.106	3.696
Shear in {111}<110>	76.037	4.965	3.568
Shear in {111}<11$\bar{2}$>	73.381	4.893	3.535

The contours of charge density distribution in each LZ tensile simulation with the strain of 0.5 are plotted in Fig.34. Charge density distribution reveals the election gain and loss characteristic. The red color indicates election gain and the blue color indicates the election loss. As shown in Fig.34, the Zr atoms lost almost all its valence election to the O atoms. The Density distributions near O atoms are similar between the [001] tensile model and [110] tensile model. However, the [111] tensile model has the highest charge density near O atom among all the tensile models, suggesting the electron interaction in [111] tensile model are the strongest. This strong election interaction leads to a high Young's modulus in [111] direction.

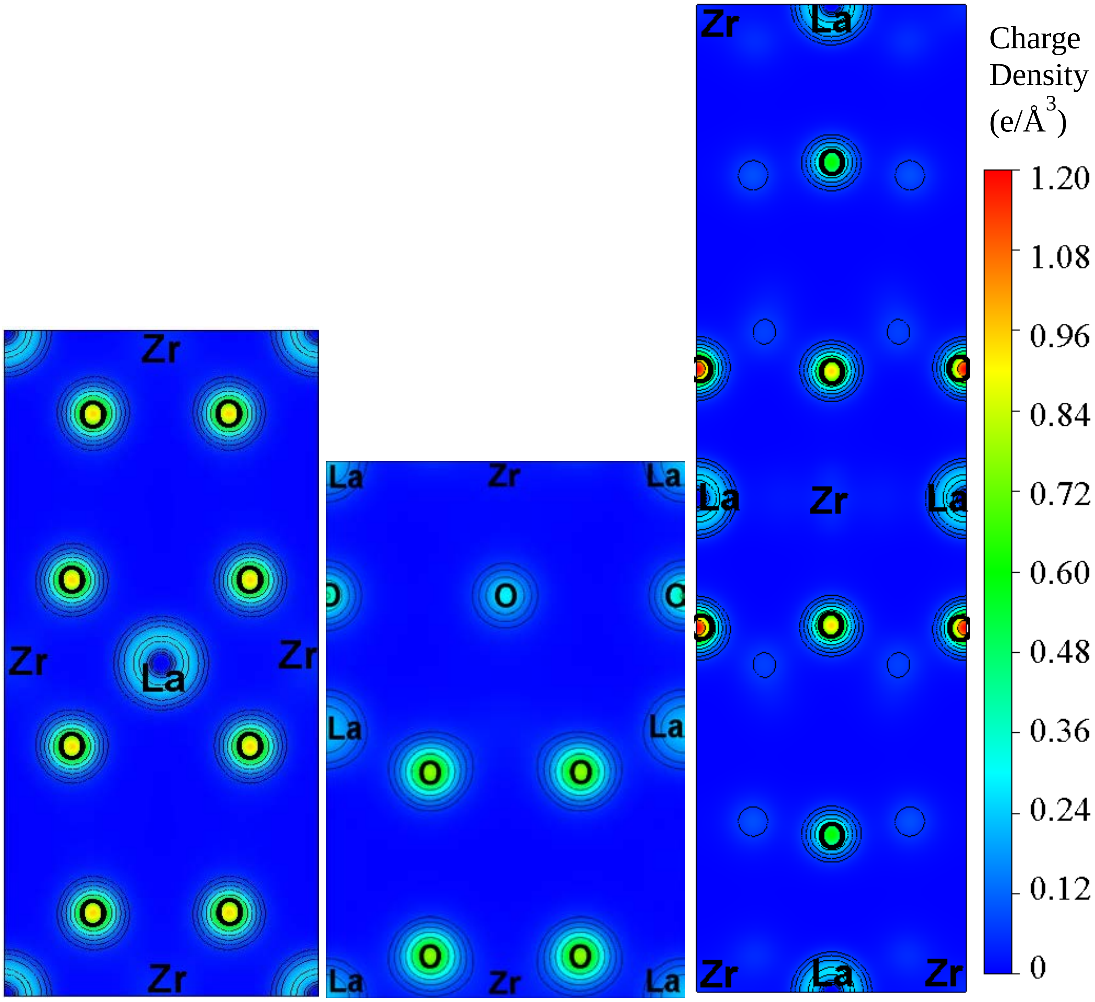

(a) (b) (c)

Figure 34: Charge density distribution (e/Å^3) of tensile calcualtion at strain of 0.5 in (a) [001] direction, (b) [110] direction and (c) [111] direction.

4.2.6 MD LZ models

All of the DFT calculations for tensile and shear deformations are performed on the ground state of atoms, which is typically at the temperature of 0 K. The tensile and shear simulations at higher temperatures were conducted using molecular dynamics (MD) calculation. MD also can be performed at a larger scale than the first principles calculations. All of the MD calculations in this study were conducted using LAMMPS (Large-scale Atomic/Molecular Massively Parallel Simulator) MD simulation package [61]. In this work, the interaction between atoms was assumed to be purely ionic, so the Buckingham and Coulomb potential were applied to describe the short and long range atom interactions, respectively, which can be expressed as follows:

$$U_{ij}(r_{ij}) = A_{ij} \exp\left(\frac{-r_{ij}}{\rho_{ij}}\right) - \frac{C_{ij}}{r_{ij}^{6}} + \frac{1}{4\pi\epsilon_0} \cdot \frac{q_i q_j e^2}{r_{ij}} \tag{21}$$

where r_{ij} is the distance of the interactive ions, q_i and q_j are the charges of La^{3+}, Zr^{4+}, O^{2-} ions, ρ is an ionic pair dependent length parameter, and A and C are adjustable parameters. The parameters of the Buckingham potential used in this study are listed in Table 8, which were fitted based on experimental crystallographic data and Hartree-Fock calculated elastic constants by Crocombette *et al.* [62].

Both tensile and shear simulations were conducted in 300 K. The tensile simulation was carried out using uniaxial elongation along the x-axis, and the shear simulation was performed using uniaxial compression. Periodical boundary condition was used in all these MD simulations. The first principles calculation LZ unit cell shown in Fig.27 was used to assemble the MD tensile and shear models. For tensile MD calculation, three tetragonal boxes of 12×12×24 (individually in x, y, z directions) LZ unit cells in [001], [110] and [111] directions were assembled as tensile models in each direction.

The MD model of tensile simulation in [001] direction is shown in Fig.35. In the tensile model, the (001), (110) and (111) surface were perpendicular to the tensile axis (z). The shear models were built with 16×16×16 LZ unit cells in [112] direction and 24×36×16 LZ unit cell in [110] direction. The compression axis was performed along [110] and $[11\bar{2}]$

directions. The conjugate gradient method was used to minimize the energy of the system in both tensile and shear simulations [63]. Then, the time integration was performed in isothermal-isobaric (NPT) ensembles, which was dedicated to generating the position and velocities parameters. Finally, the tensile models were elongated in the NPT ensembles, and the shear models were compressed in the canonical (NVT) ensembles. The time step of all the MD simulations performed at 1 femtosecond.

Table 8: Buckingham potential parameter for LZ MD models [62].

Interactions	A (eV)	P (Å)	C (eV· Å^6)	Charges
O-O	22764.00	0.1490	27.89	-2.0
La-O	1367.41	0.3591	0.00	-3.0
Zr-O	1478.69	0.3554	0.00	+4.0

4.2.7 MD simulations of LZ tensile and shear deformations

Fig.35 shows the models of the first and last steps of the MD tensile calculations in [001] direction. The model image of initial step demonstrates the perfect LZ single crystal without any tensile strain. The model image of 0.16 strain step shows that there are some vastly deformed areas in the model, which reach its critical strength and are about to break apart.

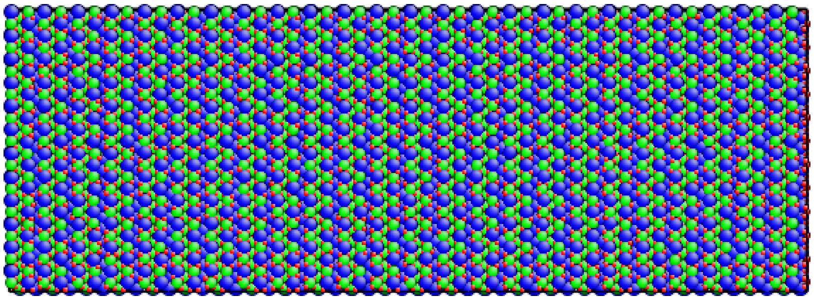

(a)

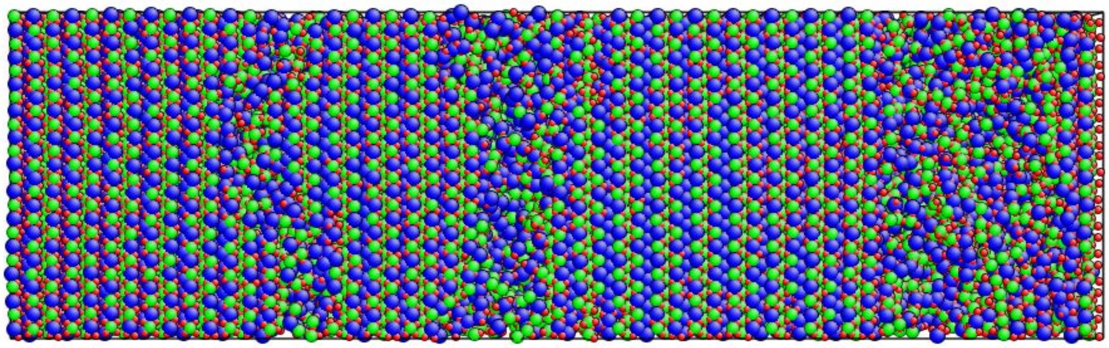

(b)

Figure 35: MD calculated tensile model in [001] direction. (a) the initial step (no strain), and (b) the step with 0.16 strain. Each ball shown as green, red, and blue indicates Zr atom, O atom and La atom, respectively.

Fig.36 shows the MD method calculated tensile stress and strain curves in [111], [001], [011] directions. All of the stress-strain curves in these three tensile simulations exhibit an elastic stage and the stress drops after the maximum tensile stress reached. The slopes of these stress-strain curves in the elastic stage are very similar when the strain is less than 0.03 at the beginning. Then, the slope changes as the increase of the stress, when the deformation occurs in the tensile model. The Young's modulus of LZ in [111], [001], [011] directions are calculated from the slope of the elastic stage on the MD calculated stress-strain curves, whose strains ranges from 0 to 0.03. The Young's modulus values in [001] and [111] directions are very close to each other, which are higher than that in [110] direction. The stress-strain curve in [001] direction shows longer linear elastic stage and higher ultimate stress than the stress-strain curves in other two directions, indicating that LZ has a larger toughness in [001] direction than that in [110] and [001] directions. The MD calculated ultimate tensile strengths share the same trend with the DFT results. However, the magnitude of Young's modulus, ultimate strength and toughness results are different with DFT results.. This is primarily due to the different scale in dimension and atom number between DFT and MD calculations. The MD models used in this works are about several hundred times larger than the DFT model in both atom number and dimensions.

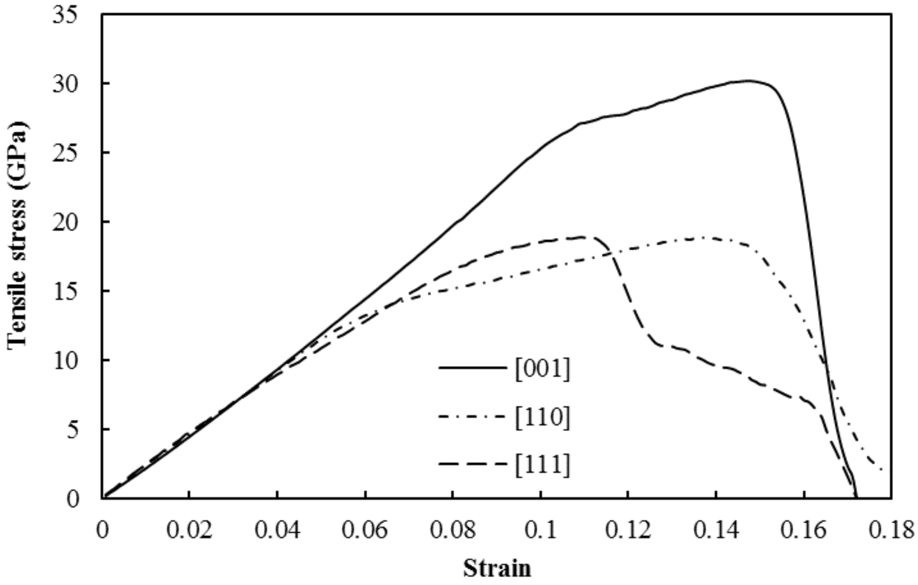

Figure 36: MD calculated tensile stress-strain curves.

The shearing stress was derived from the virial theory by averaging the virial stress over the whole system, which includes both the potential and kinetic energies [68]. The shear stress was calculated by the following equation:

$$\tau = -0.5[\sigma_{xx} - 0.5(\sigma_{yy} + \sigma_{zz})] \tag{22}$$

where x is the uniaxial compression axis [69]. The relation between the resolved compression and shear slip system was also considered. The orientation of the slip plane in the LZ normal compression model is very close to the initial compression axis, so the compressive shear strain was used to specify the strain in the slip plane as a simplification [69].

Fig.37 shows the MD calculated shear stress-strain curves in [110] and [112] directions. The shear stress-strain curves have the similar form as the tensile stress-strain curve, which shows a linear elastic stage. The ultimate shear strength of [110] is obviously larger than that of [112]. Similar to the DFT calculated shear stress-strain curves, the MD shear results also indicate that LZ single crystal in [112] direction are more likely to slip than in [110] direction.

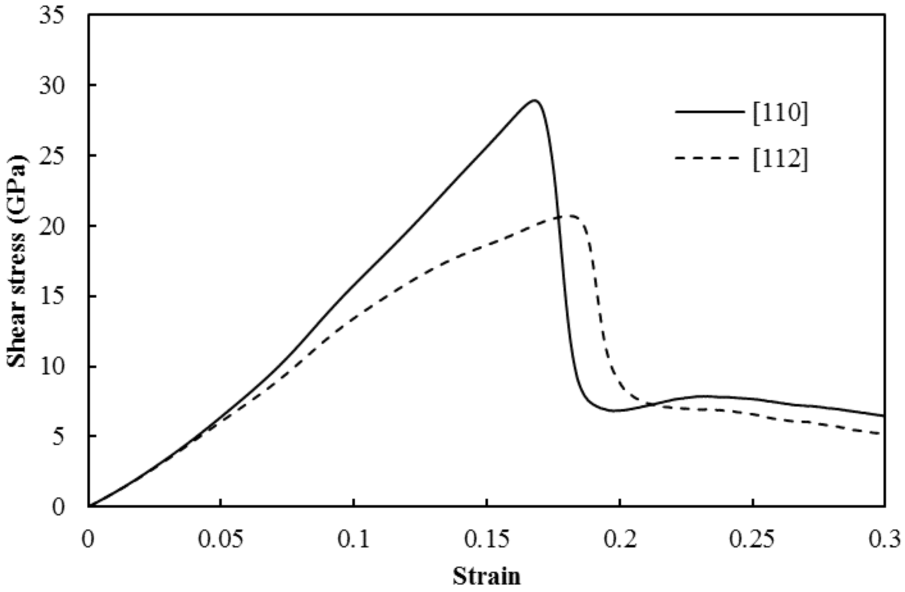

Figure 37: MD calculated shear stress-stain curves of LZ in [110] and [112] directions.

4.2.8 Summary of DFT and MD modeling of mechanical properties

In this task, the conventional unit cell of single crystal LZ was built, and the lattice constant of LZ unit cell was optimized using DFT calculations. Based on the LZ unit cell model, the nanoscale tensile and shear simulation for LZ single crystal material were performed using DFT and MD calculations, and the corresponding mechanical properties were calculated using two approaches: stress-strain curve analysis in large deformation and Voigt-Reuss-Hill approximation in small deformation. The DFT calculated results of both methods are very close, suggesting the consistency of these two methods. Comparing with experimental results from the literature, the effective elastic moduli calculated from Voigt-Reuss-Hill approximation have a good accuracy. The main conclusions of this task can be summarized as following aspects.

(1) The actual lattice constant of LZ was calculated by minimization of the total energy. The DFT calculated LZ lattice constant is 10.875 Å, which has an error of 0.68 % comparing to the experimental result.

(2) The elastic moduli of LZ single crystal are anisotropic. The DFT results show that the largest Young’s modulus occurred in [111] direction. The average Bader charge difference analysis indicates that the bonds between Zr and O, and between La and O are the strongest in LZ tensile model in [111] direction. The charge density distribution analysis exhibits the strong electron interaction in tensile [111] model, which leads to a high Young’s modulus.

(3) The DFT calculated shear stress-strain in {111}<110> and {111}<11$\bar{2}$> slip system are very similar, so as the average Bader charge difference between the cations and anions in these two models. The most likely slip system in {111} plane is {111}<11$\bar{2}$>, because more strain is generated in {111}<11$\bar{2}$> shear model than that in {111}<110> shear model under same stress level.

(4) The MD calculated tensile and shear stress-strain curves show the same trend as the DFT calculated results. However, the value of the mechanical properties calculated using MD is quite different from the DFT results, because the scale of dimensions and number of atoms are different between the MD and the DFT models.

Task 4.3: DFT, MD, and FE modeling of thermal properties of LZ

4.3.1 Introduction

TBCs are used in high-temperature environments, so the thermal properties are very important for TBC material. The primary requirements of TBCs for the turbine designer are low thermal conductivity [70, 71]. Although there are several experimental methods to measure thermal conductivity, such as flash method and pulsed thermal imaging-multilayer analysis (PTI-MLA) method, there is no theoretical modeling calculation on LZ thermal conductivity. Actually, the intrinsic thermal conductivity of single crystal LZ is almost impossible to be accurately measured using experimental method due to the porous and fragile characteristic of the LZ powder, which includes the huge number of defects. In addition, the experimental equipment has limitations on the temperature range and the sample size. However, the theoretical calculation does not have the temperature limitation.

In this task, the specific heat of single LZ crystal was calculated based on the optimized LZ unit cell using DFT calculations. Then, we propose a novel image-based multi-scale simulation framework combining MD and FE method calculations to study the thermal conductivity of LZ thermal barrier coating. A reverse non-equilibrium molecular dynamics approach is used at first step to compute the temperature-dependent thermal conductivity of LZ single crystal. Then, the single crystal data is plugged into an FE model of a thermal barrier coating that generated using SEM microstructures images. The predicted thermal conductivities from the FE model are compared against thermal conductivity experimental results using both flash laser and PTI-MLA techniques.

4.3.2 Thermodynamics and specific heat of LZ

The thermodynamic energies (Gibbs free energy, enthalpy and entropy) and specific heat calculation of LZ unit cell were implemented by CASTEP code [72]. The thermodynamic energy and specific heat can be well described using a quasi-harmonic Debye model, in which the non-equilibrium Gibbs function $G^{*}(V, P, T)$ can be expressed as the following equation [73].

$$\mathrm{G}^{*}(V(x), P, T) = E(x) + PV(x) + A_{vib}[V(x), T] \tag{23}$$

where x represents all the geometric information such as lattice constant, E(x) is the total energy of LZ unit cell, PV(x) represents the energy in constant hydrostatic pressure condition, and A_{vib} is the vibrational Helmholtz free energy. E(V) and PV can be obtained from DFT calculation result, so the next step is to calculate the vibrational contribution A_{vib} using Debye model of the phonon density of states:

$$\mathrm{A}_{vib}(\Theta, T) = nkT[\frac{9}{8}\frac{\Theta}{T} + 3\ln\left(1 - e^{-\Theta/T}\right) - D\left(\frac{\Theta}{T}\right)] \tag{24}$$

where $\Theta(V)$ is Debye temperature, n represents the number of atoms per formula unit, and D(y) is the Debye integral that defined as:

$$D(y) = \frac{3}{y^{3}}\int_{0}^{y}\frac{x^{3}}{e^{x}-1}dx \tag{25}$$

In Debye ‘s theory, the vibrations of the solid are considered as elastic waves, so the Debye temperature of the solid is related to average sound velocity. In addition, Debye temperature in a solid material is determined by phonon perturbation and lattice vibration, which can be computed as:

$$\Theta = \frac{h}{k}\left(6\pi^2 V^{1/2} n\right)^{1/3} f(\nu)\sqrt{\frac{B}{M}} \tag{26}$$

where M represents the molecular mass, B is the adiabatic bulk modulus, ν is Poisson ratio, and f(ν) is given by the following equation:

$$f(\upsilon) = \{3\left[2\left(\frac{2}{3}\frac{1+\upsilon}{1-2\upsilon}\right)^{2/3} + \left(\frac{1}{3}\frac{1+\upsilon}{1-\upsilon}\right)^{2/3}\right]^{-1}\}^{1/3} \tag{27}$$

The Phonon calculations in CASTEP were used to evaluate the enthalpy, entropy, free energy, and specific heat capacity of LZ unit cell as a function of temperature in the quasi-harmonic Debye approximation. The specific heat (C_v) can be expressed using the following equation [73].

$$C_v = 3nk[4D(\Theta/T) - \frac{3(\Theta/T)}{e^{\Theta/T}-1}] \tag{28}$$

The calculated thermodynamic energy curves are shown in Fig.38, in the temperature range of 0-1800 K. The entropy increases as temperature increases, which is consistent with the second law of thermodynamics. Then enthalpy increases slowly and the free energy decreases as the temperature increases. The enthalpy indicates the amount of heat transfer into the crystal cell. Since the Gibbs free energy equals to the enthalpy minus the product of temperature and entropy, it is reasonable that the free energy decreases as temperature increases.

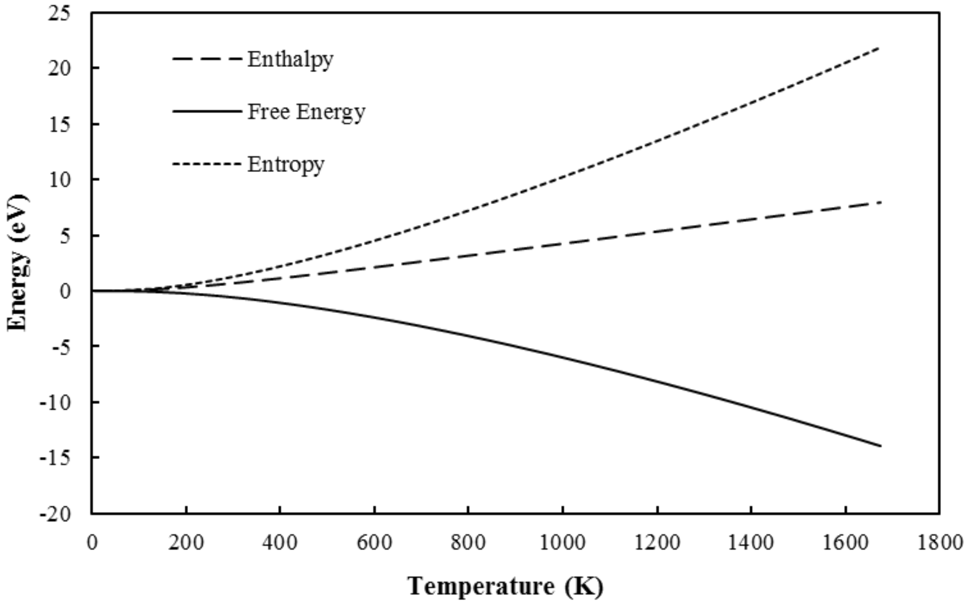

Figure 38: Thermodynamic energy curves of LZ as function of temperature

The calculated specific heat (C_v) curve in constant pressure shows in Fig.39, in the temperature range of -273 to 1327 ^oC, which is very difficult to measure by experiment in such wide temperature range. The value of specific heat increases as the temperature increases, especially in low-temperature range it increases very rapidly. When the temperature reaches above 400 ^oC, the specific heat increased very slowly, the value is 0.4~0.467 J/ (g·^oC) from 400 ^oC to 1400 ^oC.

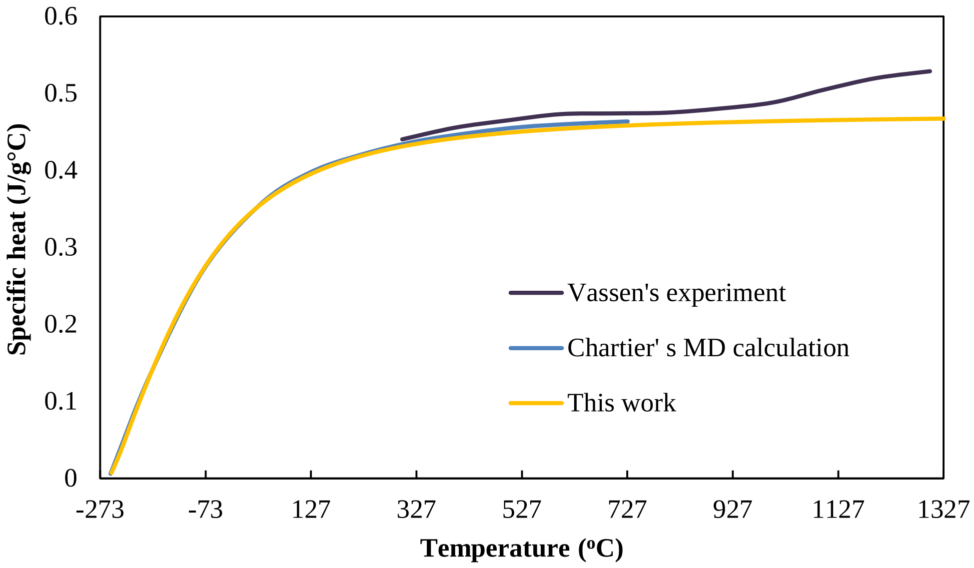

Figure 39: Specific heat results and comparison to literatures.

By comparison with experiment data from Vassen‘s work [12, 18] and calculated results from Chartier’ s work [74], it can be concluded that the specific heat calculated by this work is accurate and reliable.

4.3.3 Thermal conductivity of LZ crystal and coating

4.3.3.1 Thermal conductivity of single crystal LZ using MD simulation

The MD method can be used to investigate the thermal conductivity. For single crystals, there are two common molecular dynamics methods for thermal conductivity calculations: direct method [75, 76] and Green-Kubo method [77, 78]. The direct method is a non-equilibrium molecular dynamics (NEMD) method which imposes a temperature gradient to the system. The Green-Kubo method is an equilibrium MD (EMD) method which uses the current fluctuation to calculate the thermal conductivity according to the fluctuation-dissipation theorem [79]. Based on the NEMD, a more reliable method to compute thermal conductivity was developed, which is the reverse NEMD (RNEMD) method [80]. In RNEMD method, the Muller-Plathe algorithm [81] is applied to exchange kinetic energy between two atoms in different regions of the simulation box at every finite step to induce a temperature gradient in the system. It works by exchanging velocities between two atoms in different parts of the simulation cell. At set intervals, the velocity of the fastest atom in one region is replaced by the velocity of the slowest atom in another region and vice versa. Consequently, the first region becomes colder, whereas, the second region increases in temperature. The system will be reacted by flowing energy from the hot to cold regions. Eventually, a steady state is established when the exchanged energy equilibrates the energy flowing back in a temperature gradient over the space between the two regions. This enables the thermal conductivity of a material to be calculated. The usual NEMD approach is to impose a temperature gradient on the system and measure the response as the resulting heat flux. In RNEMD using the Muller-Plathe algorithm, the heat flux is imposed, and the temperature gradient is the system's response. The advantage of RNEMD over traditional NEMD is that there are no artificial ‘‘temperature walls’’ in the simulated system because these cause a fluid structure different from the bulk. Additionally, energy and momentum are conserved, and there are no thermostat issues [80].

The reverse non-equilibrium molecular dynamics (RNEMD) method is used to predict temperature-dependent thermal conductivities of the single crystal LZ model in this work. The thermal conductivity model is assembled using the geometry optimized LZ unit cell, which contained 2×2×30 unit LZ cell and had the dimension of 21.6×21.6×324 $Å^3$ in x,y,z directions [82]. The thermal conductivity model (LZ supercell model) contains total 10560 atoms, including 6720 O atoms, 1920 La atoms, and 1920 Zr atoms. The supercell model is sliced into 30 layers with equal thickness. A temperature decay constant 0.1 per picoseconds is imposed in each layer. The thermal conductivity calculations are performed as the energy flux divided by the temperature gradient [80]:

$$k = \frac{\dot{q}}{\partial T / \partial z} \tag{29}$$

where k is thermal conductivity, $\dot{q}$ is heat flux defined by the amount of heat (Q) transferred per unit time per unit area in heat transfer direction; $\partial T/\partial z$ is the temperature gradient in the heat transfer direction. The universal force field was used in this work, which has a full coverage of the periodic table [83].

One of the calculated temperature distribution contour in the LZ supercell model is shown in Fig.40. There are two high-temperature hot zones at the ends due to the periodic boundary condition, and a low-temperature cold zone in the middle for generating a temperature gradient. The target temperature in Fig.40 is 1273 K, which is the average temperature in the supercell [84].

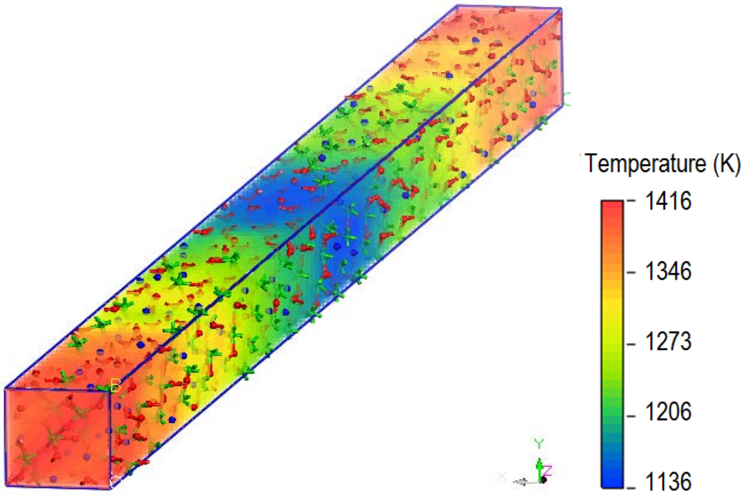

Figure 40: Temperature distribution in LZ single crystal supercell at 1273 K.

The temperature gradient along the heat flux direction in the supercell is plotted in Fig. 41. Two linear temperature gradients were identified and the thermal conductivity was calculated using Equation 29.

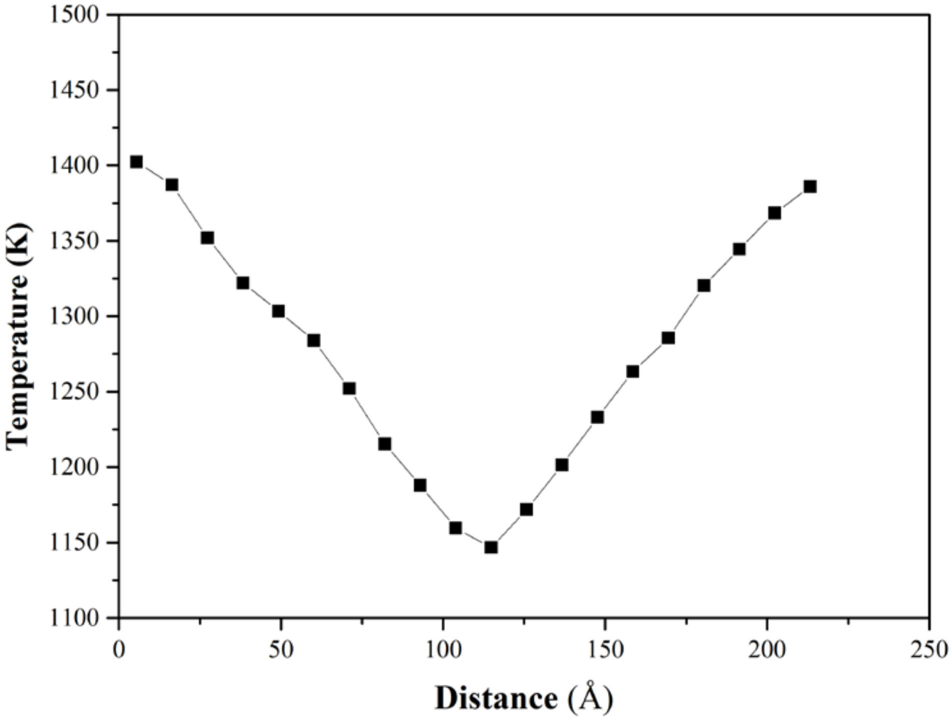

Figure 41: Temperature distribution along the heat flux direction.

The calculated temperature-dependent thermal conductivity of LZ single crystal is shown in Fig.42. The thermal conductivity values range from 1.25 W/m/K to 1.39 W/m/K in the temperature range of 473 ~ 1273K. It is noted that thermal radiation effect at high temperatures is not considered in this RNEMD model. Our predicted LZ single crystal thermal conductivity is lower than Schelling's NEMD result (1.98 W/m/K at 1200 ºC [75]), probably due to two factors. One is the method, Schelling used NEMD and we use RNEMD. The second is the different force fields used in the model. Schelling used Buckingham potentials and this work applied the universal force field. Schelling's single crystal result compared reasonably well with fully dense polycrystalline experimental data. However, the influence of microstructure in the polycrystalline was not considered in Schelling's work. In our model, we also calculate temperature-dependent thermal conductivity of polycrystalline LZ using the FE model as discussed below.

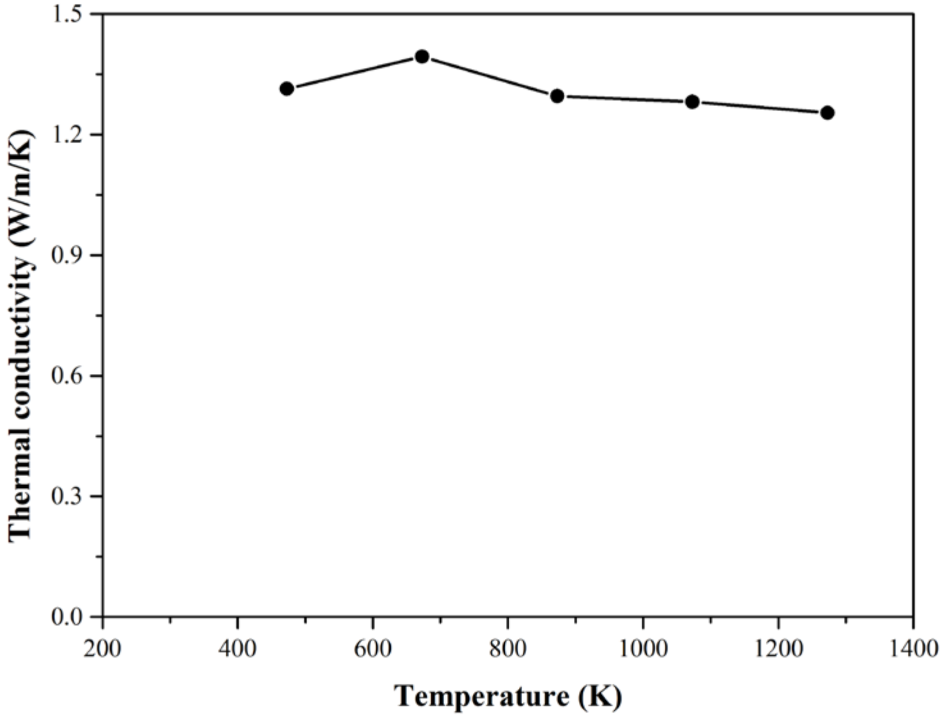

Figure 42: Temperature-dependent thermal conductivity of LZ single crystal using the RNEMD method.

4.3.3.2 Finite element modeling of thermal conductivity of polycrystalline LZ coating

Finite element (FE) method can be used to simulate the heat conduction process of a coating structures with cracks and pores [85]. The pore and crack morphology of thermal barrier coating is an important parameter affecting the mechanical and thermal properties [86, 87]. The quantitative imaging analysis method can be used to investigate the non-uniformity properties of the porous coating with polycrystalline microstructure [8, 88]. Based on the quantitative imaging analysis, the image-based FE method uses scanning electron microscope (SEM) images to generate microstructures and import into an FE model [89]. Therefore, the image-based FE method is able to calculate the thermal conductivity of non-uniform porous polycrystalline coatings.

Three representative SEM images of the cross-sectional view of the porous LZ TBC sample with the porosity of 13.61% are converted into binary images using imaging processing software package ImageJ [90]. In the binary images, white color regions represent solid LZ coating phase, and black color regions are pores and cracks. The binary images then are passed into to an FE software package, COMSOL Multiphysics [91], to automatically generate FE meshes. In the FE models, a constant temperature difference boundary condition is applied at the top (T_{top}) and bottom (T_{bot}) surface of the system, with the average temperature ($T_{top}/2+T_{bot}/2$) as the target temperatures, 473 ~ 1273K. The pores and cracks are filled with non-flowing air. Zero thermal conductivity is assumed for the pores and cracks because the thermal conductivity of non-flowing air is much smaller than that of the coating [92, 93]. For LZ coating solid phase, the calculated temperature-dependent thermal conductivities of LZ single crystal from RNEMD are used.

For porous LZ polycrystalline coating samples, SEM images of cross-sectional views of three free-standing coating samples were used. A representative SEM image of LZ coating is shown in Figure a. The simulated temperature contour in the sample is shown in Fig.43.

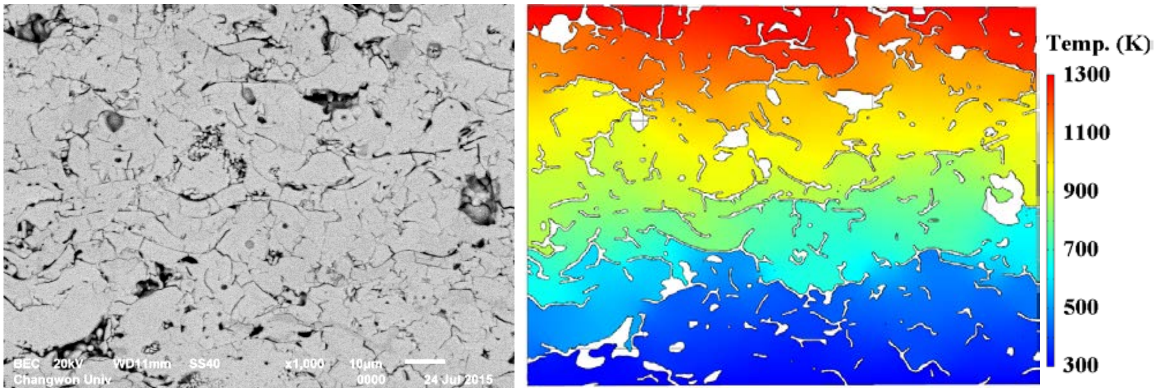

(a) (b)

Figure 43: (a) SEM image, and (b) calculated temperature contours of LZ coatings.

As shown in Fig.44, comparing with the flash method experiment results, the FE method calculated thermal conductivity values are in the good agreement with the experiments results. The cracks and pores in the coating clearly reduce the thermal conductivity of the coatings.

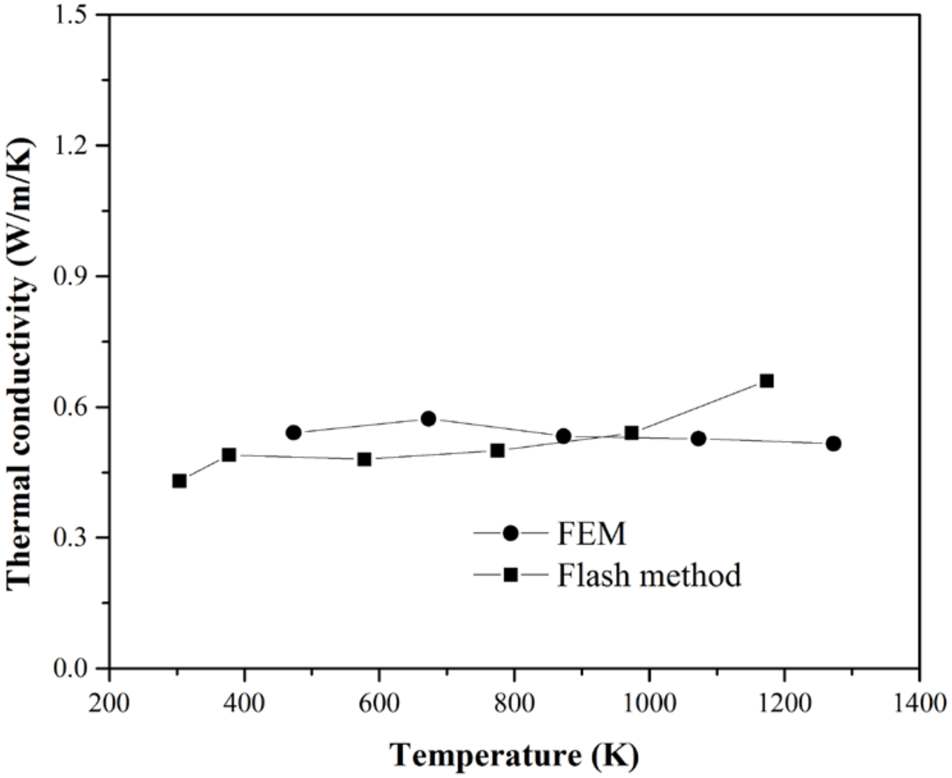

Figure 44: Thermal conductivity of LZ coating: FE method prediction and flash method.

Using the flash method, the averaged thermal conductivity measured from the three LZ porous coating samples is given in Fig.45, which ranges from 0.44 to 0.62 W/m/K in the temperature range of 300~1200 K. The measured thermal conductivity is relatively constant below 900 K, and slightly increases above 900 K. As shown in Fig.44, the predicted thermal conductivity using the FE model is in a good agreement with experimental measurement.

Pulsed thermal imaging-multilayer analysis (PTI-MLA) method is recently developed as a new method to measure the thermal conductivity [94], to overcome the limitations of the flash method. For example, the flash method requires two sides accessible for the specimens. The sample surface is destructed by the laser flash. In addition, the flash method obtains a single averaged thermal conductivity of the sample, and it does not provide the spatial distribution of the thermal conductivity [94]. In comparison, the PTI-MLA technique developed at ANL is a one-sided experimental system, which consists a photographic flash lamp (Source 6400; BALCAR, France), an infrared filter and a mid-wavelength (3~5μm) infrared camera (Phoenix, FLIR). PTI-MLA method is based on monitoring the surface temperature decay, after it is applied with a pulsed thermal energy that is transferred inside the sample gradually [94].

In the pulsed thermal image-multilayer analysis method, the optical image of LZ coating specimen, thermal conductivity map, and heat capacity map are shown in Fig.45. The measured product of heat capacity is ~ 2.16 J/cm^3/K. The average thermal conductivity measured by the PTI-MLA technique is 0.55 W/m/K, which is also consistent with the results measured by the flash method and calculated by FE model.

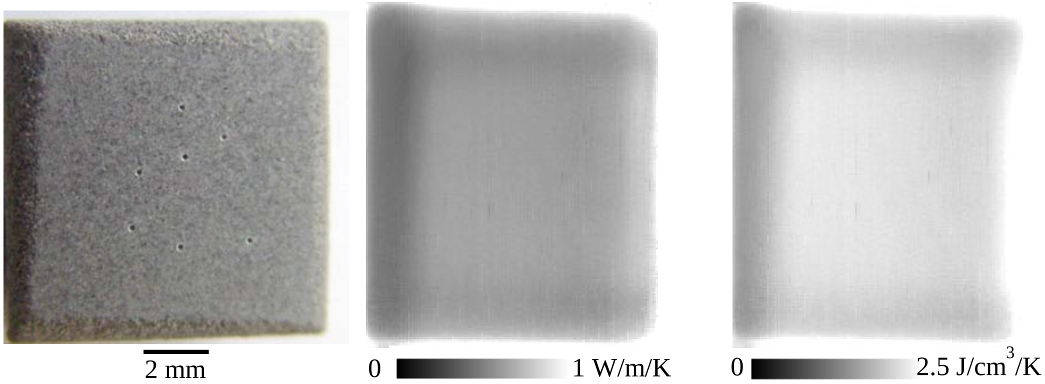

(a) (b) (c)

Figure 45: LZ coating (a) optical image; (b) thermal conductivity map; (c) product of heat capacity (ρc) map

4.3.4 Summary of DFT, MD, and FE modeling of LZ thermal conductivities

In this task, selected thermodynamic energies (Gibbs free energy, enthalpy and entropy) and the specific heat of single crystal LZ were calculated using DFT calculations based on a quasi-harmonic Debye model. In addition, a novel image-based multi-scale simulation framework combining molecular dynamics and finite element calculations has been proposed to study the thermal conductivity of porous LZ coatings. Experimental validations include the flash method and pulsed thermal image-multilayer analysis technique to measure the coating thermal conductivity. The main conclusions of this task are summarized as following aspects.

(1) The calculated specific heat capacity of single crystal LZ ranges from 0.4~0.467 J/g/K at a temperature range from 400 ^oC to 1400 ^oC. The calculated results have a good accuracy comparing with literature data.

(2) The calculated thermal conductivity of LZ single crystal ranges from 1.25 W/m/K to 1.39 W/m/K in the temperature range of 473 ~ 1273K, using RNEMD method.

(3) Using the image-based FE method and single crystal thermal conductivity data, the calculated thermal conductivities of porous LZ polycrystalline are in the range of 0.46 ~ 0.59 W/m/K at the temperature range of 473 ~ 1273K. The predicted FE data are in good agreement with the flash method, 0.44 to 0.62 W/m/K, in the temperature range of 300~1200 K, and the PTI-MLA technique, 0.55 W/m/K. The image-based multi-scale simulation framework proposed in this work provides a design tool to the future design of advanced coating systems.

Task 4.4 Modeling of mechanical properties of ZrO2/Ni interface

4.4.1 Introduction

It is widely accepted that the mechanical properties at the ceramic-metal interface between the top and bond coats and/or between the top coat and the TGO layer have a primary influence on the lifetime of the TBCs in the thermomechanical environments. It is still challenging to directly examine the interfacial mechanical properties from experiments. Modeling and simulation are powerful tools as an alternative way to investigate the interfacial properties and decipher failure mechanisms [95]. The failure and spallation mechanisms of the have been discussed by Evans in the context of continuum mechanics [39, 96, 97]. He suggested that the delamination, typically observed in TGO layer or near the interface, is related to a significant residual stress gradient which amplifies the imperfections in TBCs. Cracks propagate when the residual tensile and/or shear stresses exceed the delamination toughness of the top bond coat interface. At the atomic level, the mechanical characteristics at the ceramic-metal interface are related to the intrinsic atomic properties. The idealized mechanical properties can be calculated which offers insights into the complex interface systems. Guo *et al.* investigated the mechanical properties of Ni (111) /α-Al2O3 (0001) interface, and calculated the theoretical shear strength and unstable stacking energy, using the first principles calculations [98]. Since LZ, 8YSZ and NiCrAlY bond coat structure is too complicated to calculate using DFT method, the ZrO_2/Ni interface structure was implemented as a simplified top and bond coat model. This simplification is reasonable because the main composition of 8YSZ and LZ is ZrO_2, and Ni is the main composition of bond coat. Christensen *et al.* studied the adhesion energy of ZrO_2(111)/Ni(111) interface using the ultrasoft pseudopotential within the density functional theory [99].

Although previous efforts, however, the exact mechanical properties of ZrO_2/Ni interface are still not well examined using theoretical calculation approach. Specifically, the interfacial mechanical behaviors under tensile and shear stresses are not available. The difficulty of such studies primarily stems from the complexity of the interface structure, which requires minimizing the misfit between different crystal surfaces, and intensive calculations involved in the interfacial tensile and shear deformation simulations.

In this task, we conducted the DFT and MD tensile and shear calculations of ZrO_2 (111)/Ni (111) interface. In the DFT modeling, an interface model in Ref. [99] is used to compare and/or partially validate the model through calculating the adiabatic work of adhesion. For mechanical property calculations, two Ni thickness of 1 and 3 atomic layers are modeled to investigate the effect of interface thickness on the mechanical properties. The crystallographic orientation (111) is considered since the primary slip system in face-centered cubic (fcc) metal crystals, such as Ni, is {111}<110>, with $\{111\}<11\bar{2}>$ being the secondary slip system [58]. Although the actual slip systems of the ZrO_2/Ni interface may be more complicated, both {111}<110> and $\{111\}<11\bar{2}>$ should be the major slip systems. Therefore, the tensile stress-strain curve in <111> direction is calculated, and the shear stress-strain curves along {111}<110> and $\{111\}<11\bar{2}>$ directions are computed.

The toughness and elastic modulus, Young's modulus or shear modulus, are also calculated. Finally, the Bader charge analyses are conducted to explain the observed interfacial mechanical properties. In the MD model, the electron charge was considered in the force field potential. The tensile simulation in [111] direction and the shear simulation in {111}<110> and {111}<11$\bar{2}$> direction were conducted using MD method.

4.4.2 DFT model description of ZrO_2/Ni interface

4.4.2.1 DFT ZrO_2 (111)/Ni (111) interface model

The constructed ZrO_2 (111)/Ni (111) interface atomistic models are shown in Fig.46 The cubic zirconia (*c*-ZrO_2) has the fluorite crystal structure (space group *Fm3m*) and Ni has a face-centered cubic (fcc) crystal structure (space group *Fm3m*). Both *c*-ZrO_2 and Ni small portions are cut from their bulk counterpart on (111) plane. To match the interface with minimal lattice misfit, the *c*-ZrO_2 and Ni small portions are rotated according to Ref. [99].

As shown in Fig.46, the interface model contains two layers of ZrO_2 (111) atoms, and 1 or 3 layers of Ni (111) atoms [100]. Because the O atoms and Zr atoms are not positioned in the same horizontal plane, the termination of the ZrO_2 (111) surface may result in dipole moment perpendicular to the interface. Therefore, symmetric models are built to screen out the dipole interactions. Two ZrO_2 (111)/Ni (111) interfaces are in this interface model, corresponding to a sandwich structure. This model with the interface is extended periodically in three dimensions, due to the periodical boundary condition. To calculate adiabatic work of adhesion, ZrO_2 (111)/Ni (111) interface slabs are built with a vacuum layer thickness of 10 Å, which is large enough to eliminate the interaction between each interface film layer.

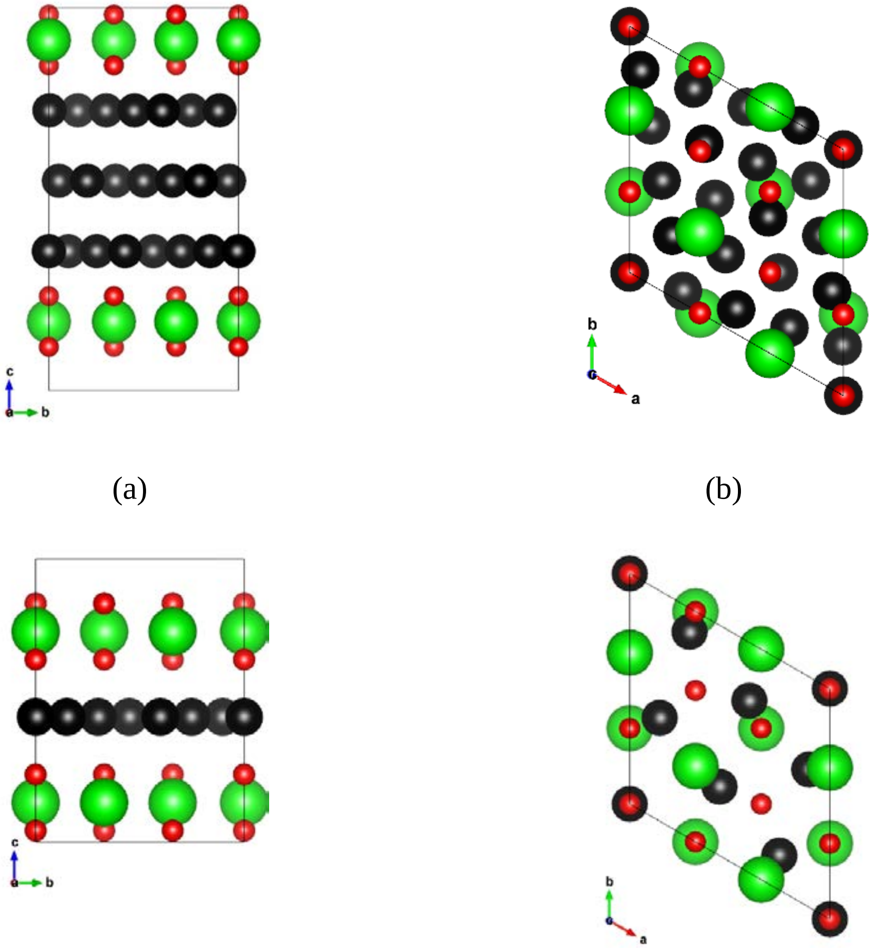

(a) (b)

(c) (d)

Figure 46: ZrO$_2$ (111)/Ni (111) interface models with different Ni atomic layers: (a) side view and (b) top view with 3 layers of Ni, and (c) side view and (d) top view of 1 layer of Ni. Green, red, and black balls are Zr, O, and Ni atom, respectively (same coloring schemes are used in all of the DFT modeling figures afterwards).

The first principles calculations in this task are carried out using the VASP [52, 53, 101], based on the density functional theory (DFT) [49, 50].The projector augmented wave (PAW) method of generalized gradient approximation (GGA) functional is adopted to specify the exchange-correlation potential. A periodic supercell regime is used and *k*-point of the Brillouin zone is conducted using 3×3×1 Monkhost-Pack scheme. A conjugate-gradient algorithm is used to relax the ions into its instantaneous ground state. The plan-wave cutoff energy is 400 eV. The energy relaxation criterion for the electron is 10^{-5} eV for the self-consistency. The total forces are smaller than 0.01 eV/A in the ionic relaxation convergence criterion.

4.4.2.2 Adiabatic work of adhesion

In order to compare or partially validate the interface model, due to limited literature data, adiabatic work of adhesion (W_{adh}) is calculated using the atomistic model described in Ref. [99]. W_{adh} is the most commonly used property to describe the adhesion characteristics, which can be described using the following equation [99]:

$$W_{adh} = \frac{E_{0,Ni} + E^{N}_{0,Zro_2} - E^{N}_{Zro_2,Ni}}{A} \tag{30}$$

where $E_{0,Ni}$ and E_{0,ZrO_2} are the total energies of the relaxed Ni and ZrO_2 surfaces, respectively. $E_{ZrO_2,Ni}$ is the total energy of the relaxed ZrO_2/Ni interface structure. *A* is the area of the interface and *N* is the number of the ceramic layers [99].

4.4.2.3 Stress-strain curves in tensile and shear deformations

For tensile deformation, the calculations are conducted by extending the lattice parameters of the interface model in [111] direction, which is perpendicular to the interface. All ions in the interface model are relaxed, and the volume and the shape of the interface unit cell are also optimized during the stress tensor calculation process. Similarly, for shear deformations, the shear stress is calculated by accumulating the shear strain in {111}<110> or {111}<11$\bar{2}$> direction [102].

4.4.2.4 Bader charge analysis

To explain the calculated stress-strain behaviors, the Bader method is used to calculate the charge transfer numbers and electron density distributions [59, 60, 103]. The charge transfer results are processed by calculating the average charge difference between O and

Ni ions. This is because the bonds formed in the ZrO_2/Ni interface models through the Zr and Ni atoms losing electrons, and the O atoms gaining electrons.

4.4.3 Results and discussion of DFT interface models

4.4.3.1 Adiabatic work of adhesion

The relaxed ZrO_2 /Ni interface models for adiabatic work of adhesion calculations are shown in Fig.47. In this work, all of the atoms except the two bottom Ni layers (which are away from the interface) are relaxed to allow to reach their equilibrium. Comparing with the structures in Ref. [99], the relaxed atomic structures in this study are slightly different. This is due to limited information regarding computation details in Ref. [99].

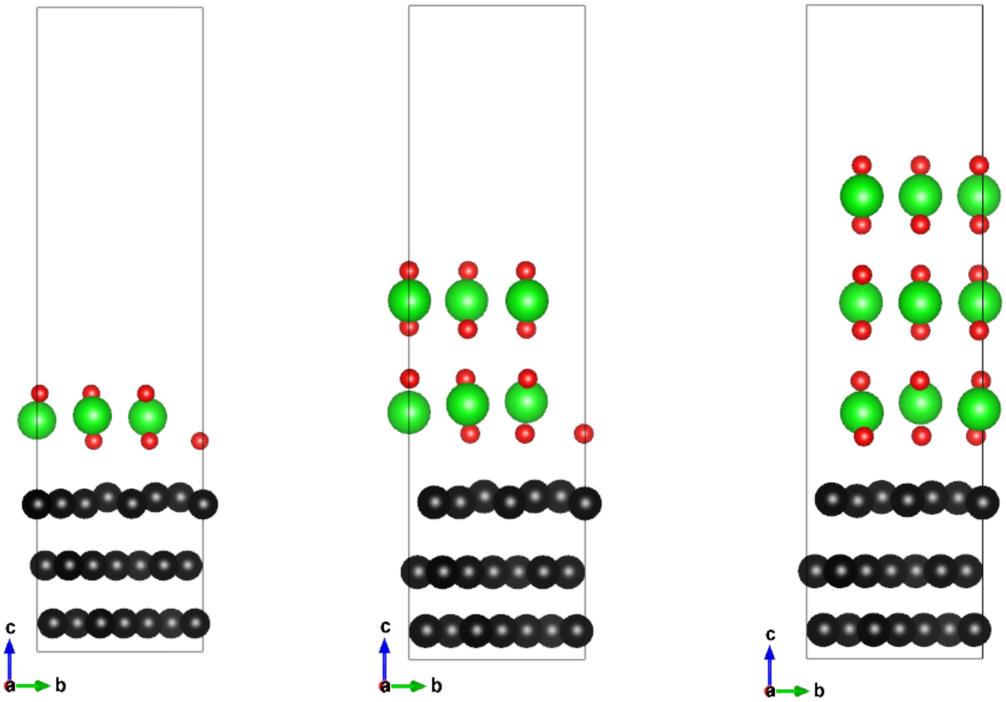

(a) (b) (c)

Figure 47: Relaxed ZrO_2 (111)/Ni (111) interface models with a vacume layer above the slabs: (a) 1-layer ZrO_2, (b) 2-layer ZrO_2, and (c) 3-layer ZrO_2.

In this work, the calculated W_{adh} value of the interface with 1-layer ZrO_2 is 629 mJ/m^2, which is greater than those of 2 and 3-layers ZrO_2 (554 mJ/m^2 and 296 mJ/m^2, respectively). In Ref. [99], the W_{adh} values are 2011, 1308, and 995 mJ/m^2 for 1, 2, and 3-layers ZrO_2, respectively. Although our calculated values are lower than reported in Ref. [99] in ~ 60%, our calculated values follow the same trend as Ref. [99], i.e., a thicker ZrO_2 layer corresponds to a lower adhesion energy.

4.4.3.2 Stress-strain behaviors in tensile and shear deformations

(1) Tensile Deformation along [111] direction

For mechanical property calculations, the atomic configurations of relaxed tensile models along [111] direction with Ni slabs of 1 and 3 layers are shown in Fig.48 and Fig.49, respectively.

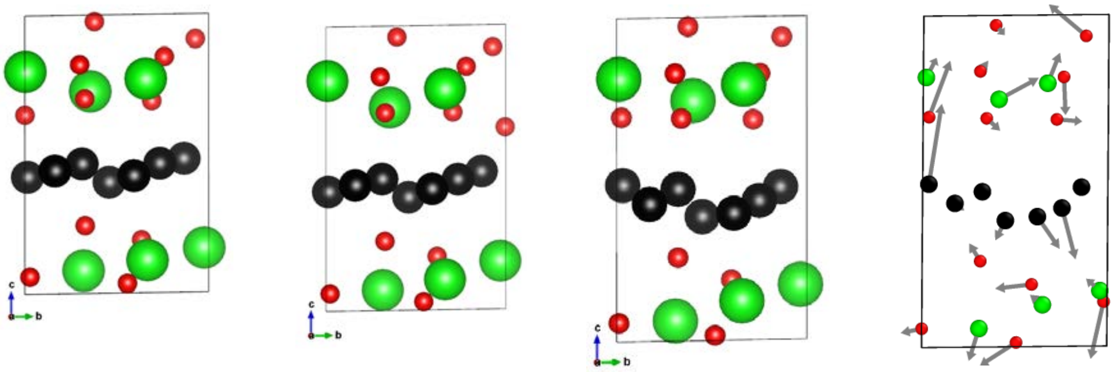

(a) (b) (c) (d)

Figure 48: Tensile deformation models with 1 layer of Ni: (a) initial configuration, (b) strain of 0.051, (c) strain of 0.105 and (d) atom displacement vector between strain 0.105 and initial steps.

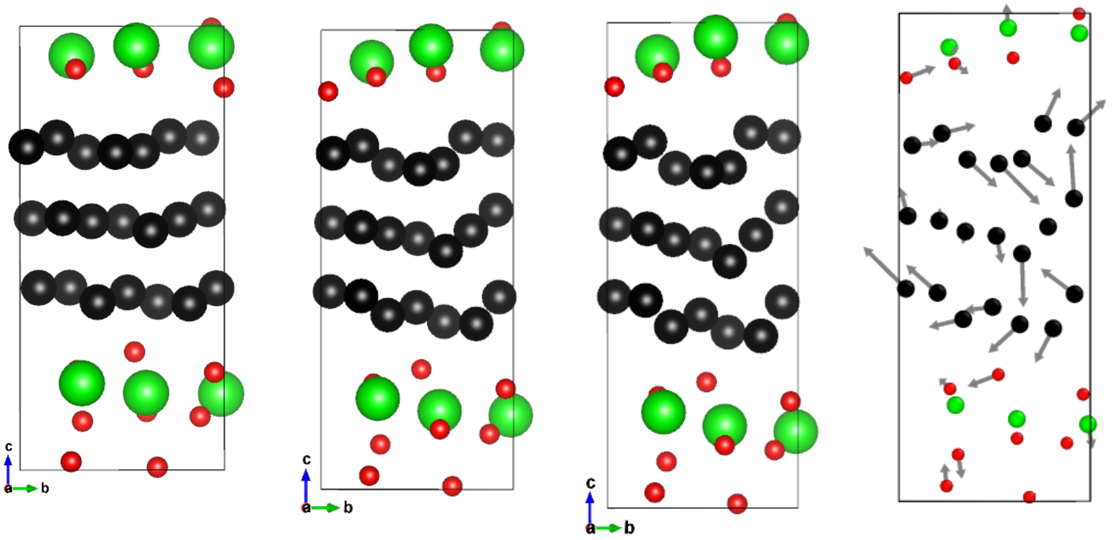

(a) (b) (c) (d)

Figure 49: Tensile deformation models with 3 layers of Ni: (a) initial configuration, (b) strain of 0.072, (c) strain of 0.138 and (d) atom displacement vector between strain 0.138 and initial steps.

The tensile stress-strain curves of ZrO_2 (111)/Ni (111) interface with Ni slabs of 1 and 3 layers are shown in Fig.50. As shown in Fig.50, a thinner (1-layer) Ni layer has almost double Young’s modulus (139.9 GPa) and higher ultimate tensile strength (11.6 GPa) than those of the 3-layer Ni case (60.2 GPa and 7.9 GPa, respectively) (see Table 1 for a complete summary of calculated mechanical properties, including elastic modulus, ultimate tensile/shear strength, and toughness). The layer thickness dependence is consistent with work of adhesion values, i.e., a thin Ni layer interface model has higher strength or work of adhesion. In terms of deformation strain, the 3-layer Ni interface is more ductile as illustrated with larger tensile strain. This can be interpreted by the atom displacement vectors between the final and initial steps of the nanoscale tensile calculation, as shown in Fig.49. The atom displacement of Ni atoms at the interface are larger than that of Zr and O atoms in 3-layer Ni interface model, indicating most of the deformation occurs among Ni layers in the 3-Ni-layers model. In the 1-layer Ni interface model, the displacement of Ni, Zr and O atoms are arbitrarily distributed, but the total outcome of these displacement extends the model in the tensile direction. The 3-layer Ni interface possesses more deformation compatibility than 1-layer Ni interface, suggesting a thick Ni interface can provide extra deformation to accommodate tensile strain.

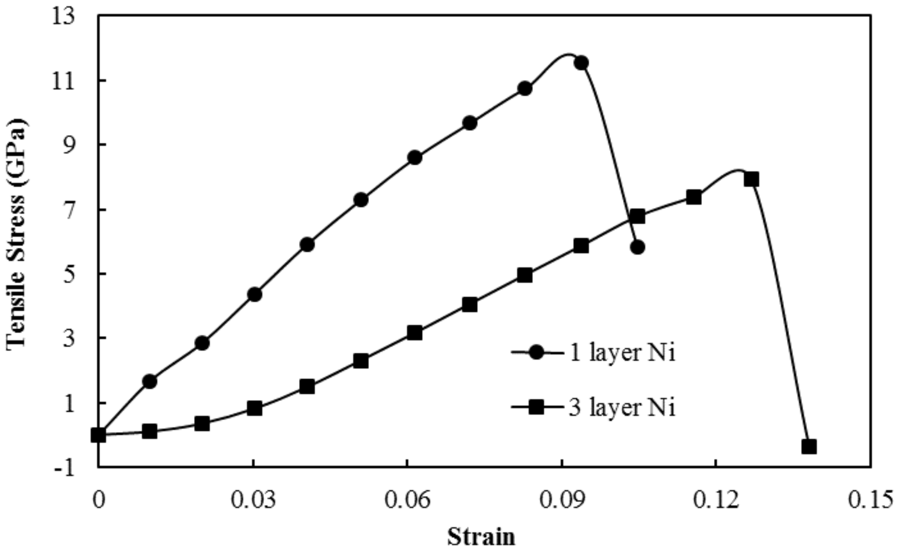

Figure 50: Tensile stress-strain curves of ZrO_2(111)/Ni (111) interfaces with Ni slabs of 1 and 3 layers.

(2) Shear deformations along {111}<110> and {111}<11$\bar{2}$> directions

The atomic configurations of 1-layer Ni slab model during shear deformations along {111}<110> and {111}<11$\bar{2}$> directions are shown in Fig.51, and Fig.52, respectively. The calculated shear stress-strain curves are given in Fig.53. Both the shear modulus (43.9 GPa) and ultimate shear strength (7.9 GPa) along {111}<110> direction are greater than those along {111}<11$\bar{2}$> direction (30.9 GPa for shear modulus and 6.0 GPa for ultimate shear strength). Therefore, {111}<11$\bar{2}$> is a favorable shear slip system in this ZrO2 (111)/Ni (111) interface system, which is different from pure Ni. It is also noted that the ductility of {111}<110> measured by strain, 0.23, is lower than that of {111}<11$\bar{2}$>, 0.27.

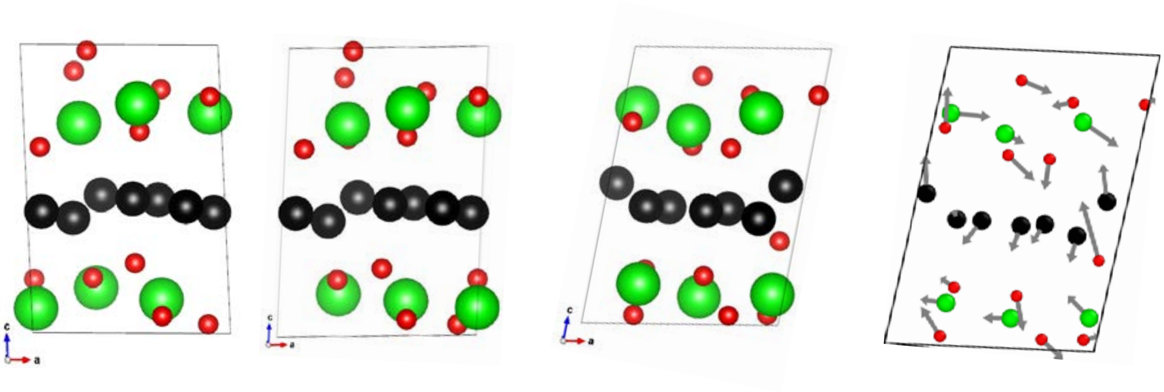

(a) (b) (c) (d)

Figure 51: Shear deformation model with 1-layer Ni along {111}<110> direction after relaxation: (a) initial position, (b) strain 0.126, (c) strain 0.230, and (d) atom displacement vectors between strain 0. 230 and initial steps.

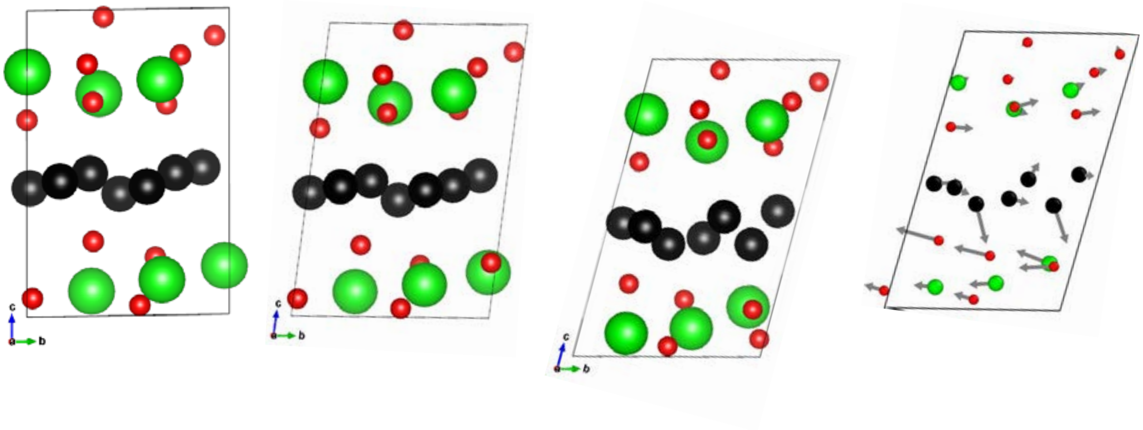

(a) (b) (c) (d)

Figure 52: Shear deformation model with 1-layer Ni along {111}<11$\bar{2}$>direction after relaxation: (a) initial position, (b) strain 0.126, (c) strain 0.267, and (d) atom displacement vectors between strain 0.267 and initial step.

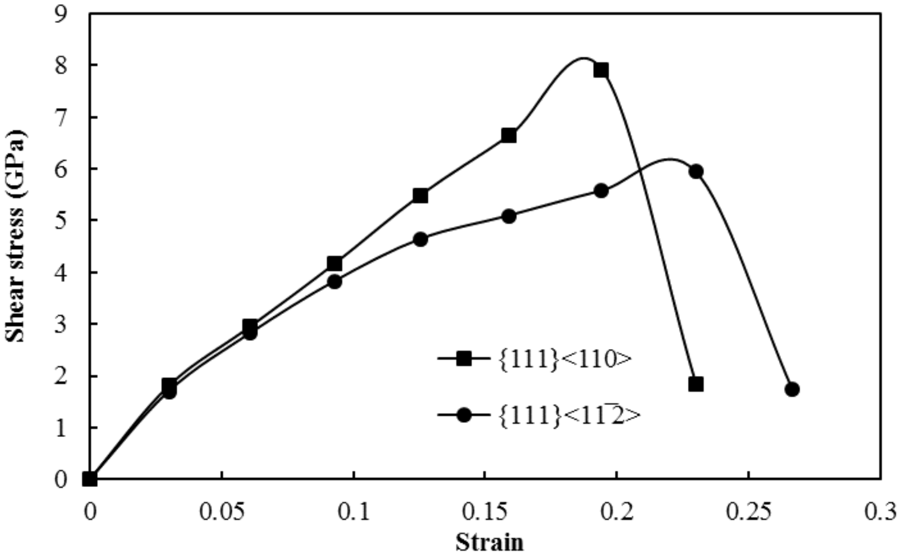

Figure 53: Calculated shear stress-strain curves of 1-layer Ni shear deformation model.

The shear deformations along {111}<110> and {111}<11$\bar{2}$> directions of the 3-layer Ni model are shown in Fig.54 and Fig.55, respectively. The calculated shear stress-strain curves are given in Fig.56. Similar to the 1-layer Ni model, for the 3-layer Ni, both the shear modulus (30.4 GPa) and ultimate shear strength (3.0 GPa) along {111}<110> direction are greater than those along {111}<11$\bar{2}$> direction (17.3 GPa for shear modulus and 1.8 GPa for ultimate shear strength). Therefore, {111}<11$\bar{2}$> is again a favorable shear slip system. Again, the ductility of {111}<110> measured by strain, ~0.10, is lower than that of {111}<11$\bar{2}$>, ~0.11.

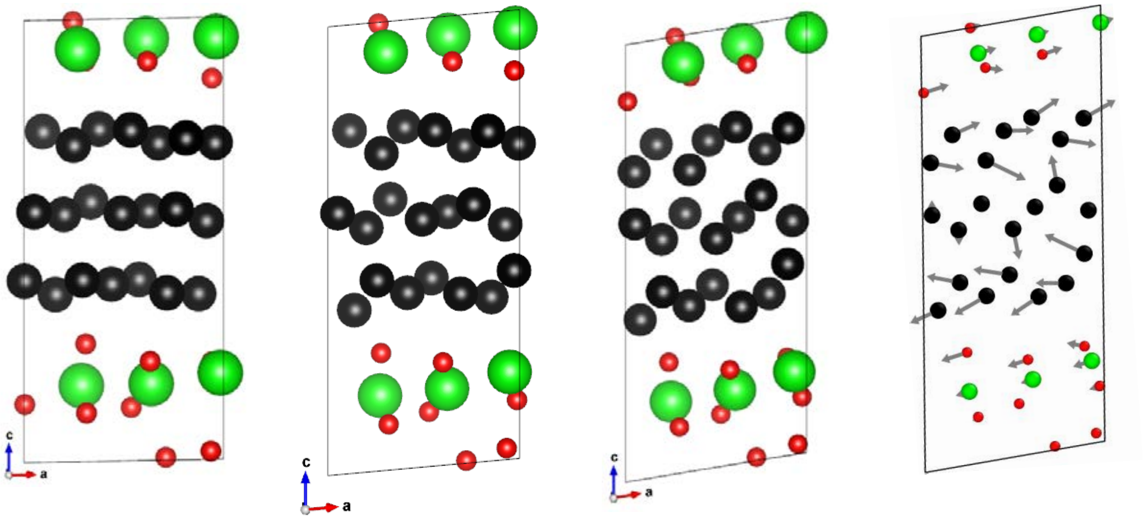

(a) (b) (c) (d)

Figure 54: Shear deformation model with 3-layer Ni along {111}<110> direction after relaxation: (a) initial position, (b) strain 0.051, (c) strain 0.105, and (d) atom displacement vectors between strain 0.105 and initial steps.

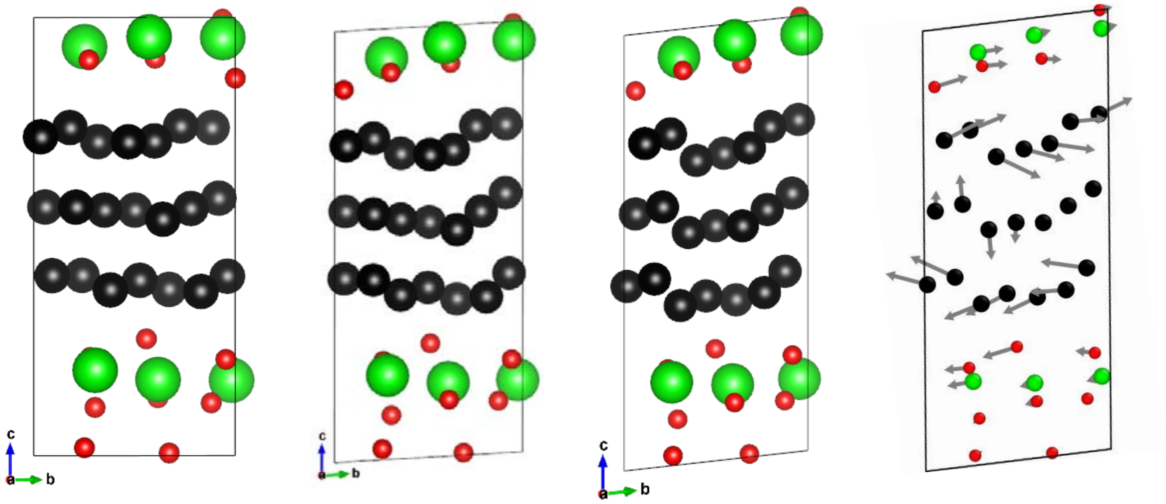

(a) (b) (c) (d)

Figure 55: Shear deformation model with 3-layer Ni along {111}<11$\bar{2}$>direction after relaxation: (a) initial position, (b) strain 0.062, (c) strain 0.116 and (d) atom displacement vectors between strain 0.116 and initial steps.

Comparing with the 1-layer Ni shear deformation model, the shear modulus and strengths in the 3-layer model are much lower by 40%. This is because the shear deformation is primarily achieved by the deformation of Ni atoms. A thicker Ni layer allows to deformation at lower stress level.

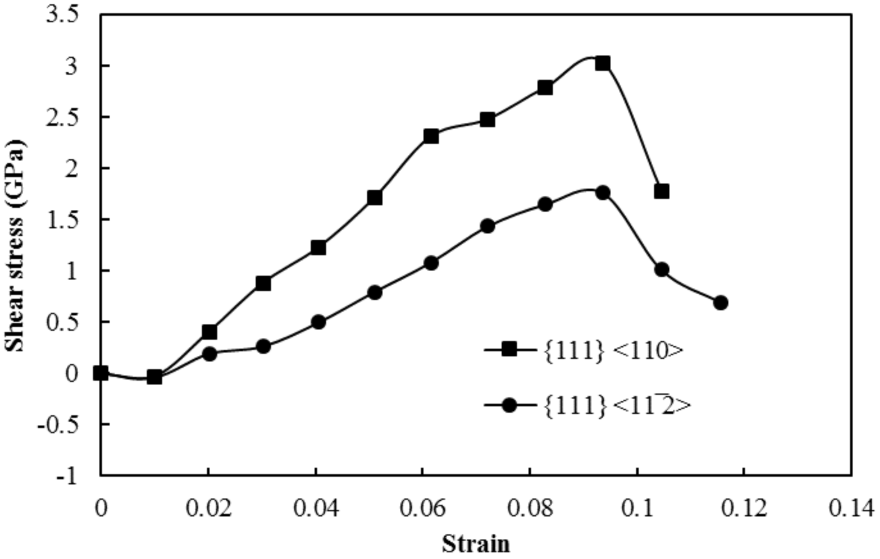

(b)

Figure 56: Calculated shear stress-strain curves of 3-layer Ni shear deformation model.

The atom displacement vectors between the final and initial step of shear deformation models are plotted in Fig.51d, Fig.52d, Fig.54d and Fig.55d. In the 1-layer Ni interface models, there is no obvious difference for the displacement vectors between Ni, Zr and O atoms, as shown in Fig.51d and Fig.52d. However, the displacement directions between upper and lower ZrO_2/Ni interface are in opposite trend, which properly illustrates the shear deformation. As shown in Fig.54d and Fig.55d, the 3-layer Ni interface models show larger displacement in the Ni layers than that in the ZrO_2 layers, indicating that the Ni layers provide the most deformation in these interface models.

In addition to stress, toughness can be used to measure the interfacial strength in large deformations. Toughness is calculated by integrating the are below the stress-strain curve. As shown in Table 9, the 1-layer Ni interface model has higher toughness than the 3-layer Ni model for both tensile and shear deformations. This is also consistent with the results from the adiabatic work of adhesion. In addition, the toughness in {111}<110> system is higher than that of {111}<11$\bar{2}$> direction for both 1-layer and 3-layer Ni models, primarily due to higher shear modulus and ultimate shear strength in the {111}<110> system. It also suggests that the {111}<110> direction is stronger than that of {111}<11$\bar{2}$> direction during interface fracture.

Since most interfacial deformation is achieved by Ni atoms, it is worthy to compare the interfacial models with pure Ni. Ogata *et al.* calculated the shear stress-strain curves of pure Ni in {111}<11$\bar{2}$> direction using the DFT calculations [104]. The calculated ultimate strength is 5.1 GPa. It is similar to the 1-layer Ni interface model in this work, 6.0 GPa. However, the shear modulus in Ogata's work is ~ 60.3 GPa, which is larger than that in this work, 30.9 GPa. Comparing to experimental data, Young's modulus of polycrystalline Ni (190 ~220 GPa) [105] is also much higher than that of ZrO2/Ni interface calculated in this work (139.9 GPa for 1-layer and 60.2 GPa for 3-layer Ni). Both elastic modulus and the ultimate strength values decrease as the increase of the Ni layer thickness. These comparisons suggest that the strength of the ZrO2/Ni interface is substantially different from its pure component, and is determined by the Ni layer thickness.

Table 9: Calculated elastic modulus, ultimate strength, and toughness

Deformation mode, stress direction, and number of Ni layers	Elastic modulus (GPa)	Ultimate tensile/shear strength (GPa)	Toughness (MJ/m^3)
Tensile [111] 1-layer Ni	139.9	11.6	0.728
Tensile [111] 3-layer Ni	60.2	7.9	0.486
Shear {111}<110> 1-layer Ni	43.9	7.9	1.040
Shear {111}<110>	30.4	3.0	1.038

3-layer Ni			
Shear {111}<11$\bar{2}$> 1-layer Ni	30.9	6.0	0.166
Shear {111}<11$\bar{2}$> 3-layer Ni	17.3	1.8	0.096

4.4.3.3 Charge density and Bader charge analyses

The contours of charge density distribution are plotted in Fig.57. As shown in the figure, it is clear that the 1-layer Ni interface models have stronger O-Ni bonds than the 3-layer Ni cases. This is the reason why the 1-layer Ni interface models have higher elastic modulus and strength. The electron localization function (ELF) can be used to describe the electron localization status and bonding behaviors, which depends on the electron density, gradient, and the kinetic energy density [106, 107]. Typically the value of ELF ranges from 0 to 1, which specifies vacuum to perfect localization of the electrons. A higher ELF value in the ELF graph indicates the electron are more localized. Metallic bonding in the ELF graph typically shows electron vacuum near the atom nucleus and a relatively high electron localization value at area far from the atom nucleus. Fig.57 shows the ELF graph of 1-layer and 3-layer Ni shear {111}<110> interface models, ELF graph in other tensile and shear cases shows the similar trend. The ELF of 3-layer Ni model shows electron vacuum near the Ni atom, however, it has a comparatively higher electron localization value in space far from the Ni atom. The Ni layers in the interface model show the typical metallic bonding characteristics, which can accommodate the deformation during the tensile and shear process. This is consistent with the above discussions that thicker Ni layer results to lower elastic modulus and lower ultimate strength.

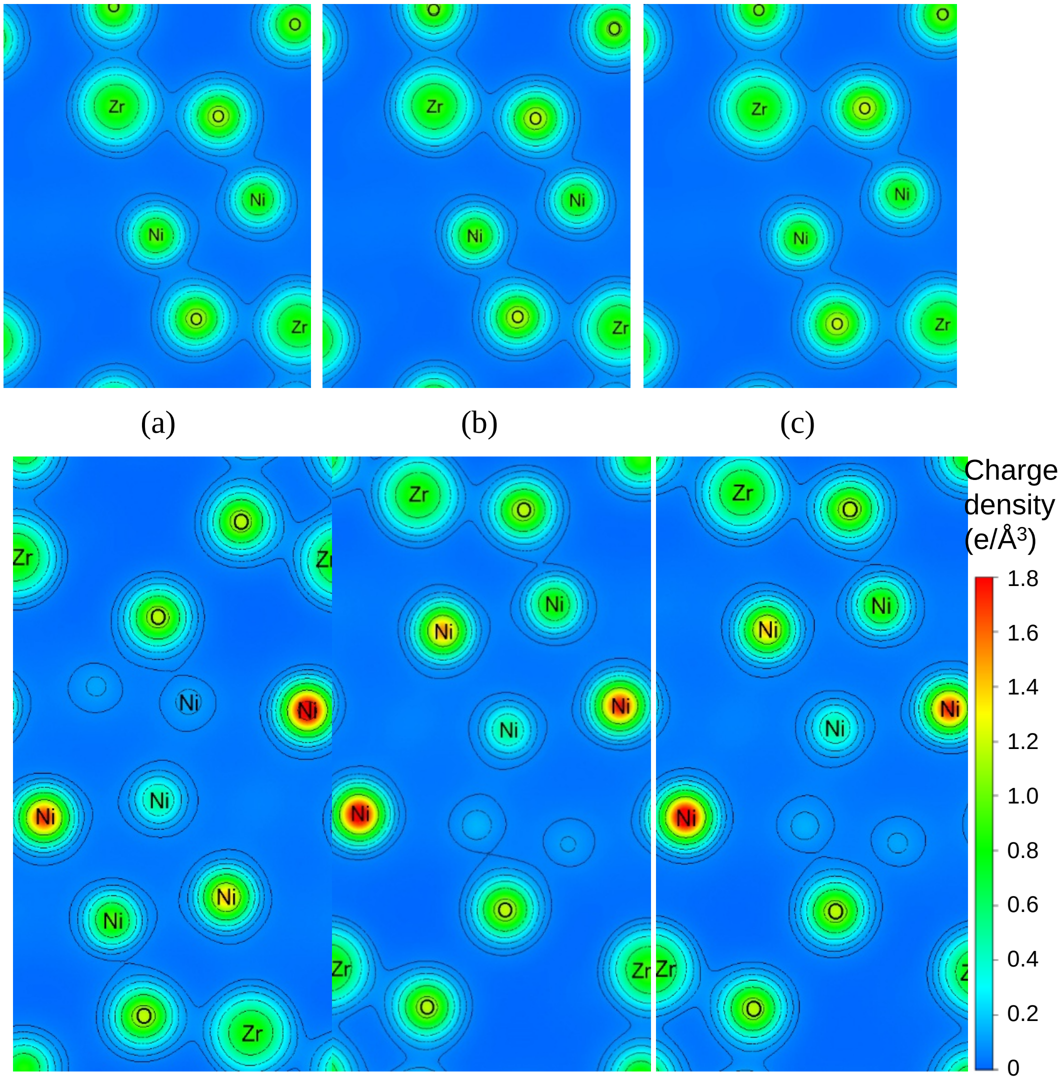

(a) (b) (c)

(d) (e) (f)

Figure 57: Charge density distributions in logarithmic scale: (a) tensile <111> with 1-layer Ni, (b) shear {111}<110> with 1-layer Ni, (c) shear {111}$<11\bar{2}>$ 1-layer Ni, (d) tensile <111> with 3-layer Ni, (e) shear {111}<110> 3-layer Ni, (f) shear {111}$<11\bar{2}>$ 3-layer Ni.

As shown in Fig.58, the O and Zr atoms have higher ELF values than that of the Ni atoms in both 1-layer and 3-layer Ni interface models. The chemical bonding between the O and Ni atom at the interface shows an ionic bonding feature. In addition, both ELF graphs show a delocalized electron gap between ZrO_2 and Ni layer, suggesting the ionic bonding might be weaker than the metallic bonding in Ni layer, which has higher ELF value than ionic bonding. During the tensile and shear processes, the ionic bonding becomes weaker and weaker, until it breaks. Because 1-layer Ni models have stronger ionic bonding than that of 3-layer Ni models, as shown in Fig.57 of the charge density distribution contour, the 1-layer Ni interface models possess higher ultimate strength than that of the 3-layer Ni counterpart.

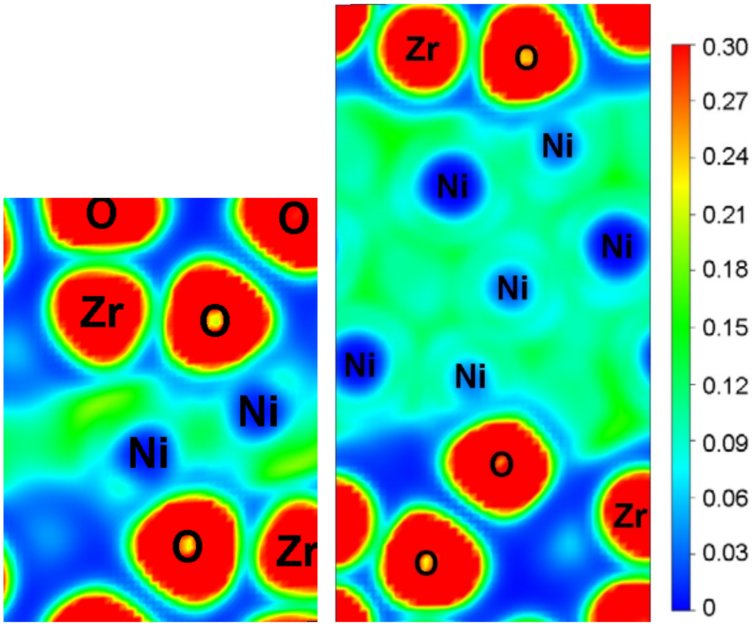

(a) (b)

Figure 58: ELF graphs in the (a) shear {111}<110> 1-layer Ni interface model, (b) shear {111}<110> 3-layer Ni interface model.

To get more quantitative measurements about bond characteristics, the average Bader charge numbers, including O, Zr, Ni ions, and the difference between O and Ni ions for both tensile and shear deformations, are summarized in Table 10. It is clear that the O and Ni differences, the average Bader charge difference between O and Ni ions of 1-layer Ni interface are consistently larger than those of 3-layer Ni interface in both tensile and shear cases. The Bader charge analysis results are also consistent with the charge density distributions in Fig.57. A larger average Bader charge difference indicates a stronger interaction between O and Ni, or more interaction between ZrO2 and Ni. This explains the higher ultimate strength and elastic modulus in the thin Ni layer interface than in the thick Ni layer interface, as listed in Table 10.

Table 10: Average Bader charge number (e)

Deformation mode, stress direction, and number of Ni layers	O	Zr	Ni	Difference between O and Ni
Tensile <111> 1-layer Ni	1.258	-2.457	-0.050	1.308
Tensile <111> 3-layer Ni	1.264	-2.459	-0.019	1.283
Shear {111}<110> 1-layer Ni	1.252	-2.451	-0.045	1.297
Shear {111}<110> 3-layer Ni	1.266	-2.462	-0.019	1.285
Shear {111}<11$\bar{2}$> 1-layer Ni	1.257	-2.460	-0.046	1.303
Shear {111}<11$\bar{2}$> 3-layer Ni	1.265	-2.460	-0.019	1.284

From the calculated mechanical properties of ZrO_2/Ni ceramic-metal interface, the layer thickness of bond coat film, NiCrAlY, at the interface makes a major impact on the coating's mechanical behavior. Typically, fracture or delamination in as-sprayed TBC system occurs near the interfaces between the top and bond coats [39, 45]. Therefore, the mechanical properties near the interface are important to enhance the lifetime performance of TBC system. Higher toughness and elastic modulus at the interface enhance the ability of fracture resistance to impede crack propagations in the ceramic top coat near the interface. From the theoretical analyses of this work, the ultimate tensile and shear strength are decreased with increase of the bond coat film thickness at the interface, which means a thicker thickness of bond coat in TBC system corresponds to a weaker adhesion strength. On the other hand, a thin bond coat film will deteriorate the oxidation resistance of the

TBC system. Therefore, the thickness of bond coat should be properly optimized to design and fabricate robust TBC systems.

4.4.4 MD model of ZrO_2/Ni interface in tensile and shear deformations

The DFT calculation is performed at the ground energy state of the atomic system, which means the DFT theoretical result are limited at very low temperature (close to 0 K). Therefore, MD method was performed to simulate the nanoscale tensile and shear process of ZrO2/Ni interface model at high temperature. LAMMPS code was used to conduct all of the MD calculations in this work. The charge-optimized many body potential (COMB3) was applied to describe the interatomic force field of ZrO_2/Ni interface [108]. In COMB potential series (including both COMB and COMB3), the total potential energy U^{tot} of system is described by:

$$U^{tot}(r,q) = U^{es}(r,q) + U^{short}(r,q) + U^{vdW}(r) + U^{corr}(r) \tag{31}$$

where r represents the coordinate array of the system and q represents the charge array. U^{es} represents the electrostatic energies that include the energies to form a charge on an atom, the charge-nuclear interaction, the charge-charge interaction and the energies related with atomic polarizability. U^{short} is the short-range interaction energies that describe the pairwise repulsive and attractive potentials. The long-range van der Waals interactions (U^{vdW}) is described using Lennard-Jones expression. The energy corrections term (U^{corr}) were used to optimize the total energy.

To validate the COMB3 potential in ZrO_2/Ni interface system the lattice constants of ZrO_2 unit cell and Ni unit cell were calculated using MD model, respectively. Cubic ZrO_2 with a space group *Fm3m* and cubic Ni of the same space group are used to calculate the lattice constant. The DFT calculation methods are similar to the one used in LZ unit cell model, except different cutoff energy and Brillouin zone k-point scheme. The cutoff energy for ZrO_2 and Ni were 500 eV and 300 eV, respectively, and the 5×5×5 Monkhost-Pack scheme was used for both ZrO_2 and Ni as Brillouin zone k-point. Table 11 shows the DFT and MD calculation results of the ZrO2 and Ni lattice constants. The error difference between MD results and DFT results for ZrO2 and Ni are 1.478 % and 0.378 %, respectively, suggesting that the COMB3 potential is reliable in single material ZrO_2 or Ni MD models.

Table 11: DFT and MD calculated lattice constant and work of adhesion results

	DFT calculated result	MD calculated result
Lattice constant ZrO_2 (Å)	5.146	5.070
Lattice constant Ni (Å)	3.514	3.527
Work of adhesion with 1 layer ZrO_2 (mJ/m^2)	629	751
Work of adhesion with 2 layer ZrO_2 (mJ/m^2)	554	602
Work of adhesion with 3 layer ZrO_2 (mJ/m^2)	296	378

The ZrO_2/Ni interface MD models were built based on the DFT model, and the lattice mismatch was less than 3%. The work of adhesion of ZrO_2(111)/Ni(111) interface was calculated using MD method, and it was compared with DFT results. The calculated work of adhesion results are listed in Table 11 and plotted in Fig.59. The MD calculated work of adhesion result has the same trend as DFT results and a moderate accuracy, which is acceptable in the interface simulations.

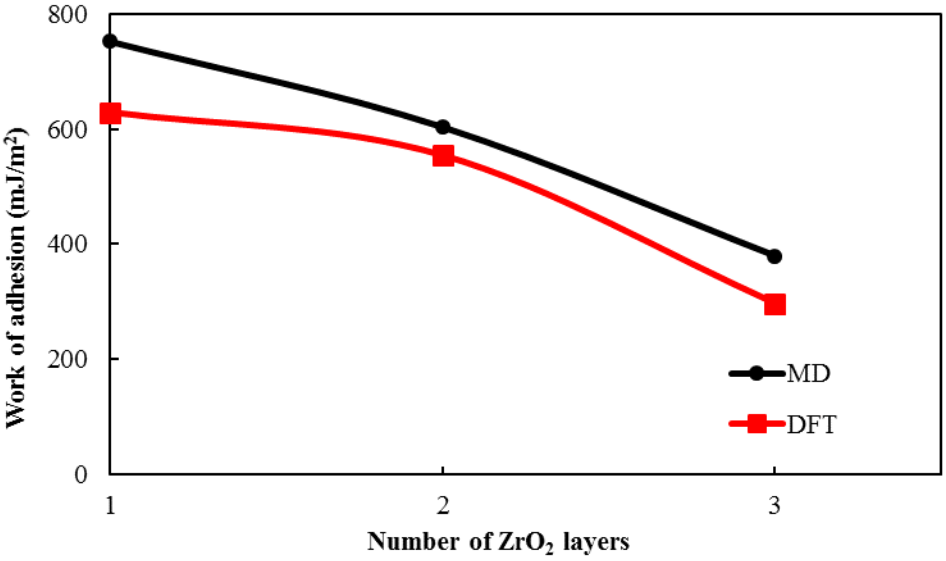

Figure 59: Comparison of work of adhesion between DFT and MD models.

The tensile stress-strain curves of ZrO_2/Ni interface model were calculated using the same scheme as LZ model. However, the shear stress and strain values here were calculated from the single direction pure shear deformation. Therefore, the shear strain was represented by the deformation angle, and shear stress was calculated from the elastic constants.

The MD models of ZrO_2 (111)/Ni(111) interface before and after the tensile simulation are shown in Fig.60. The periodic boundary condition was applied in all three dimension of this tensile model, so the ZrO_2-Ni-ZrO_2 sandwich model was built to match the periodic condition in the tensile direction. As shown in Fig.60b, the Ni layer in the model with 0.16 tensile strain did not keep the initial lattice array, suggesting that the primary deformation came from the Ni layer.

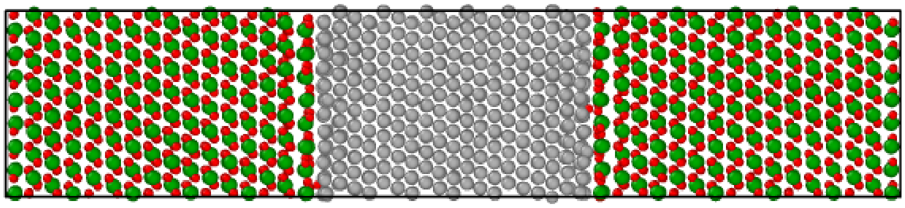

(a)

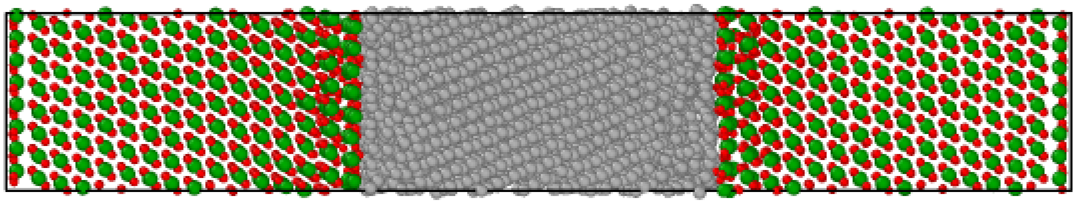

(b)

Figure 60: MD ZrO_2(111)/Ni(111) interface model in tensile simulations at 300 K (a) initial position with 0 strain (b) the position of tensile strain 0.16, Green, red, and grey balls represent Zr, O, and Ni atom, respectively (same coloring schemes are used in all of the MD figures afterwards).

The MD ZrO_2(111)/Ni(111) interface model used in the shear simulation of {111}<110> direction at 300 K are shown in Fig.61. The non-periodic boundary condition was applied in the shear direction, and the periodic boundary condition was used in the other two dimensions.

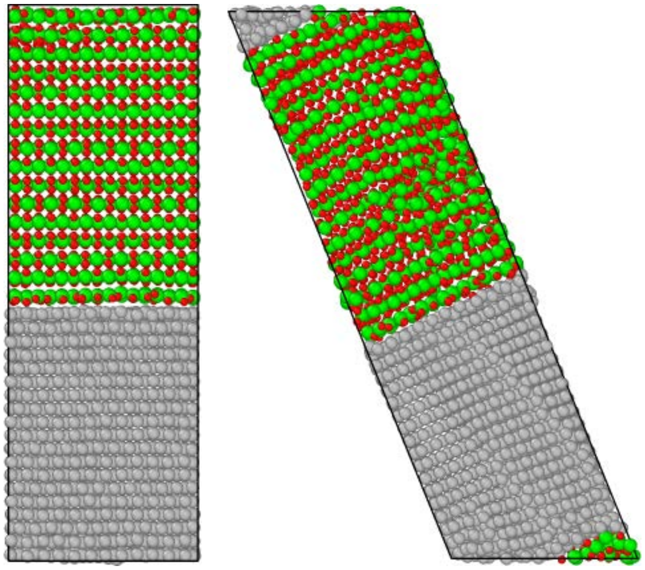

(a) (b)

Figure 61: MD ZrO2(111)/Ni(111) interface model in shear simulation in {111}<110> direction (a) initial position with 0 strain (b) the position of shear strain 0.35.

The tensile stress-strain curves of ZrO_2(111)/Ni(111) interface model in [111] direction and ZrO_2(100)/Ni(100) model in [100] direction at 300 K are shown in Fig.62.

The tensile curve in [111] direction reaches its ultimate strength of ~15 GPa at the strain of 0.143. The MD calculated ultimate strength is in the similar level but larger than the DFT calculated results. The undulation of the curve is due to the limitation of the atom numbers. The average Young’s modulus in [111] direction is 131.56 GPa, which is similar as the DFT result of 1 Ni-layer interface model as listed in Table 11 (139.9 GPa). The average Young’s modulus in [100] is 127.85 GPa, which is slightly lower than that in [111] direction. However the ultimate strength in [100] direction is only ~10 GPa, which is about two thirds of that in [111] direction, indicating that the mechanical strength of ZrO2/Ni interface in [111] direction is much stronger than that in [100] direction.

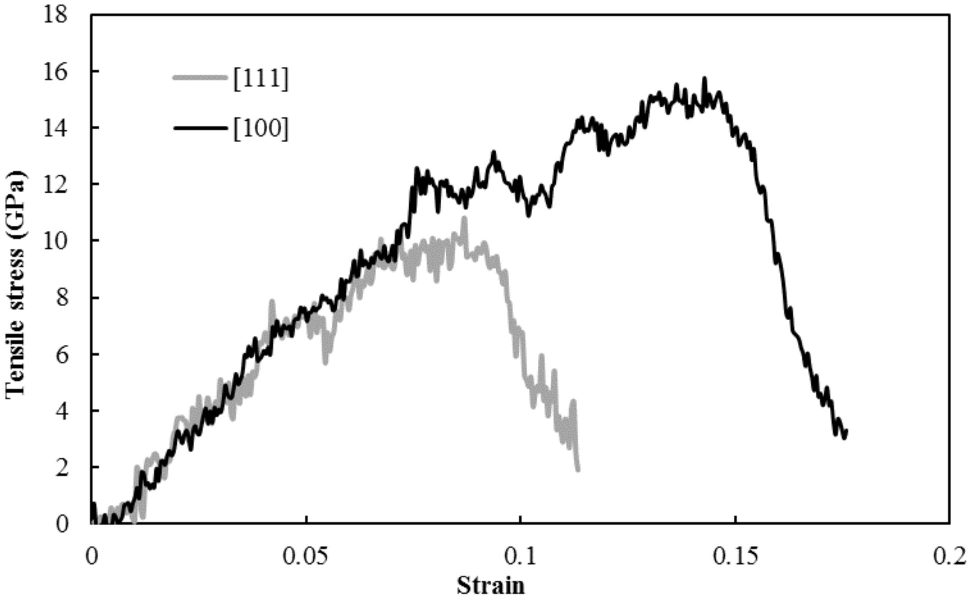

Figure 62: Tensile stress-strain curves of ZrO_2/Ni interface at 300 K.

The shear stress-strain curves in {111}<11$\bar{2}$> and {111}<110> direction at 300K are shown in Fig.63. These two curves share the similar shear stress-strain trend as the thin-Ni-layer DFT results. The ultimate shear strength in {111}<11$\bar{2}$> direction is ~9 GPa at the shear strain of ~0.31. The average shear modulus in {111}<11$\bar{2}$> is ~29.4 GPa. The ultimate shear strength in {111}<110> direction is ~12 GPa at the shear strain of ~0.29. The average shear modulus in {111}<110> is ~34.5 GPa. The ultimate strength is larger than DFT calculated results. The shear modulus is similar to the DFT calculated results.

These ultimate strength and elastic modulus differences between DFT and MD results are due to the dimension scale and atom number differences. In addition, the MD calculation is performed in a dynamic equilibration, and the DFT calculations are conducted in the static equilibration of each tensile steps.

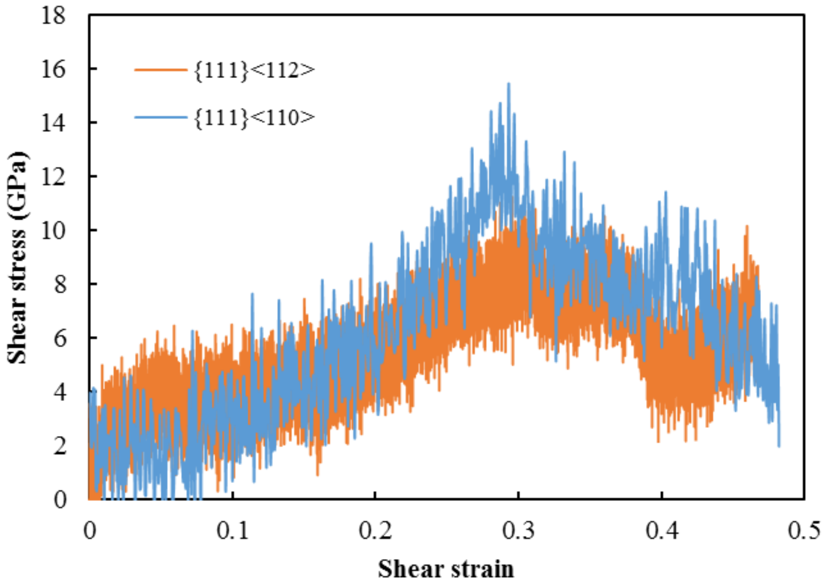

Figure 63: Shear stress-strain curves of ZrO_2/Ni interface at 300 K.

4.4.5 Summary of modeling of mechanical properties of ZrO2/Ni interface

The ideal tensile strength and shear strength of ZrO_2/Ni ceramic-metal interface are calculated using the DFT and MD methods. The major conclusions are summarized below:

(1) For tensile deformation in [111] direction, Young's moduli of the 1-layer Ni and 3-layer Ni metal-ceramic models are 139.9 GPa and 60.2 GPa, respectively; the ultimate tensile strengths are 11.6 GPa and 7.9 GPa, respectively; the toughnesses are 0.728 MJ/m^3 and 0.486 MJ/m^3, respectively. The 1-layer Ni model shows higher mechanical strength than the 3-layer Ni model in tensile deformation.

(2) For shear deformation in {111}<110> system, the shear moduli of the 1-layer Ni and 3-layer Ni M-C models are 43.9 GPa and 30.4 GPa, respectively; the ultimate shear strengths are 7.0 GPa and 3.0 GPa, respectively; the toughnesses are 1.040 MJ/m^3 and

1.038 MJ/m^3, respectively. The 1-layer Ni model shows higher mechanical strength than the 3-layer Ni model in shear deformation.

(3) For shear deformation in {111}<11$\bar{2}$> system, the shear moduli of the 1-layer Ni and 3-layer Ni metal-ceramic models are 30.9 GPa and 17.3 GPa, respectively; the ultimate shear strengths are 6.0 GPa and 1.8 GPa, respectively; the toughnesses are 0.166 MJ/m^3 and 0.096 MJ/m^3, respectively.

(4) Both charge distribution and Bader charge analyses show that the 1-layer Ni ceramic-metal model has stronger interaction between Ni and O ions than that of the 3-layer Ni model, which explains the higher mechanical properties in 1-layer Ni model from the calculated tensile and shear stress-strain results.

(5) From the theoretical analyses of this work, the ultimate tensile and shear strengths are decreased with the increase of the bond coat film thickness at the interface, which means a thicker thickness of bond coat in TBC system corresponds to a weaker adhesion strength. On the other hand, a thin bond coat film will deteriorate the oxidation resistance of the TBC system. Therefore, the thickness of bond coat should be properly optimized to design and fabricate robust TBC systems.

Task 5: Durability of LZ based TBCs at elevated temperatures

Task 5.1: Heat treatment test

Furnace heat treatment tests were conducted on sample 6, 7, 8 and 9 with round button substrate in a diameter of 25.4 mm (1 inch) at 1353 K (1080 ^{o}C) for 4 hrs in an argon atmosphere.

The optical images of the TBC samples before and after the furnace heat treatment are summarized in Fig.64. After furnace heat treatment for 4 hrs, the sample 6 (SCL LZ coating, Fig.64a and sample 8 (the DCL with the dense 8YSZ and LZ layers, Fig.64c were completely delaminated. One of the main reasons for the failure was the CTE differences among the bond coat, the 8YSZ layer, and the LZ layer. In the isothermal heating process, volume change due to the thermal expansion mismatch between the bond coat and the LZ layer led to high thermal residual stresses, which initiated cracks in ceramic top coats, as indicated in the calculated residual stress distribution. Additionally, the fracture toughness of LZ is ~1.1 MPa·m$^{1/2}$, which is much lower than that of 8YSZ (2.0 MPa·m$^{1/2}$) [18, 19]. As a result, cracks tended to be extended inside the LZ coating layer in the early stage of heat treatment. The failure ultimately occurred in the LZ coating layer due to its low fracture toughness and the CTE mismatch between the bond coat and the LZ layer or between the LZ and the 8YSZ layers. In contrast with the finding for sample 8, the sample 7 (DCL with the porous 8YSZ and LZ layers) was partially cracked on the edge, which only took up about 10% of the coated area, as shown in Fig.64b. As the porosity of the porous 8YSZ coating was more than two times higher than that of the dense 8YSZ coating, the porous 8YSZ coating had greater compliance to accommodate the volume mismatch caused by the CTE differences, so the double-layer top coat of the sample 7 survived in the heat treatment test. On the other hand, the low compatibility of the dense 8YSZ coating in sample 8 led to its complete failure in the heat treatment. As shown in Fig.64d, the sample 9 (SCL porous 8YSZ coating) was in good condition after heat treatment for 4 hrs, suggesting the porous 8YSZ layer has good adhesion in TBC systems.

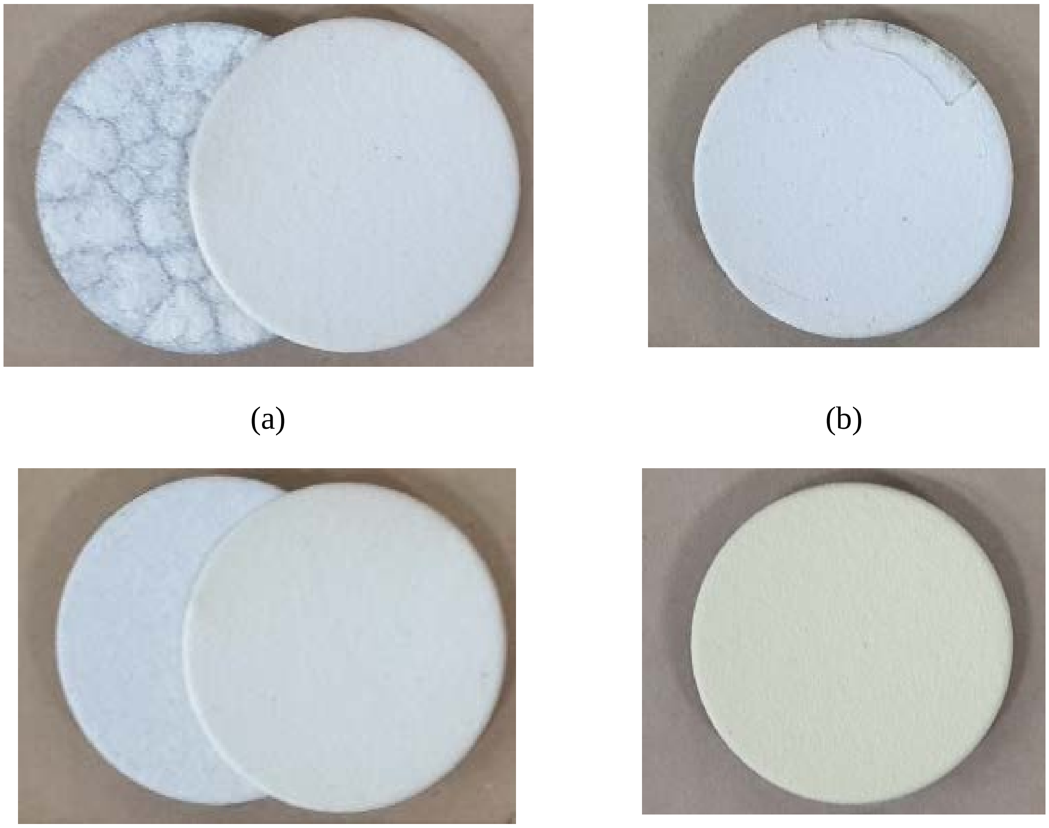

(a) (b)

(c) (d)

Figure 64: Optical images of the TBC samples after furnace heat treatment: (a) single-layer LZ coating, (b) double-layer coating with porous 8YSZ and LZ, (c) double-layer coating with dense 8YSZ and LZ, and (d) single-layer porous 8YSZ coating.

Fig.65 shows the SEM images of the cross-sectional view of TBC microstructures after heat treatment for 4 hrs. Except for sample 9, delamination in all of the samples occurred in the LZ layer (the SEM microstructure image of sample 7 was taken at the delaminated area). Therefore, CTE difference should not be the only reason for delamination of the single-layer LZ coating. The occurrence of cracks is also related to fracture toughness [37]. Delamination can more easily occur in the single-layer LZ coating due to the low fracture toughness of LZ. Failure in the LZ coating is likely caused by a combination of its low fracture toughness and high stresses created by CTE mismatch. Levi *et al.* proposed that elastic energy played a critical role in TBC systems to determine the lifetime of coating [38].When the elastic energy reaches the critical energy value, delamination occurs. This elastic energy can be estimated using coating thickness, Young’s modulus, and CTE [38]. The cause of delamination in sample 8 is similar to the single-layer LZ coating, namely a combined effect of both CTE difference and low fracture toughness of LZ.

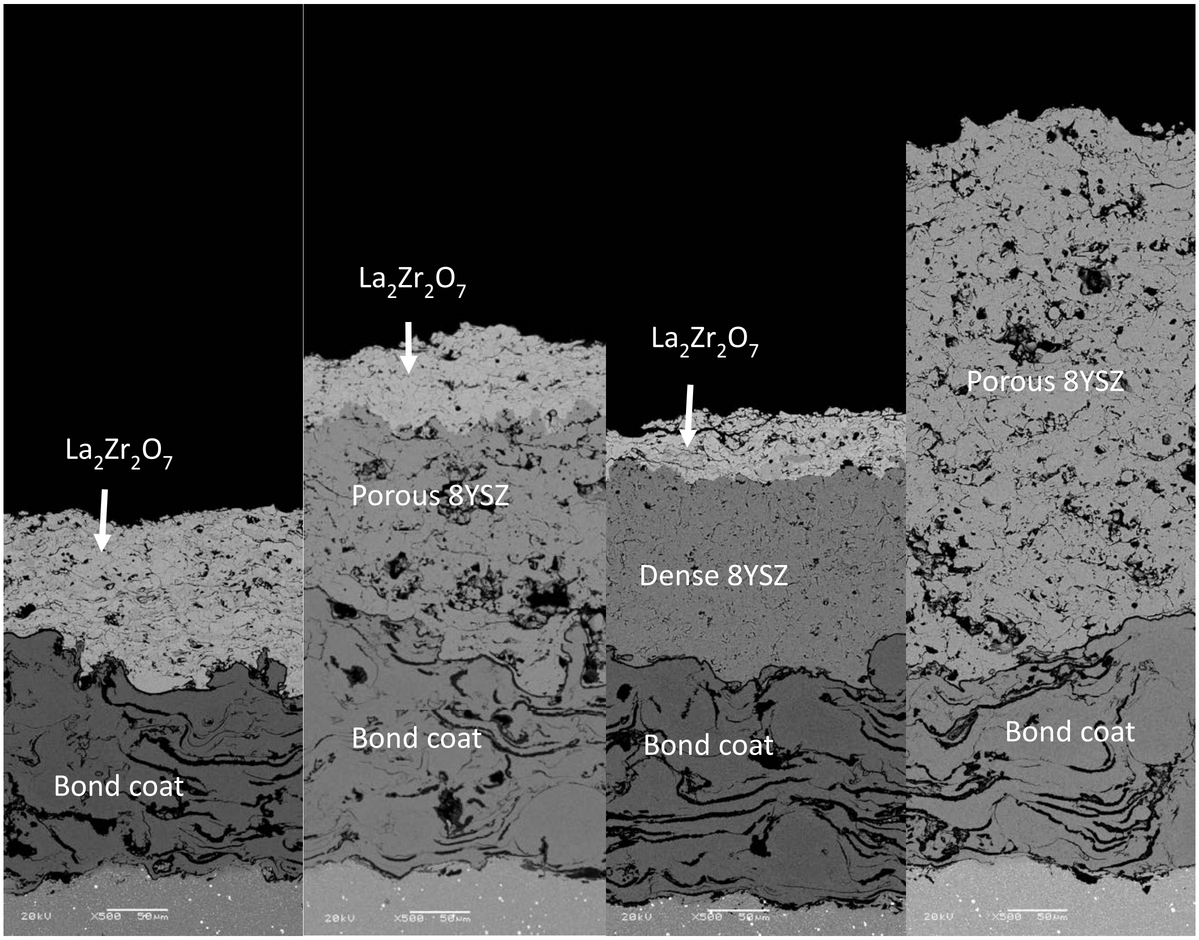

(a) (b) (c) (d)

Figure 65: SEM images of the cross sectional view of the TBC samples after furance heat treatment: (a) fully delaminated SCL LZ coating, (b) edge delaninated DCL coating with porous 8YSZ and LZ, (c) fully delaminated DCL with dense 8YSZ and LZ, and (d) SCL porous 8YSZ coating.

In addition, the heat treatments were also performed on TGMF dog-bone samples at 1353 K (1080 ^{o}C) for 4 hrs. However, the TGMF tensile bar samples show better performance than the aforementioned round button samples. Only single layer LZ TGMF samples were delaminated. 8YSZ and LZ double layer coatings were in a good condition after 4hours heat treatment. The delamination of single-layer LZ coating is mainly because of the week fracture toughness of LZ coating. The volume changes due to the discrepancy of thermal expansion coefficient between bond coat and LZ coat led to high thermal stress. The failure ultimately occurred due to the large residual stress in the thermally grown oxide through its roles in amplifying the imperfections near the interface [39].

Task 5.2: Furnace cycling test (FCT)

The FCT experiments were conducted on sample 6, 7, 8 and 9 between high temperature 1366 K (1093 ^{o}C) and room temperature. In each cycle, samples were heated at 1366 K for 50 minutes and then cooled by compressed air for 10 minutes. It is recognized as a failure when more than 20% surface area of top coat is delaminated.

All LZ coats layers were delaminated in the first 20 cycles in the FCT experiments. However, no significant delamination occurred in SCL porous 8YSZ coating after 2000 cycles. Because the coefficient of thermal expansion (CTE) of LZ (9-10 $\times 10^{-6}$ /K) is much lower than that of 8YSZ (10-11 $\times 10^{-6}$ /K), and bond coats have even higher CTE (about 15×10^{-6} /K). The CTE difference between LZ and bond coat is larger than that between 8YSZ and bond coat, which leads to higher thermal stresses in LZ layers [12, 40]. The low fracture toughness means the resistance for the crack propagation in LZ material is very weak, so the crack is more easily to propagated in LZ than in YSZ. The failure mechanism for the LZ coating is associated with the large residual stress at the interface due to the large CTE difference and the low fracture toughness of LZ.

Task 5.3: Jet engine thermal shock (JETS) test

The JETS tests were conducted to investigate the thermal shock and thermal cycling performance. During JETS tests, the TBC samples were heated to 1505 K (1232^{o}C) at the center for 20 seconds, and then were cooled by compressed N_2 gas for 20 seconds, followed by ambient cooling for 40 seconds. The heating and cooling cycles were repeated until the TBC samples failed. The failure criterion in the JETS tests was more than 20% spallation of the TBC surface [41]. For each type of coats, at least 3 samples were tested in the JETS tests. Both the front and back side temperatures were measured during the test through two-color pyrometers to investigate the temperature gradient across sample thickness. The TBC samples were sectioned and polished according to the ASTM standard E1920-30 to examine their microstructures using a scanning electron microscope (SEM, JEOL Model JSM-5610, Japan).

The number of cycles-to-failure and final top coat status after the JETS tests are summarized in Table 12. During the JETS tests, the single-layer LZ coating was completely delaminated within 25 cycles, and the double-layer coating with the dense 8YSZ and the LZ was completely delaminated in about 885 cycles. Delamination happened near the interface between the dense 8YSZ layer and the LZ layer in the double-layer coating. However, the double-layer coating with the porous 8YSZ and LZ was only partially delaminated at edges after 2000 cycles and the cracked edge area took up about 20% of the total area of the top coat. In the remaining area, the top coat of LZ was still bonded with the porous 8YSZ layer. The double-layer coating with the porous 8YSZ and LZ had a better performance than other LZ based coatings. The single-layer porous 8YSZ coating was intact after 2000 cycles.

Table 12: Summary of the number of cycles and final status in JETS tests

	#6, SCL LZ	#7, DCL porous 8YSZ + LZ	#8, DCL dense 8YSZ + LZ	#9, SCL porous 8YSZ
Number of cycles before complete delamination	25	>2000	885	>2000
Failure status	Complete delaminated	Edge crack	Complete delaminated	Intact

The optical images of the TBC samples after the JETS tests are given in Fig.66. The single-layer LZ coating sample is shown in Fig.66a, in which the LZ top coat was completely delaminated from the bond coat. Only the bond coat remained. The double-layer coating with the dense 8YSZ and LZ is shown in Fig.66c. In this figure, the delaminated LZ coating fragments were laid on the top surface, although it already detached from the dense 8YSZ layer. The bright area is the dense 8YSZ layer, and the dark gray region is the LZ layer. After the JETS tests, only the dense 8YSZ layer was left on the substrate. The LZ top coat was totally lost during the JETS tests. Delamination occurred between the 8YSZ and LZ layers. The single-layer porous 8YSZ coating is shown in Fig.66d. The 8YSZ top coat was almost intact after 2000 cycles, suggesting good thermal shock resistance. The three black marks on the edge of the samples in Fig.66a and Fig.66d were caused by sample holding clips. The double-layer coating with the porous 8YSZ and LZ is shown in Fig.66b. The coating survived after the JETS tests with cracks on the edge of LZ top coat. The double-layer coating with the porous 8YSZ and LZ showed a considerably better performance than the single-layer LZ coating and the double-layer coating with the dense 8YSZ and LZ. Heating and cooling cycles led to the thermal residual stresses in TBC systems. The residual stress levels are proportional to the distance from the interface [18]. For the double-layer coating with the porous 8YSZ and the LZ, the stress level at the interface between the 8YSZ and LZ layers was less than that at the interface between the 8YSZ and the bond coat.

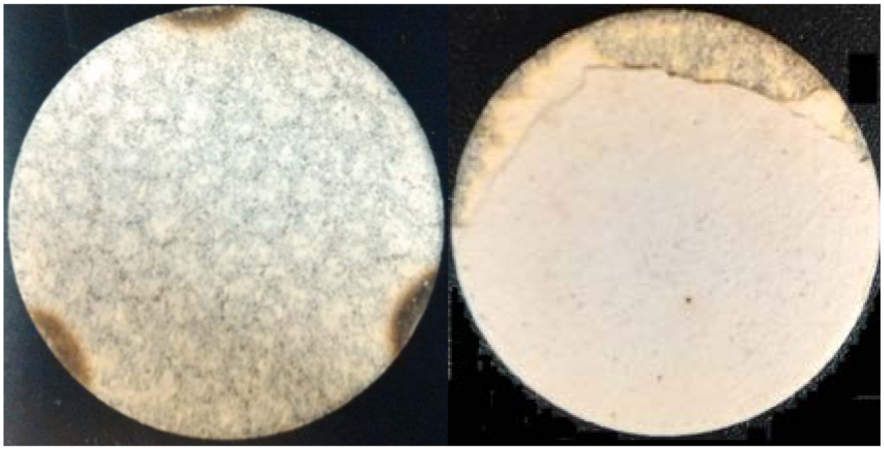

(a) (b)

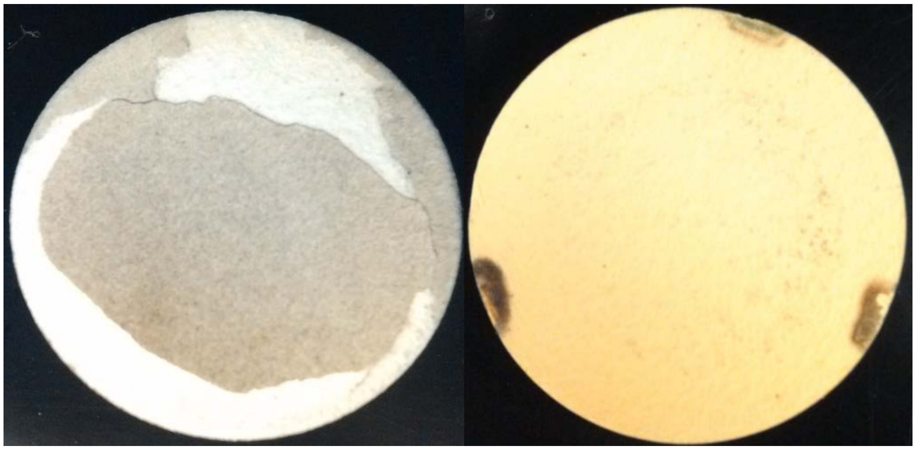

(c) (d)

Figure 66: Optical images of the TBC samples after JETS tests: (a) single-layer coating with LZ, (b) double-layer coating with porous 8YSZ and LZ, (c) double-layer coating with dense 8YSZ and LZ, and (d) single-layer porous 8YSZ coating.

The temperature differences between the front and back surfaces of the samples during the JETS tests are shown in Fig.67. Fig.67a shows the temperature difference in the cycle range from 0 to 2000, and Fig.67b is in the cycle range from 0 to 50. As shown in Fig.67a, the curve of double-layer coating with the dense 8YSZ and LZ showed a sudden temperature change between 660-885 cycles, which is an evidence of delamination. However, the double-layer coating with the porous 8YSZ and LZ, including the single-layer porous 8YSZ coating, did not show a large temperature change, suggesting that the double-layer coating with the porous 8YSZ and LZ had a similar performance in the JETS tests as that of 8YSZ. However, the double-layer coating with the porous 8YSZ and LZ showed smaller temperature drops (56 K on average) than the single-layer 8YSZ coating, although thermal conductivity of the as-sprayed single-layer 8YSZ coating is higher than that of the single layer LZ coating. In the JETS tests, the temperature drops of the single-layer and double-layer coatings are not simply related to the thermal conductivities of as-sprayed coatings. The temperature drops of the single layer porous 8YSZ coating can be higher than those of the double-layer coatings with 8YSZ and LZ, due to the porosity difference, the interface roughness, sintering and thermal conductivity change in the JETS tests. In addition, the 8YSZ single layer coating was thicker than the double-layer coatings, so the temperature drops in the single layer 8YSZ coating can be larger than those of double-layer coatings.

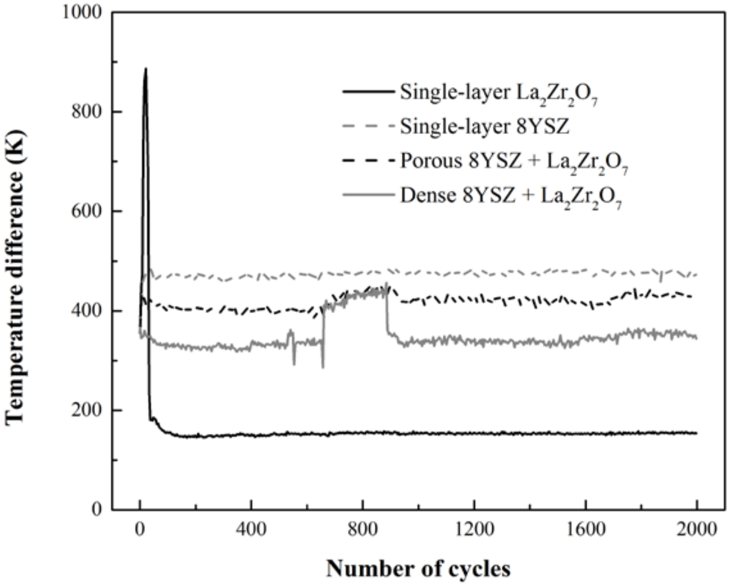

(a)

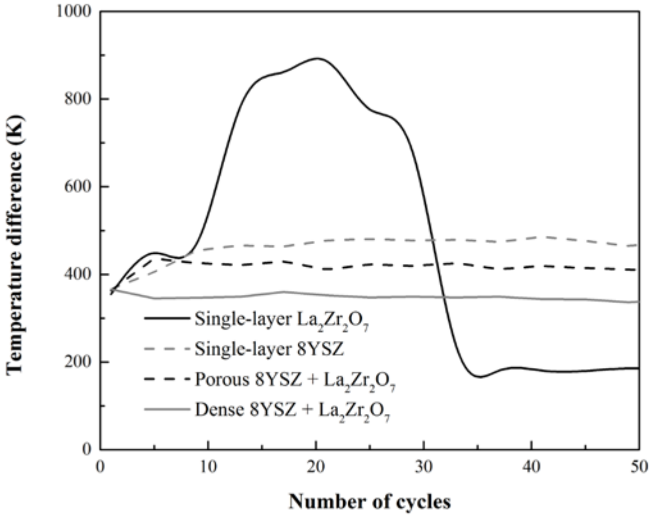

(b)

Figure 67: Average temperature differences during JETS tests: (a) number of cycles from 0 to 2000 and (b) number of cycles from 0 to 50.

As shown in Fig.67b, the temperature differences of the single-layer LZ coating bumped up after 10 cycles and then dropped after 25 cycles. The gaps between the top and bond coats caused the increase of front-back surface temperature differences, indicating that the LZ top coat partially delaminated from the bond coat after 10 cycles. The top surface temperature of single-layer LZ coating reached to 2032 K (1759 ^{o}C) after 13 cycles due to accumulate of heat. As the top coat delaminated after 25 cycles, the bond coat and substrate were exposed to the JETS flame directly, causing a reduced temperature difference, as shown in Fig.67b.

While the sprayed coating samples were heated and cooled in the thermal cycling test, thermal residual stress was generated in the TBCs layers due to the different CTE value between each layer. When the coating sample was heated, tensile stress was generated in the top and bond coat, and the compressive stress in the substrate. When the coatings were cooled from the high temperature, the compressive and shear stresses were generated in the top and bond coat, and the tensile stress in the substrate.

The thermal residual stresses were calculated during the heating and cooling process. The residual stress distributions across the coating thickness of sample 6, 7, 8, and 9 are shown in Fig.68. The thermal residual stress difference at the interface between the top and bond coat of SCL LZ coat is larger than that of SCL porous 8YSZ coating. The stress differences at the interface between LZ and 8YSZ layers in DCL coatings were much smaller than that between the top coat and bond coat in the SCL LZ coating. Although the stress differences between the two DCL coatings were similar, the stress difference in sample 7 is smaller than that of sample 8. As a result, the SCL LZ coating was easily delaminated due to its larger residual stress and low fracture toughness, and sample 7 (porous 8YSZ + LZ) was survived due to its lowest residual stress at the interface and the stress accommodation characteristic from porous 8YSZ buffer layer.

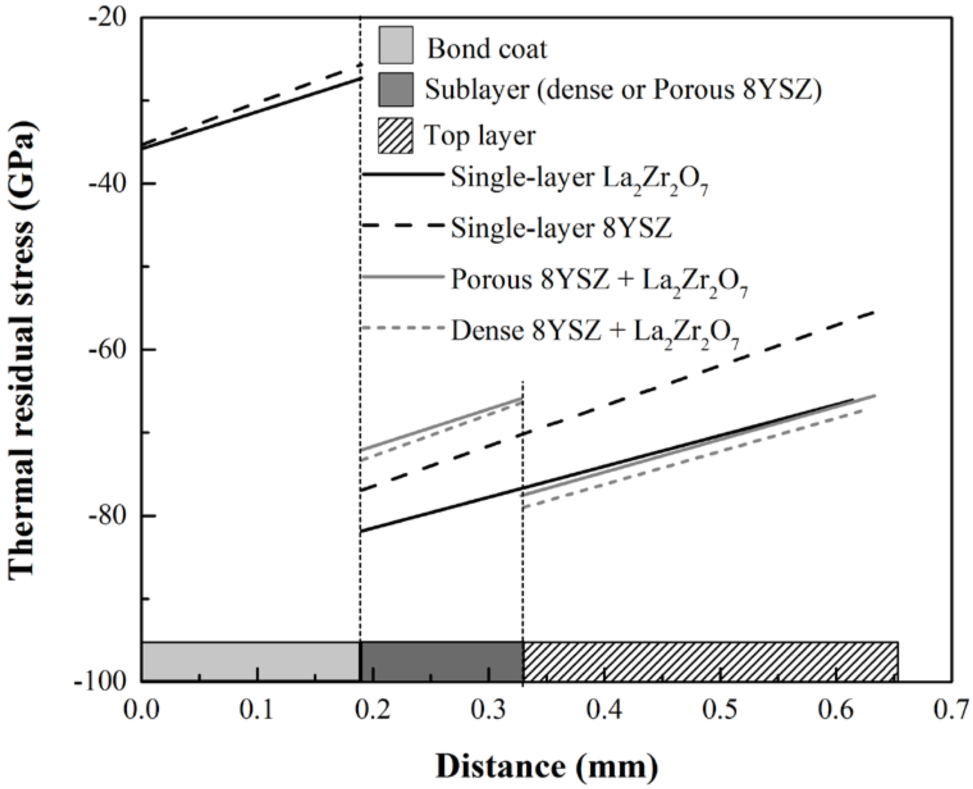

Figure 68: Calculated residual stress distributions as a function of thickness in four TBC samples.

Task 5.4: Thermal gradient mechanical fatigue (TGMF) test

The thermal gradient mechanical fatigue (TGMF) tests combine the thermal exposure and mechanical loading test together, which introduce a thermal gradient over the tensile bar [42]. The experiments were conducted in argon atmosphere using tensile bar samples. A constant load of 150 N was added on the tensile bar during the thermal exposure, as shown in Fig.69. The samples were heated to 850 ^oC or 1100 ^oC for 10 minutes on the top coating side and kept at a constant temperature 350 ^oC on the back side, as shown in Fig.70.

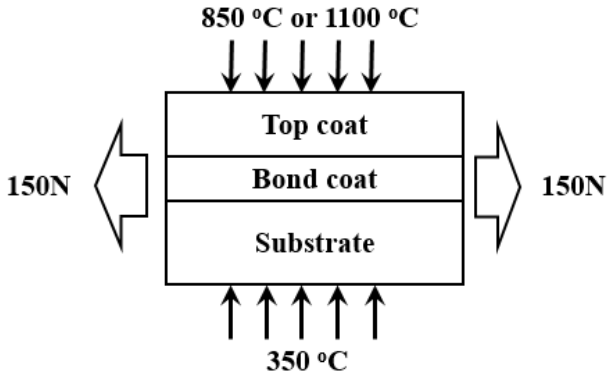

Figure 69: Schematics of TGMF test.

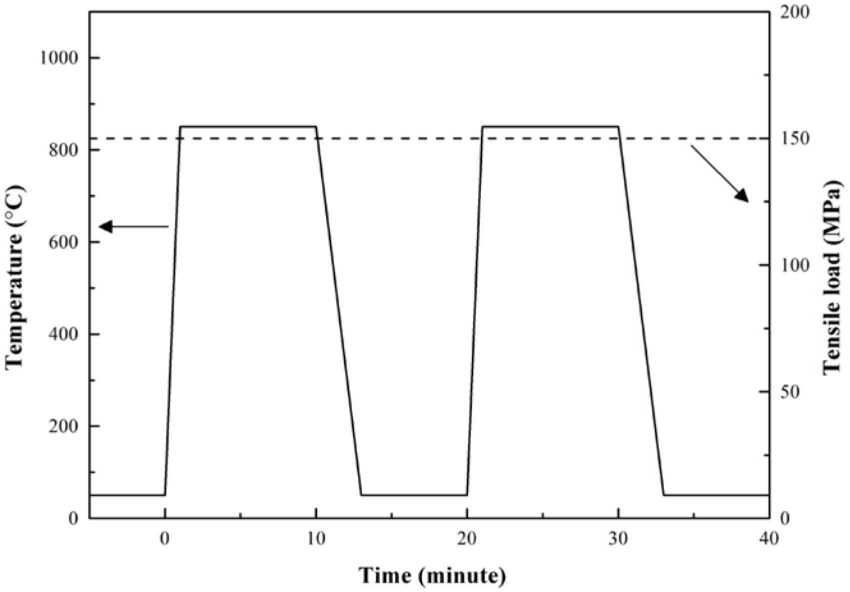

Figure 70: TGMF loading and heating and loading regime.

The thermal gradient is established during TGMF test across the TBC samples. After the heating process, the samples were cooled on front surface using a compressed air for 3 minutes and using ambient cooling for another 7 minutes. The thermal cycling experiments were repeated in this temperature control regime until the failure occurred. The failure criterion is the spallation for more than 20% of the surface area.

The TGMF tests in this work were categorized in two sets which were conducted in two different temperatures gradient environment. The first set of experiments heated 850 ^{o}C in the front side and kept 350 ^{o}C in back side; the second set heated the sample 1100 ^{o}C in front and kept 350 ^{o}C in back.

Fig.71 shows the optical images of the samples before and after the first set TGMF tests. As shown in Fig.71e and Fig.71f, after 1200 cycles, there was no crack or spallation tendency in SCL porous 8YSZ coats. As shown in Figs.71a - 71d, the double layer LZ cannot last many cycles. In Fig.71a and Fig.71b, DCL porous 8YSZ and LZ coats (sample 7) delaminated on the edge after 220 TGMF cycles. In Fig.71c and Fig.71d, DCL dense 8YSZ and LZ coats delaminated after 50 cycles.

(a)

(b)

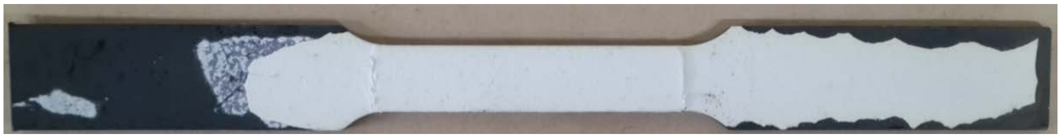

(c)

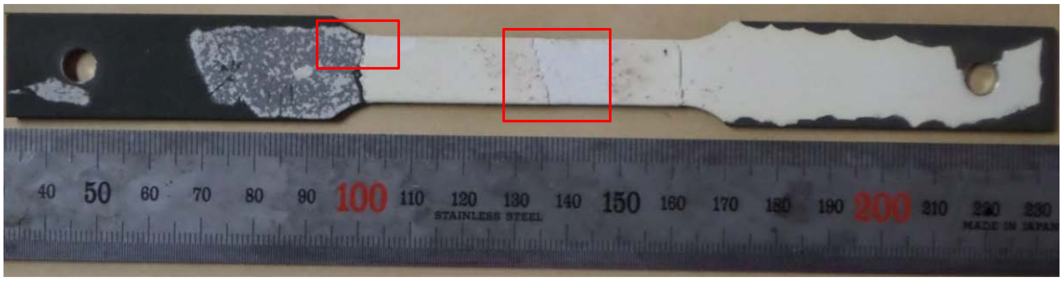

(d)

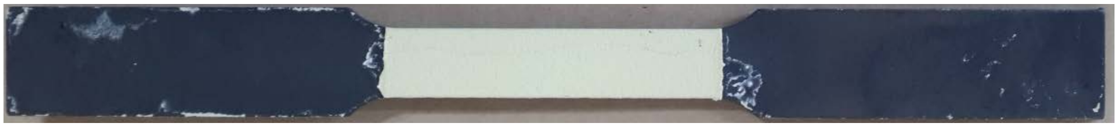

(e)

(f)

Figure 71: Photograph of samples before and after the first set of TGMF test: (a) as-sprayed sample 7, (b) sample 7 after 220 cycles, (c) as-sprayed sample 8, (d) sample 8 after 50 cycles, (e) as-sprayed sample 9, (f) sample 9 after 1200 cycles.

The optical images of the second set of TGMF test samples are shown in Fig.72. As shown in Fig.72b, both 8YSZ and LZ layer were partly delaminated near the center of the tensile bar after 38 TGMF cycles. Part of the bond coat was exposed due to the delamination. Fig.72d shows only the top LZ layer was delaminated after 49 TGMF cycles. Comparing with the first set TGMF tests, both sample 3 and sample 4 have shorter lifecycles in the second set TGMF tests. DCL porous 8YSZ + LZ has better performance in lower temperature gradient (the first set TGFM tests) and became worse in higher temperature gradient (the second set TGFM tests).

(a)

(b)

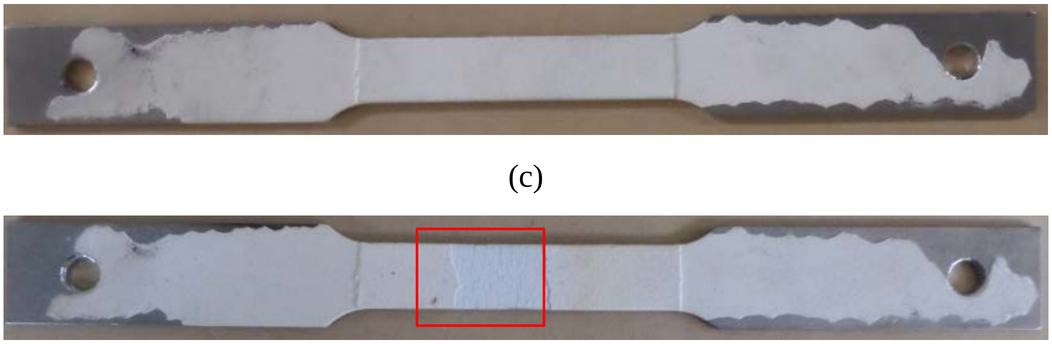

(c)

(d)

Figure 72: Photograph of samples before and after the second set of TGMF tests (a) as-sprayed sample 7, (b) sample 7 after 38 cycles, (c) as-sprayed sample 8, (d) sample 8 after 49 cycles.

Typically, the spallation process began at edges between LZ coats and 8YSZ coats sublayer. In this TGMF experiments, all the spallation occurred near the interface of the LZ layer and 8YSZ layers, which is just underneath the LZ top coats. The first stage of the spallation process was the buckling of the LZ top coats layer, following the occurrence of cracks in the interface. The second stage was the propagation of cracks in the interface, which followed by the spallation of top coat. Finally, the LZ top coat was peeled off [42].

Because the coefficients of thermal expansion (CTE) in 8YSZ (11×10^{-6} K^{-1} at 1000 ^{o}C) are large than LZ (9×10^{-6} K^{-1} at 1000 ^{o}C) [34, 40], so the volume difference is very large between 8YSZ and LZ layers. Due to the mismatch of volume change, thermal residual stress was induced in the thermal cycles. The thermal residual stress in the interface was accumulated during this TGMF cycles. When the accumulated residual stress became larger than the critical yield stress of the LZ material, crack and spallation occurred. Besides, the fracture toughness of LZ is lower than 8YSZ [17, 18], so DCL 8YSZ and LZ coats tend to delaminate first at LZ layers near the interface.

Task 5.5: Durability of composite LZ/8YSZ coatings

Both FCT and JETS test were performed in the composite coating samples. In the FCT test, the round button samples were heated at a surface temperature of 1100 ^{o}C (1373 K) for 40 min and then cooled with natural air at room temperature for 20 min. In the JETS test, the same equipment and heating/cooling regime were applied as the layered coating, except the surface heating temperature is 1400 ^{o}C, which is higher than that used for the layered coating. The failure criterion for both FCT and JETS were defined as 20% top coat delamination.

The equivalent operating hours (EOH) is an analytical parameter that commonly used to estimate the TBC lifetime during the operation of the gas turbine engine, which can be expressed as the following equation.

$$EOH = AOH + 20(\sum S_i + \sum LR_i + \sum T_i + \sum LC_i) \times F \tag{32}$$

where AOH, ΣS_i, ΣLR_i, ΣT_i, ΣLC_i and F correspond to actual operating hours, the coefficient of correction, load rejection, trip, rapid load change, and fuel factor, respectively. In this study, the EOH can be approximated by multiplying 21 to the member of FCT cycles [43, 44].

The summary of the FCT and JETS test results are listed in Table 13. The FCT tests were conducted for each sample to an equivalent thermal durability of 24000 EOH, which is equal to 1143 cycles. The JETS tests were aimed to perform for 2000 cycles to compare with the state-of-the-art single layer 8YSZ coating. Compare with the layered LZ based TBC, all the composted LZ/8YSZ coating have better performance in FCT test. Sample 10, which is a single layer coating with the composition of LZ/8YSZ in a 50%: 50% volume ratio, delaminated after 540 cycles in FCT and 70 cycles in JETS, showing very poor thermal stability. Sample 12 which is a single layer coating with the composition of LZ/8YSZ in a 25%: 75% volume ratio, delaminated in 936 cycles in FCT and 1022 cycles in JETS, showing a better performance than sample 10. The comparison between sample 10 and sample 12 indicates that the thermal durability can be improved by controlling the composition ratio of the composite coating. Although the sample 11, which have single 8YSZ buffer layer, shares the same top coat with sample 10, it shows a good performance in JETS test and better performance in FCT than sample 10. The comparison between sample 10 and sample 11 indicates that the thermal durability can be effectively improved by introducing buffer layer. Sample 13 has two composite coat layers and an 8YSZ buffer layer. Sample 13 shows the best performance in FCT and JETS tests, which is the only TBC survived in both tests without spallation, suggesting that combining the buffer layer and the gradient LZ/8YSZ composite top coat is an effective architecture to improve the thermal durability performance.

Table 13: Thermal cycling results of composite TBC samples

Sample #	FCT test/Status	JETS test/Status
10	540 cycles (11,340 EOH)/ Fully delaminated	70 cycles/ Fully delaminated
11	768 cycles (16,128 EOH) / Fully delaminated	2000 cycles/ Intact
12	936 cycles (19,656 EOH) / Fully delaminated	1022 cycle/ Fully delaminated
13	1143 cycles (24,000 EOH)/ Intact	2000 cycles/ Intact

The cross-sectional SEM microstructure images of all the samples after FCT and JETS test are shown in Fig.73. As shown in the figure, all of the delamination occurred near the interface between the top (the LZ/8YSZ composite layer and the buffer layer) and bond coat. During the FCT test the TGO layer (α-Al_2O_3 in black color) was observed at the interface between the top coat and bond coat. The TGO layer at the interface becomes fragile part and result to delamination when TGO thickness grows greater than 10 μm. However, the TGO in these composite samples is far less than 10 μm, which is not the reason to the delamination of the top coat. In Fig.73d and Fig.73h, the sample 11 and sample 13 show the microstructure of vertical cracks in top coat after the JETS test, which can provide the strength compliance during the thermal cycling test and improve the thermal durability [11].

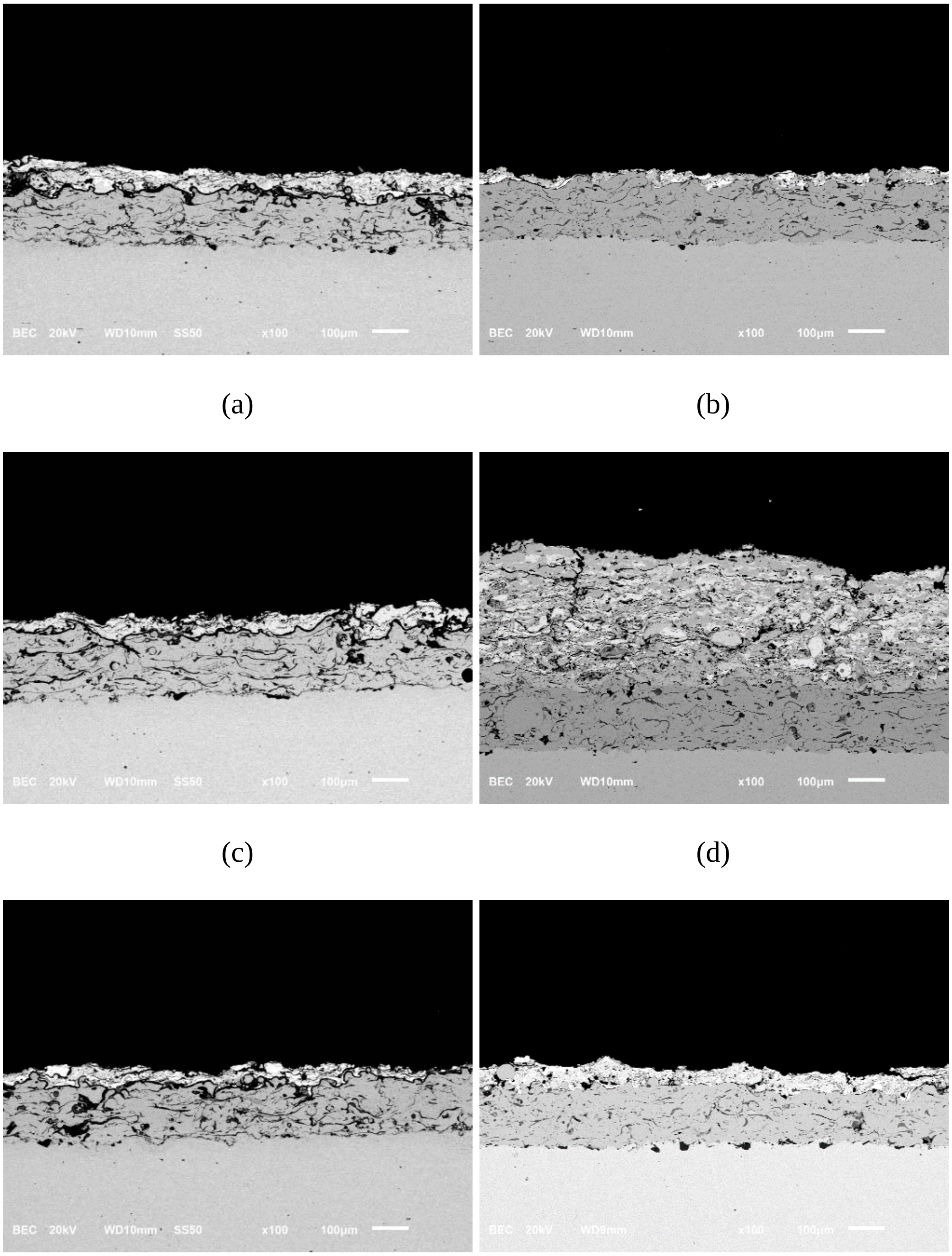
BEC 20kV WD10mm SS50 x100 100μm
BEC 20kV WD10mm x100 100μm
BEC 20kV WD10mm SS50 x100 100μm
BEC 20kV WD10mm x100 100μm
BEC 20kV WD10mm SS50 x100 100μm
BEC 20kV WD9mm x100 100μm

(a) (b)

(c) (d)

(e) (f)

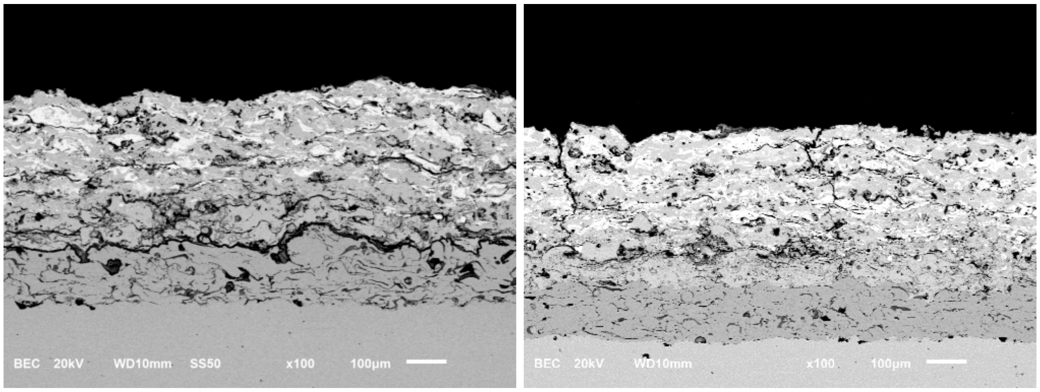

(g) (h)

Figure 73: SEM microstructure images of composite coatings after FCT and JETS test: (a) sample 10 after FCT test, (b) sample 10 after JETS test, (c) sample 11 after FCT test, (d) sample 11 after JETS test, (e) sample 12 after FCT test, (f) sample 12 after JETS test, (g) sample 13 after FCT test, (h) sample 13 after JETS test.

Fig.74 summarizes the FCT and JETS cycle results for both layered and composite LZ/8YSZ TBC, including from samples 6 to sample 13. As shown in Fig.74, the FCT performance of composite LZ/8YSZ coating (sample 10 – 13) improved greatly. The JETS test of coating with the buffer layer (multiple layer coating, sample 7, 8, 11 and 13) have better performance than the single layer LZ based TBC. Sample 9 single layer 8YSZ TBC is the standard reference sample. Comparing with other LZ based TBC samples, sample 13 exhibits the most outstanding thermal durability performance. This improvement of the thermal durability primarily is primarily due to the reduce of the CTE mismatch at the interface by the relatively continuous composition variation, and the increase of the fracture toughness in the LZ coating by adding 8YSZ that has high fracture toughness. In addition, the double layer gradient composite LZ/8YSZ coating with buffer layers can accommodate the residual stress, so the stress is dissipated in the composite top coat and its buffer layers.

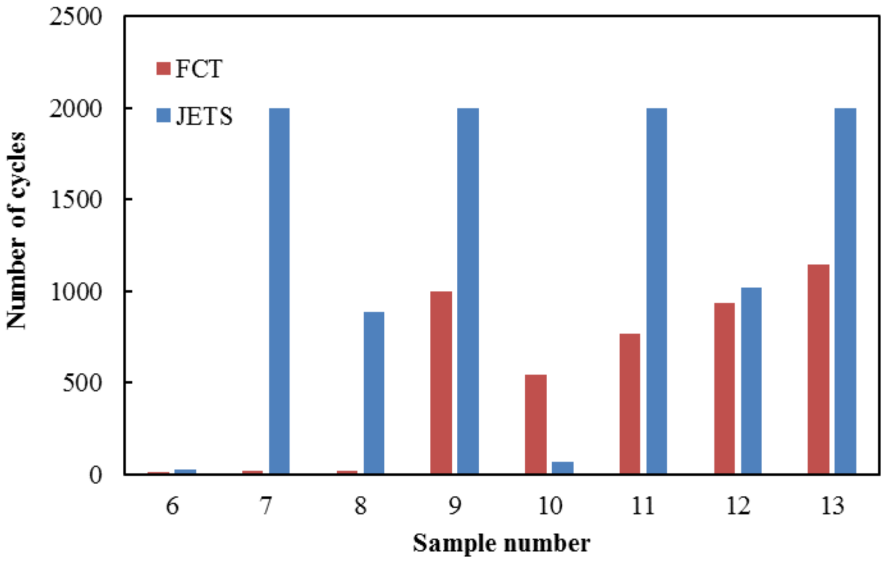

Figure 74: Comparison of number of cycles between the layered and composite TBC samples in FCT and JETS tests.

In summary, the SCL, DCL and composite LZ based TBC samples were successfully deposited using APS technique. The microstructures confirm that the porosities increase as the standoff distance increases. The intrinsic defect like pores, splat boundaries, and cracks are not uniformly dispersed in LZ and 8YSZ top coat. This task systematically discussed the physical, mechanical, thermal properties of LZ based coatings, and analyzed the thermomechanical durability of LZ base layered and composite coatings. The main conclusions of this task can be summarized as following aspects.

(1) Both furnace heat treatment and JETS tests show that the double-layer coating with porous 8YSZ and LZ layers have better thermal shock and thermal cycling performances than those of the single-layer LZ coating and the double-layer coating with the dense 8YSZ and the LZ layers. The results suggest that the porous 8YSZ can be used as a buffer layer for LZ based TBC systems to improve the durability during service. However, all the LZ coating were delaminated in the FCT test. The delamination of LZ coating in FCT and JETS test are related to the thermal residual stress that induced by the CTE difference and the low fracture toughness of LZ material.

(2) LZ coats last shorter cycles than 8YSZ coats in TGMF experiments. The primary reason for the spallation of LZ coat is mainly due to the lower fracture toughness. Besides, the large difference of CTE between 8YSZ and LZ layer will lead to high thermal residual stress. The residual stress accumulated until it reached the fracture strength of LZ. The crack occurred near the interface of 8YSZ and LZ layer.

(3) Since the layered LZ based TBC has limited thermal durability performance, the LZ/YSZ composite coating are proposed and deposited in four architectures. The double layer (50% LZ + 50% 8YSZ and 25% LZ + 75% 8YSZ) gradient composite TBC with 8YSZ buffer layers shows the best thermal durability performance in both FCT and JETS test. This is because the composite LZ/YSZ coating reduce the CTE difference at the interface, and the fracture toughness is increased in the LZ top coat by adding 8YSZ.

REFERENCES

1. Labrincha, J.A., J.R. Frade, and F.M.B. Marques, *La2Zr2O7 formed at ceramic electrode/YSZ contacts.* Journal of Materials Science, 1993. **28**(14): p. 3809-3815.
2. Xu, Z., et al., *Preparation and characterization of La2Zr2O7 coating with the addition of Y2O3 by EB-PVD.* Journal of Alloys and Compounds, 2010. **492**(1-2): p. 701-705.
3. Zhou, H., et al., *Preparation and thermophysical properties of CeO2 doped La2Zr2O7 ceramic for thermal barrier coatings.* Journal of Alloys and Compounds, 2007. **438**(1-2): p. 217-221.
4. Kido, H., S. Komarneni, and R. Roy, *Preparation of La2Zr2O7 by Sol—Gel Route.* Journal of the American Ceramic Society, 1991. **74**(2): p. 422-424.
5. Willy Poulsen, F. and N. van der Puil, *Phase relations and conductivity of Sr- and La-zirconates.* Solid State Ionics, 1992. **53–56, Part 2**(0): p. 777-783.
6. Matsumura, Y., et al., *Formation and sintering of La2Zr2O7 by the hydrazine method.* Solid State Communications, 1997. **104**(6): p. 341-345.
7. Zhang, J., *Novel Functional Graded Thermal Barrier Coatings in Coal-fired Power Plant Turbines.* 2015 NETL Crossingcutting Research Review Meeting, Pittsburgh, PA, April 27-30, 2015, 2015.
8. Zhang, J., et al., *Microstructural Non-uniformity and Mechanical Property of Air Plasma-sprayed Dense Lanthanum Zirconate Thermal Barrier Coating.* Materials Today: Proceedings, 2014. **1**(1): p. 11-16.
9. Taylor, T.A., *Low thermal expansion bondcoats for thermal barrier coatings*. 2011, US Patents No.7910225 B2.
10. Davis, J.R., *Handbook of thermal spray technology*. 2004: ASM international.
11. Guo, H.B., R. Vaßen, and D. Stöver, *Atmospheric plasma sprayed thick thermal barrier coatings with high segmentation crack density.* Surface and Coatings Technology, 2004. **186**(3): p. 353-363.
12. Lehmann, H., et al., *Thermal Conductivity and Thermal Expansion Coefficients of the Lanthanum Rare-Earth-Element Zirconate System.* Journal of the American Ceramic Society, 2003. **86**(8): p. 1338-1344.
13. Padture, N.P., M. Gell, and E.H. Jordan, *Thermal Barrier Coatings for Gas-Turbine Engine Applications.* Science, 2002. **296**(5566): p. 280-284.
14. Doerner, M.F., D.S. Gardner, and W.D. Nix, *Plastic properties of thin films on substrates as measured by submicron indentation hardness and substrate curvature techniques.* Journal of Materials Research, 1986. **1**(06): p. 845-851.
15. Oliver, W.C. and G.M. Pharr, *Measurement of hardness and elastic modulus by instrumented indentation: Advances in understanding and refinements to methodology*. Journal of materials research, 2004. **19**(01): p. 3-20.
16. Gell, M. and E. Jordan, *Bond strength and stress measurements in thermal barrier coatings*. 1995. Medium: ED; Size: 13 p.

17. Jiang, K., et al., *Microstructure and mechanical properties of La2Zr2O7–(Zr0.92Y0.08)O1.96 composite ceramics prepared by spark plasma sintering.* Ceramics International, 2014. **40**(9, Part A): p. 13979-13985.
18. Vassen, R., et al., *Zirconates as New Materials for Thermal Barrier Coatings.* Journal of the American Ceramic Society, 2000. **83**(8): p. 2023-2028.
19. Beshish, G.K., et al., *Fracture toughness of thermal spray ceramic coatings determined by the indentation technique.* Journal of Thermal Spray Technology, 1993. **2**(1): p. 35-38.
20. Hsueh, C.H., *Thermal stresses in elastic multilayer systems.* Thin Solid Films, 2002. **418**(2): p. 182-188.
21. Townsend, P.H., D.M. Barnett, and T.A. Brunner, *Elastic relationships in layered composite media with approximation for the case of thin films on a thick substrate.* Journal of Applied Physics, 1987. **62**(11): p. 4438-4444.
22. Tsui, Y.C. and T.W. Clyne, *An analytical model for predicting residual stresses in progressively deposited coatings Part 1: Planar geometry.* Thin Solid Films, 1997. **306**(1): p. 23-33.
23. Zhang, X.C., et al., *An analytical model for predicting thermal residual stresses in multilayer coating systems.* Thin Solid Films, 2005. **488**(1–2): p. 274-282.
24. Marshall, D.B., B.R. Lawn, and A.G. Evans, *Elastic/Plastic Indentation Damage in Ceramics: The Lateral Crack System.* Journal of the American Ceramic Society, 1982. **65**(11): p. 561-566.
25. Park, D., M.-W. Cho, and H. Lee, *Effects of the impact angle variations on the erosion rate of glass in powder blasting process.* The International Journal of Advanced Manufacturing Technology, 2004. **23**(5-6): p. 444-450.
26. Verma, A.P. and G.K. Lal, *A Theoretical Study of Erosion Phenomenon in Abrasive Jet Machining.* Journal of Manufacturing Science and Engineering, 1996. **118**(4): p. 564.
27. Slikkerveer, P.J., et al., *Erosion and damage by sharp particles.* Wear, 1998. **217**(2): p. 237-250.
28. Wellman, R.G. and J.R. Nicholls, *A Monte Carlo model for predicting the erosion rate of EB PVD TBCs.* Wear, 2004. **256**(9–10): p. 889-899.
29. Schmitt, M.P., B.J. Harder, and D.E. Wolfe, *Process-structure-property relations for the erosion durability of plasma spray-physical vapor deposition (PS-PVD) thermal barrier coatings.* Surface and Coatings Technology, 2016. **297**: p. 11-18.
30. Parker, W.J., et al., *Flash Method of Determining Thermal Diffusivity, Heat Capacity, and Thermal Conductivity.* Journal of Applied Physics, 1961. **32**(9): p. 1679-1684.
31. *Standard Test Method for Thermal Diffusivity by the Flash Method*, in *ASTM E1461-11*. 2011, American Society of Testing and Materials: West Conshohocken, PA.
32. Zhu, D., N.P. Bansal, and R.A. Miller. *Thermal Conductivity and Stability of HfO2-Y2O3 and La2Zr2O7 Evaluated for 1650 C Thermal/Environmental Barrier Coating Applications*. in *Proceedings of the 105th Annual Meeting and Exposition of the American Ceramic Society, The American Ceramic Society, Nashville, TN*. 2003.

33. Xu, C., et al., *Theory of the thermal expansion of Si and diamond.* Physical Review B, 1991. **43**(6): p. 5024-5027.
34. Zhang, J., et al., *Thermal expansion and solubility limits of cerium-doped lanthanum zirconates.* Journal of Alloys and Compounds, 2012. **525**(0): p. 78-81.
35. Cao, X.Q., R. Vassen, and D. Stoever, *Ceramic materials for thermal barrier coatings.* Journal of the European Ceramic Society, 2004. **24**(1): p. 1-10.
36. Hayashi, H., et al., *Thermal expansion coefficient of yttria stabilized zirconia for various yttria contents.* Solid State Ionics, 2005. **176**(5–6): p. 613-619.
37. Viswanathan, V., G. Dwivedi, and S. Sampath, *Multilayer, Multimaterial Thermal Barrier Coating Systems: Design, Synthesis, and Performance Assessment.* Journal of the American Ceramic Society, 2015.
38. Levi, C.G., et al., *Environmental degradation of thermal-barrier coatings by molten deposits.* MRS bulletin, 2012. **37**(10): p. 932-941.
39. Evans, A.G., et al., *Mechanisms controlling the durability of thermal barrier coatings.* Progress in Materials Science, 2001. **46**(5): p. 505-553.
40. Vaßen, R., F. Traeger, and D. Stöver, *New Thermal Barrier Coatings Based on Pyrochlore/YSZ Double-Layer Systems.* International Journal of Applied Ceramic Technology, 2004. **1**(4): p. 351-361.
41. Bolcavage, A., et al., *Thermal shock testing of thermal barrier coating/bondcoat systems.* Journal of Materials Engineering and Performance, 2004. **13**(4): p. 389-397.
42. Bartsch, M., et al., *Fatigue cracks in a thermal barrier coating system on a superalloy in multiaxial thermomechanical testing.* International Journal of Fatigue, 2008. **30**(2): p. 211-218.
43. Song, D., et al., *Microstructure design for blended feedstock and its thermal durability in lanthanum zirconate based thermal barrier coatings.* Surface and Coatings Technology, 2016.
44. Soares, C., *Gas turbines: a handbook of air, land and sea applications*. 2011: Butterworth-Heinemann.
45. Guo, X., et al., *Thermal Properties, Thermal Shock, and Thermal Cycling Behavior of Lanthanum Zirconate-Based Thermal Barrier Coatings.* Metallurgical and Materials Transactions E, 2016. **3**(2): p. 64-70.
46. Hill, R., *The elastic behaviour of a crystalline aggregate.* Proceedings of the Physical Society. Section A, 1952. **65**(5): p. 349.
47. Ingel, R.P. and D.L. Iii, *Elastic Anisotropy in Zirconia Single Crystals.* Journal of the American Ceramic Society, 1988. **71**(4): p. 265-271.
48. Anderson, O.L., *A simplified method for calculating the Debye temperature from elastic constants.* Journal of Physics and Chemistry of Solids, 1963. **24**(7): p. 909-917.
49. Hohenberg, P. and W. Kohn, *Inhomogeneous electron gas.* Physical review, 1964. **136**(3B): p. B864.
50. Kohn, W. and L.J. Sham, *Self-Consistent Equations Including Exchange and Correlation Effects.* Physical Review, 1965. **140**(4A): p. A1133-A1138.

51. Wu, L. and J. Zhang, *Ab initio study of anisotropic mechanical properties of LiCoO2 during lithium intercalation and deintercalation process.* Journal of Applied Physics, 2015. **118**(22): p. 225101.
52. Kresse, G. and J. Furthmüller, *Efficient iterative schemes for ab initio total-energy calculations using a plane-wave basis set.* Physical Review B, 1996. **54**(16): p. 11169-11186.
53. Kresse, G. and J. Furthmüller, *Efficiency of ab-initio total energy calculations for metals and semiconductors using a plane-wave basis set.* Computational Materials Science, 1996. **6**(1): p. 15-50.
54. Moriga, T., et al., *Crystal structure analyses of the pyrochlore and fluorite-type Zr2Gd2O7 and anti-phase domain structure.* Solid State Ionics, 1989. **31**(4): p. 319-328.
55. Tabira, Y., et al., *Systematic Structural Change in Selected Rare Earth Oxide Pyrochlores as Determined by Wide-Angle CBED and a Comparison with the Results of Atomistic Computer Simulation.* Journal of Solid State Chemistry, 2000. **153**(1): p. 16-25.
56. Kresse, G., M. Marsman, and J. Furthmüller, *VASP the guide.* http://cms.mpi.univie.ac.at/vasp/vasp/, 2013.
57. Den Toonder, J., J. Van Dommelen, and F. Baaijens, *The relation between single crystal elasticity and the effective elastic behaviour of polycrystalline materials: theory, measurement and computation.* Modelling and Simulation in Materials Science and Engineering, 1999. **7**(6): p. 909.
58. Arakere, N.K. and G. Swanson. *Effect of crystal orientation on fatigue failure of single crystal nickel base turbine blade superalloys*. in *ASME Turbo Expo 2000: Power for Land, Sea, and Air*. 2000. American Society of Mechanical Engineers.
59. Tang, W., E. Sanville, and G. Henkelman, *A grid-based Bader analysis algorithm without lattice bias.* Journal of Physics: Condensed Matter, 2009. **21**(8): p. 084204.
60. Henkelman, G., A. Arnaldsson, and H. Jónsson, *A fast and robust algorithm for Bader decomposition of charge density.* Computational Materials Science, 2006. **36**(3): p. 354-360.
61. Plimpton, S., *Fast Parallel Algorithms for Short-Range Molecular Dynamics.* Journal of Computational Physics, 1995. **117**(1): p. 1-19.
62. Crocombette, J.-P. and A. Chartier, *Molecular dynamics studies of radiation induced phase transitions in La 2 Zr 2 O 7 pyrochlore.* Nuclear Instruments and Methods in Physics Research Section B: Beam Interactions with Materials and Atoms, 2007. **255**(1): p. 158-165.
63. Hestenes, M.R. and E. Stiefel, *Methods of conjugate gradients for solving linear systems*. Vol. 49. 1952: NBS.
64. Barsoum, M.W., *Fundamentals of ceramics*. 2002: CRC Press.
65. Shimamura, K., et al., *Thermophysical Properties of Rare-Earth-Stabilized Zirconia and Zirconate Pyrochlores as Surrogates for Actinide-Doped Zirconia.* International Journal of Thermophysics, 2007. **28**(3): p. 1074-1084.
66. Liu, B., et al., *Theoretical elastic stiffness, structure stability and thermal conductivity of La2Zr2O7 pyrochlore.* Acta Materialia, 2007. **55**(9): p. 2949-2957.

67. Fischer-Cripps, A.C. and B.R. Lawn, *Stress Analysis of Contact Deformation in Quasi-Plastic Ceramics.* Journal of the American Ceramic Society, 1996. **79**(10): p. 2609-2618.
68. Lilleodden, E.T., et al., *Atomistic simulations of elastic deformation and dislocation nucleation during nanoindentation.* Journal of the Mechanics and Physics of Solids, 2003. **51**(5): p. 901-920.
69. Dupont, V. and T.C. Germann, *Strain rate and orientation dependencies of the strength of single crystalline copper under compression.* Physical Review B, 2012. **86**(13): p. 134111.
70. Clarke, D.R., M. Oechsner, and N.P. Padture, *Thermal-barrier coatings for more efficient gas-turbine engines.* MRS Bulletin, 2012. **37**(10): p. 891-898.
71. Clarke, D. and C. Levi, *Materials design for the next generation thermal barrier coatings.* Annual Review of Materials Research, 2003. **33**(1): p. 383-417.
72. Segall, M.D., et al., *First-principles simulation: ideas, illustrations and the CASTEP code.* Journal of Physics: Condensed Matter, 2002. **14**(11): p. 2717.
73. Blanco, M.A., E. Francisco, and V. Luaña, *GIBBS: isothermal-isobaric thermodynamics of solids from energy curves using a quasi-harmonic Debye model.* Computer Physics Communications, 2004. **158**(1): p. 57-72.
74. Chartier, A., et al., *Atomistic modeling of displacement cascades in* $La_2Zr_2O_7$ *pyrochlore.* Physical Review B, 2003. **67**(17): p. 174102.
75. Schelling , P.K., S.R. Phillpot , and R.W. Grimes, *Optimum pyrochlore compositions for low thermal conductivity.* Philosophical Magazine Letters, 2004. **84**(2): p. 127-137.
76. Maiti, A., G.D. Mahan, and S.T. Pantelides, *Dynamical simulations of nonequilibrium processes — Heat flow and the Kapitza resistance across grain boundaries.* Solid State Communications, 1997. **102**(7): p. 517-521.
77. Kubo, R., *Statistical Physics II Nonequilibrium Statistical Mechanics*. Second edition.. ed, ed. M. Toda and N. Hashitsume. 1991, Berlin, Heidelberg: Berlin, Heidelberg : Springer Berlin Heidelberg.
78. Che, J., et al., *Thermal conductivity of diamond and related materials from molecular dynamics simulations.* The Journal of Chemical Physics, 2000. **113**(16): p. 6888-6900.
79. Schelling, P.K., S.R. Phillpot, and P. Keblinski, *Comparison of atomic-level simulation methods for computing thermal conductivity.* Physical Review B, 2002. **65**(14): p. 144306.
80. Müller-Plathe, F., *A simple nonequilibrium molecular dynamics method for calculating the thermal conductivity.* The Journal of Chemical Physics, 1997. **106**(14): p. 6082-6085.
81. Müller-Plathe, F., *Reversing the perturbation in nonequilibrium molecular dynamics: An easy way to calculate the shear viscosity of fluids.* Physical Review E, 1999. **59**(5): p. 4894-4898.
82. Guo, X. and J. Zhang, *First Principles Study of Thermodynamic Properties of Lanthanum Zirconate.* Materials Today: Proceedings, 2014. **1**(1): p. 25-34.

83. Rappé, A.K., et al., *UFF, a full periodic table force field for molecular mechanics and molecular dynamics simulations.* Journal of the American chemical society, 1992. **114**(25): p. 10024-10035.
84. Guo, X., et al., *Image-based multi-scale simulation and experimental validation of thermal conductivity of lanthanum zirconate.* International Journal of Heat and Mass Transfer, 2016. **100**: p. 34-38.
85. Wang, L., et al., *Modeling of thermal properties and failure of thermal barrier coatings with the use of finite element methods: A review.* Journal of the European Ceramic Society, 2016. **36**(6): p. 1313-1331.
86. Wang, L., et al., *Influence of pores on the surface microcompression mechanical response of thermal barrier coatings fabricated by atmospheric plasma spray—Finite element simulation.* Applied Surface Science, 2011. **257**(6): p. 2238-2249.
87. Arai, M., H. Ochiai, and T. Suidzu, *A novel low-thermal-conductivity plasma-sprayed thermal barrier coating controlled by large pores.* Surface and Coatings Technology, 2016. **285**: p. 120-127.
88. Zhang, J., *et al. Quantitative analysis of pore morphology in lanthanum zirconate thermal barrier coating*. in *Materials Science and Technology (MS&T) 2014*. 2014.
89. Keyak, J.H., et al., *Automated three-dimensional finite element modelling of bone: a new method.* Journal of Biomedical Engineering, 1990. **12**(5): p. 389-397.
90. ImageJ. Available from: https://imagej.nih.gov/ij/.
91. COMSOL. 2016; Available from: https://www.comsol.com/.
92. Wang, Z., et al., *Effects of pores and interfaces on effective properties of plasma sprayed zirconia coatings.* Acta Materialia, 2003. **51**(18): p. 5319-5334.
93. Nair, B., J. Singh, and M. Grimsditch. *A model for residual stress evolution in air-plasma-sprayed zirconia thermal barrier coatings*. in *24th Annual Conference on Composites, Advanced Ceramics, Materials, and Structures-A: Ceramic Engineering and Science Proceedings*. 2009. John Wiley & Sons.
94. Sun, J., *Pulsed Thermal Imaging Measurement of Thermal Properties for Thermal Barrier Coatings Based on a Multilayer Heat Transfer Model.* Journal of Heat Transfer, 2014. **136**(8): p. 081601.
95. Finnis, M., *The theory of metal-ceramic interfaces.* Journal of Physics: Condensed Matter, 1996. **8**(32): p. 5811.
96. Mumm, D. and A. Evans, *On the role of imperfections in the failure of a thermal barrier coating made by electron beam deposition.* Acta Materialia, 2000. **48**(8): p. 1815-1827.
97. Evans, A. and J. Hutchinson, *The mechanics of coating delamination in thermal gradients.* Surface and Coatings Technology, 2007. **201**(18): p. 7905-7916.
98. Guo, X. and F. Shang, *Shear strength and sliding behavior of Ni/Al 2 O 3 interfaces: A first-principle study.* Journal of Materials Research, 2012. **27**(09): p. 1237-1244.
99. Christensen, A. and E.A. Carter, *Adhesion of ultrathin ZrO2 (111) films on Ni (111) from first principles.* Journal of Chemical Physics, 2001. **114**(13): p. 5816-5831.
100. Guo, X., et al., *Ideal tensile strength and shear strength of ZrO2(111)/Ni(111) ceramic-metal Interface: A first principle study*. Materials & Design, 2016. **112**: p. 254-262.

101. Kresse, G. and J. Hafner, *Ab initio molecular dynamics for liquid metals.* Physical Review B, 1993. **47**(1): p. 558.
102. Zhang, M., et al., *Hardness of FeB4: Density functional theory investigation.* The Journal of Chemical Physics, 2014. **140**(17): p. 174505.
103. Bader, R.F., *Atoms in molecules.* Accounts of Chemical Research, 1985. **18**(1): p. 9-15.
104. Ogata, S., *et al. Ab Initio Study of Ideal Shear Strength*. in *IUTAM Symposium on Mesoscopic Dynamics of Fracture Process and Materials Strength*. 2004. Springer.
105. Ledbetter, H. and R.P. Reed, *Elastic Properties of Metals and Alloys, I. Iron, Nickel, and Iron-Nickel Alloys.* Journal of Physical and Chemical Reference Data, 1973. **2**(3): p. 531-618.
106. Becke, A.D. and K.E. Edgecombe, *A simple measure of electron localization in atomic and molecular systems.* The Journal of Chemical Physics, 1990. **92**(9): p. 5397-5403.
107. Silvi, B. and A. Savin, *Classification of chemical bonds based on topological analysis of electron localization functions.* Nature, 1994. **371**(6499): p. 683-686.
108. Liang, T., et al., *Classical atomistic simulations of surfaces and heterogeneous interfaces with the charge-optimized many body (COMB) potentials.* Materials Science and Engineering: R: Reports, 2013. **74**(9): p. 255-279.

APPENDIX: PUBLICATIONS AND PRESENTATIONS AS A RESULT OF THIS RESEARCH

Journal articles

1. Jing Zhang, Xingye Guo, Yeon-Gil Jung, Li Li, and James Knapp, Lanthanum Zirconate Based Thermal Barrier Coatings: A Review, Surface and Coatings Technology, 2016 (in press, DOI: 10.1016/j.surfcoat.2016.10.019)
2. Xingye Guo, Yi Zhang, Yeon-Gil Jung, Li Li, James Knapp, and Jing Zhang, Ideal Tensile Strength and Shear Strength of ZrO2(111) / Ni (111) Ceramic-Metal Interface: A First Principles Study, Materials & Design, vol. 112, pp. 254-262, 2016.
3. Xingye Guo, Bin Hu, Changdong Wei, Jiangang Sun, Yeon-Gil Jung, Li Li, James Knapp, and Jing Zhang, Image Based Multi-Scale Simulation and Experimental Validation of Thermal Conductivity of Lanthanum, International Journal of Heat and Mass Transfer, vol. 100, pp. 34-38, 2016.
4. Xingye Guo, Linmin Wu, Yi Zhang, Yeon-Gil Jung, Li Li, James Knapp, and Jing Zhang, First Principles Study of Oxygen Adsorption on Nano-Structured Lanthanum Zirconate Surfaces, Physica E: Low-dimensional Systems and Nanostructures, vol. 83, pp. 36-40, 2016.
5. Xingye Guo, Zhe Lu, Li Li, James Knapp, Yeon-Gil Jung, and Jing Zhang, Thermal property, thermal shock and thermal cycling behavior of lanthanum zirconate based thermal barrier coatings, Metallurgical and Materials Transactions E, vol. 3, pp. 64-70, 2016.
6. Xingye Guo, Linmin. Wu, Yeon-Gil Jung, Li Li, James Knapp, and Jing Zhang, Carbon dioxide adsorption on lanthanum zirconate nanostructured coating surface: a DFT study, Adsorption, vol. 22, pp. 159-163, 2016.
7. Dowon Song, Ungyu Paik, Xingye Guo, Jing Zhang, Ta-Kwan Woo, Zhe Lu, Sung-Hoon Jung, Je-Hyun Lee, and Yeon-Gil Jung, Microstructure design for blended feedstock and its thermal durability in lanthanum zirconate based thermal barrier

coatings, Surface and Coatings Technology, 2016. (In press, DOI: 10.1016/j.surfcoat.2016.07.112)

Conference proceedings and presentations

1. Xingye Guo and Jing Zhang, First Principles Study of Thermodynamic Properties of Lanthanum Zirconate, Materials Today Proceedings, vol. 1, pp. 25-34, 2014.
2. Dowon Song, Ungyu Paik, Xingye Guo, Jing Zhang, Zhe Lu, Je-Hyun Lee, Yeon-Gil Jung,Microstructure design for blended feedstock and its thermal durability in lanthanum zirconate based thermal barrier coatings, 2016 International Conference on Metallurgical Coatings and Thin Films (ICMCTF 2016), San Diego, CA, USA, April 25-29, 2016
3. Xingye Guo, Zhe Lu, Yeon-Gil Jung, Li Li, James Knapp, Jing Zhang, Thermal and mechanical properties of novel lanthanum zirconate based thermal barrier coatings, 2016 International Thermal Spray Conference (ITSC 2016), Shanghai, China, May 10 - May 12, 2016
4. Sung Hoon Jung, Zhe Lu, Seung Soo Lee, Yeon Gil Jung, Jing Zhang, Ungyu Paik, Microstructure design and thermal durability of Yb-Gd-YSZ thermal barrier coatings in cyclic thermal exposure, 2016 International Thermal Spray Conference (ITSC 2016), Shanghai, China, May 10 - May 12, 2016
5. Xingye Guo, Zhe Lu, Sung-Hoon Jung, Yeon-Gil Jung, Li Li, James Knapp, Jing Zhang, Microstructure Design of Novel Composite Lanthanum Zirconate-Yttria Stabilized Zirconia Based Thermal Barrier Coatings, Materials Science & Technology 2016 (MS&T16), Salt Lake City, UT, USA, October 23-27, 2016
6. Jing Zhang, Microstructure Design and Performance of Lanthanum Zirconate Based Thermal Barrier Coatings, Department of Materials Science, Purdue University, November 6, 2015
7. Xingye Guo, Jing Zhang, Yeon-Gil Jung, Li Li, James Knapp, Carbon Dioxide Adsorption on Nanostructured Lanthanum Zirconate Surface: A DFT study, IUPUI Nanotechnology Research Forum and Poster Symposium, Indianapolis, IN, October 23, 2015
8. Xingye Guo, Jing Zhang, Novel Lanthanum Zirconate Thermal Barrier Coatings For Gas Turbines, The Joint Board of Advisors Meeting, IUPUI, October 13th, 2015

9. Yeon-Gil Jung, Jing Zhang, Microstructure Design of Lanthanum Zirconate Coatings and Its lifetime Performance, The MS&T 2015, Material Science & Technology Conference and Exhibition, October 4 - October 8, 2015, Columbus, OH
10. Xingye Guo, Jing Zhang, Zhe Lu, Yeon-Gil Jung, Thermal Gradient Mechanical Fatigue Study of Lanthanum Zirconate Thermal Barrier Coatings, The MS&T 2015, Material Science & Technology Conference and Exhibition, October 4 - October 8, 2015, Columbus, OH
11. Xingye Guo, Jing Zhang, Density Functional Theory Study of Gas Adsorption on Lanthanum Zirconate Nanostructured Coating Surface, The MS&T 2015, Material Science & Technology Conference and Exhibition, October 4 - October 8, 2015, Columbus, OH
12. Yi Zhang, Jing Zhang, Sintering of Nanostructured Zirconia: A Molecular Dynamics Study,The MS&T 2015, Material Science & Technology Conference and Exhibition, October 4 - October 8, 2015, Columbus, OH
13. Dowon Song, Ungyu Paik, Jing Zhang, Zhe Lu, Je-Hyun Lee, Yeon-Gil Jung, Microstructure Design and Thermal Durability of Lanthanum Zirconate Based Thermal Barrier Coatings, 7th Asian Thermal Spray Conference (ATSC2015), Xi'an, China, September 23-25, 2015
14. Zhe Lu, Je-hyun Lee, Yeon-Gil Jung, Jing Zhang, Dowon Song, Ungyu Paik, Microstructure Evolution and Durability of Thermal Barrier Coatings in Thermally Graded Mechanical Fatigue Environments, 7th Asian Thermal Spray Conference (ATSC2015), Xi'an, China, September 23-25, 2015
15. Jing Zhang, Advanced Materials Research, Argonne National Laboratory, September 11, 2015
16. Yeon-Gil Jung, Zhe Lu, Ungyu Paik, and Jing Zhang, Lifetime Performance of Thermal Barrier Coatings in Thermally Graded Mechanical Fatigue Environments, The 11th International Conference of Pacific Rim Ceramic Societies(PacRim-11), Jeju, Korea, August 30 - September 4, 2015
17. Yeon-Gil Jung, Zhe Lu, Qi-Zheng Cui, Sang-Won Myoung, and Jing Zhang, Thermal Durability and Fracture Behavior of Thermal Barrier Coatings in Thermally Graded Mechanical Fatigue Environments, the International Symposium on Green Manufacturing and Applications 2015 (ISGMA 2015), Qingdao, China, June 23 - June 27, 2015
18. Jing Zhang, Yeon-Gil Jung (eds.), 1st International Joint Mini-Symposium on Advanced Coatings, Materials Today: Proceedings, 2014
19. Xingye Guo, Jing Zhang, Zhe Lu, Yeon-Gil Jung, Theoretical prediction of thermal and mechanical properties of lanthanum zirconate nanocrystal, the 1st International

Conference & Exhibition for Nanopia, Changwon Exhibition Convention Center, Gyeongsangnam-do Province, Miryang City, Korea, November 13-14, 2014

20. Sang-Won Myoung, Zhe Lu, Qizheng Cui, Je-Hyun Lee, Yeon-Gil Jung, Jing Zhang, Thermomechanical properties of thermal barrier coatings with microstructure design in cyclic thermal exposure, the 1st International Conference & Exhibition for Nanopia, Changwon Exhibition Convention Center, Gyeongsangnam-do Province, Miryang City, Korea, November 13-14, 2014

21. Zhang, J., X. Guo, Y.-G. Jung, L. Li, and J. Knapp, Microstructural Non-uniformity and Mechanical Property of Air Plasma-sprayed Dense Lanthanum Zirconate Thermal Barrier Coating. Materials Today: Proceedings, 2014. 1(1): p. 11-16.